Fluid-rock interaction in forming large ore deposits: metal mobilization, upgrading and mineral replacement reactions

by

Yanlu Xing

A thesis submitted for the degree of Doctor of Philosophy at

Monash University in 2019

School of Earth, Atmosphere and Environment

Copyright notice

Abstract

The formation of hydrothermal ore deposits, especially those large and giant in scale, are usually a result of extensive hydrothermal activities, where fluid-rock interactions play a key role in sourcing, transporting and depositing metals during hydrothermal fluid evolution. There are several aspects that affect the fate of metals during fluid-rock/mineral interaction, including metal solubility and aqueous speciation in fluids; partitioning behaviour of metals in mineral solid solutions; and mineral replacement via fluid-mediated dissolution-reprecipitation reactions. Moreover, multi-stage hydrothermal events are widely recognized in large to giant hydrothermal ore deposits. This complexity, combined with a lack of experimental data on metal solubility and speciation over the wide range of T-P conditions relevant for ore systems, however, make it hard to identify the key mechanisms that control ore formation. Hence, our understanding of fluid-rock interaction in hydrothermal ore forming processes is still limited, and this lack of knowledge limits our capability to identify the key factors and mechanisms that control mineralization and ore forming processes.

In this thesis, several key aspects of fluid-rock interaction that are important for ore generation have been investigated using thermodynamic modelling and hydrothermal experiments. These include: (1) influence of fluorine on the solubility of Fe, U, and REE in fluids; (2) role of trace elements, i.e., Ce(III/IV), in affecting mechanism and efficiency of fluid-rock/mineral reaction; (3) partitioning behaviour of As between fluid and Fe(As)-sulfide solid solutions; and (4) significance of multi-stage hydrothermal activities in forming high-grade ores. In case of hematite-rich IOCG deposits such as the Olympic Dam, the formation of high-grade Cu-Au-U-REE ores is hotly debated. New results of this thesis show that F can increase the metal (U and REE, but not Fe) carrying capacity of the fluids and help to dissolve silicates, which contributes to the large metal endowment in IOCG deposits. Furthermore, hydrothermal experiments show that trace amount of Ce(III) in fluids can significantly increase the porosity of hematite formed via replacement of magnetite, which increases the coupling between mineral reaction, fluid flow and element mass transfer, thus enhancing the ore forming processes. In general, these experiments provide the first evidence for the capacity of trace metals to act as a catalyst in promoting hydrothermal ore transport and deposition.

Extensive hydrothermal activities are thought to be important for the formation of many large and giant ore deposits. Remobilization and reprecipitation of metals may be crucial mechanism for generating high grade ores in many of these deposits. Results from reactive transport

modelling indicate that in the context of the Olympic Dam deposit, remobilization and reprecipitation of U, Cu and F can explain the formation of high-grade U-Cu (+fluorite) ores.

Similarly, based on the newly developed solid solution model for As in pyrite and arsenopyrite, reactive transport modelling shows that similar scenario can also explain the formation of high grade As(-Au) pyrite in orogenic gold systems, where dilute solution can drive dissolution-reprecipitation reactions and enrich As(-Au) in Fe sulfide minerals.

Thesis including published works declaration

I hereby declare that this thesis contains no material which has been accepted for the award of any other degree or diploma at any university or equivalent institution and that, to the best of my knowledge and belief, this thesis contains no material previously published or written by another person, except where due reference is made in the text of the thesis.

This thesis includes 3 original papers published in peer-reviewed journals, and one additional chapter to be submitted for publication. The core theme of the thesis is understanding the influence from fluid-rock interaction on forming giant hydrothermal ore deposits, based on investigations of metal hydrothermal mobilization, mineral replacement reaction and reactive transport modelling. The ideas, development and writing up of all the papers in the thesis were the principal responsibility of myself, the student, working within the School of Earth, Atmosphere and Environment under the supervision of Prof. Joël Brugger, A.Prof. Andy Tomkins, Dr. Barbara Etschmann, and Dr. Yuan Mei.

The inclusion of co-authors reflects the fact that the work came from active collaboration between researchers and acknowledges input into team-based research.

In the case of each chapter, my contribution to the work involved the following:

Thesis Chapter	**Publication Title**	**Status** *(published, in press, accepted or returned for revision, submitted)*	**Nature and % of student contribution**	**Co-author name(s) Nature and % of Co-author's contribution***	**Co-author(s), Monash student Y/N***
2	The role of fluorine in hydrothermal mobilization and transportation of Fe, U and REE and the formation of IOCG deposits	Published	75%; thermodynamic modelling, data analysis and manuscript preparation	1)Joël Brugger(10%) 2)Barbara Etschmann(5%) 3)Weihua Liu(2%) 4)Yuri Shvarov(3%) 5)Andy Tomkins(2%) 6)Yuan Mei(2%) 7)Denis Testemale(1%)	1,2,5) Y; 3,4,6,7)N
3	Uranium transport in F-Cl-bearing fluids and hydrothermal upgrading of U-Cu ores in IOCG deposits	Published	80%; thermodynamic modelling, and preparation of manuscript	1)Joël Brugger(10%) 2)Yuan Mei(5%) 3)Weihua Liu(3%) 4)Barbara Etschmann(2%)	1,4)Y; 2,3)N

4	Trace cerium catalyzes formation of giant ore deposits	In preparation	80%; hydrothermal experiments, sample preparation, data collection and interpretation, and manuscript preparation	1)Joël Brugger(10%) 2)Barbara Etschmann(4%) 3)Andy Tomkins(4%) 4)Xiya Fang(2%)	Y
5	Arsenic evolution as a tool for understanding formation of pyritic gold ores	Published	70%; thermodynamic modelling, and manuscript preparation	1)Joël Brugger (20%) 2)Andy Tomkins (5%) 3)Yuri Shvarov (5%)	1,2)Y; 3)N

I have renumbered sections of the not submitted papers in order to generate a consistent presentation within the thesis.

Student name: Yanlu Xing

Student Signature: **Date:**

I hereby certify that the above declaration correctly reflects the nature and extent of the student's and co-author's contributions to this work. In instances where I am not the responsible author I have consulted with the responsible author to agree on the respective contributions of the authors.

Main Supervisor name: Joël Brugger

Main Supervisor Signature: **Date:**

Table of Contents

Acknowledgements

First of all, I would like to say thanks to my main supervisor, Professor Joël Brugger, for giving me the opportunity to do PhD in Monash University and getting me involved in such an amazing project. Joël has been giving me so much help since the start of my PhD. He guided me to the world of hydrothermal geochemistry and showed me with great patience on how to do thermodynamic modelling and hydrothermal experiments. It is never easy to start a research in a totally different area. Doing a PhD project is also not easy and it is more like a fight, a long journey, when you have to overcome many difficulties, work hard and think hard. However, doing research with Joël is always full of fun and joy. We can usually sit together for hours, discussing the meaning of a diagram. Sometimes, we got stuck together on the modelling, thinking hard and trying to find a solution. Joël is super enthusiastic on research. His great passion usually gave me confidence to overcome the difficulties and make my research better and better. To me, it is really a great fortune to be able to do research with Joël. He is more like an old friend than a big 'boss', with him you can talk about everything!

I would like to express my thanks and gratefulness to Dr. Barbara Etschmann. During my PhD, Barbara is always the first one that I talked to whenever I need help for my experiments. I still remember the first day I arrived at the school, that Barbara took me to the lab showing me how to use the high temperature furnace. As the lab manager, Barbara did so much to keep the lab to work in its best order. Everyone comes to Barbara for help and she is always there to help! She is always helpful and she always shows great patience to help me. Apart from research, it is also great to travel with Barbara and Joël. Barbara likes panda. In 2017, we travelled together to Chengdu in China to see panda. It was with a lot of fun that we spent a whole day in the panda zoo and we visited each panda for at least twice times!

I would like to say many thanks to Dr. Yuan Mei. In 2015, Mei referred me to Monash and helped me to apply for scholarship. At the beginning of my PhD, Mei gave me lots of help. She helped me to find the first house to stay. She was the first to take me to see kangaroo in the national park. She taught me how to use Matlab. During my PhD, she also helped me a lot on my writings and encouraged me to publish.

I would like to say thanks to my co-supervisor, Dr. Andy Tomkins. He gave me lots of very insightful suggestions on my research and helped me with my papers. I also thank Dr. Weihua Liu who usually helped to revise my papers and played Ping Pong with me.

There are so many people I need to say thanks. I thank Dr. Xiya Fang, who spent several years with me to explore the way to do EBSD on powder minerals. I would also like to thank Dr. Yuri Shvarov, who helped a lot with my modelling.

Furthermore, it is a great fortune to do my PhD in the School of Earth, Atmosphere and Environment. The staff here are always friendly and helpful. Thanks to Junnel who helped me prepare samples and do fantastic polishing. Thanks to Massimo who helped me with LA-ICP-MS.

Special thanks to my officemates, Chris Voisey and Nikk Hunter, who accompanied me during my PhD and made our office, room 109, such an amazing, happy and cheerful place to stay –

everyday here is enjoyable. I also thank many other PhD students in the school who made my time here at Monash colourful and memorable: Dr. Andrew Langendam, Sam Thiele, Andrew Giles, Mitchell O'Mara, Qiushi Guan and many others.

Finally, I would like to say thanks to my partner, Yang, who gave me so much support with my research and my life, helping and supporting me when I am in trouble, encouraging me when I am depressed, and travelling with me to explore the beautiful landscape of Australia. And so many thanks to my family, my parents and my sister in China, who are always there to help me whenever and whatever I need.

Chapter 1

Introduction

Yanlu Xing

School of Earth, Atmosphere and Environment, Monash University, Clayton, VIC, 3800

1.1 Fluid-rock interactions and the formation of hydrothermal ore deposits

Hydrothermal ore deposit is one of the most important classes of ore deposits in the world. Formation of hydrothermal ore deposits relies heavily on the property of the ore fluids and the interactions between hydrothermal fluids and surrounding rocks in Earth's crust (Heinrich and Candela, 2014; Seward et al., 2014). Three major processes have been summarized to describe the formation of a hydrothermal ore deposit: source, transport, and deposition (Fig. 1.1; Heinrich and Candela, 2014). During all these processes, fluid-rock interactions control the partitioning behaviour of metals between fluids and minerals. For example, the sourcing of metals can be described as preferential partitioning of metals into a fluid phase from a parent rock when they come into contact. Stable or relatively constant solubility of certain metals (normally in the form of their aqueous complexes) under specific geological conditions (e.g., P, T, wall rock) ensures that these metals are able to be transported and concentrated in space. Whenever changes in P-T, wall rock composition or mixing with other fluids disturbs the equilibrium state of the fluid itself (i.e., saturation state of minerals/metals dissolved in the fluid) or between fluid and the surrounding rock, metals will be deposited and thus form the mineralization.

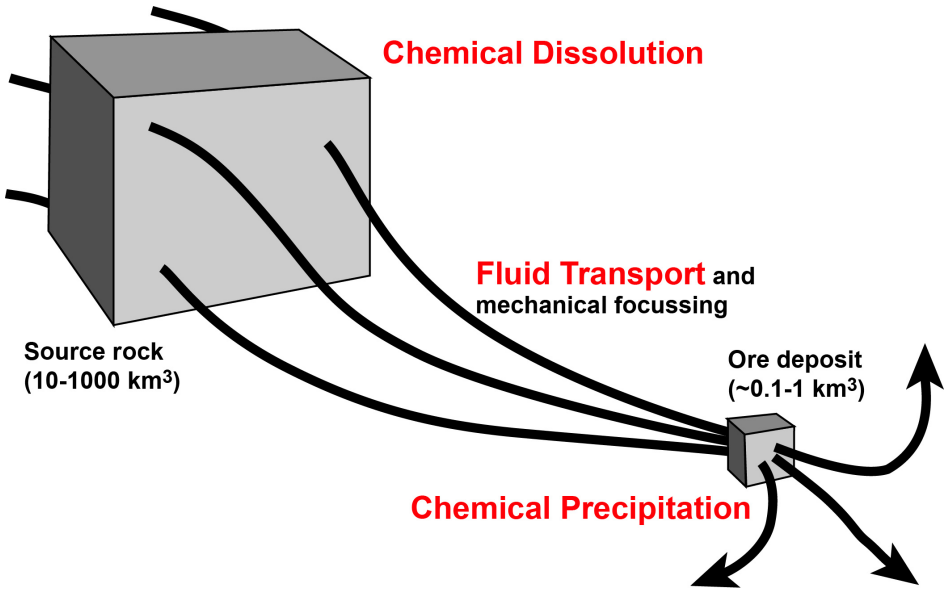

Fig. 1.1 Conceptual diagram showing processes during formation of hydrothermal ore deposits (modified from Brugger et al., 2010)

Factors affecting fluid-rock interactions include fluid chemistry (e.g., pH, salinity, availability of ligands), rock composition, pressure and temperature. However, it is usually hard to figure out the key mechanisms that control metal releasing into fluids, or deposition to form enrichment, due to the complexity of fluid and rock composition, combined with limited

understanding on metal solubility in fluids as well as in mineral solid solutions under high temperature and pressure, and on mechanisms of the fluid-mineral interaction. These fundamentally limit our understanding of ore formation processes.

The generation of large and giant ore deposits is usually a result of coincidental combination of common geological processes, or sometimes of unique processes (Richards, 2013). These factors include pressure and temperature change, mixing of different fluids, and interaction between ore fluids with certain wall-rocks. Particularly, some factors may play a fundamental role in contributing to the exceptional size of the hydrothermal ore deposit. For example, in orogenic gold deposits, pressure-drop controlled by seismic activity is a key factor for gold mineralization (Goldfarb et al., 2015). Pressure-drop induced boiling or phase separation of fluids changes the fluid composition and thus the saturation state of metals, i.e., Au, which interrupts the equilibrium of the original fluids and thus drives the gold precipitation. In IOCG deposits, permeability is often regarded as a key to controlling the metal endowment of the deposits (e.g., Davidson et al., 2007). This is because higher permeability of wall-rock or ore body will facilitate fluid penetration, increase fluid-rock interaction and also provide space for ore precipitation.

Though certain factor may play a major role in controlling ore formation in different type of hydrothermal ore deposits, the equilibrium state of the ore fluids, which determines the metal solubility and precipitation of ore minerals, and the interactions between fluids and surrounding rocks are generally the essential factor that determines the mineralization.

Specific mechanism that controls the accumulation of metal varies. However, in a common sense, fluid-rock interaction plays a fundamental role during hydrothermal mineralization processes. Therefore, a deeper understanding of fluid-rock interactions, regarding reaction mechanisms, solubility of metals in fluids and metal mobilization, and changes of ore or wall-rock textures (e.g., porosity change in the wall rock), is important to help retrieve the ore forming history, generalize accurate deposit genesis model, guide exploration and provide important knowledge on mineral processing and metal extraction.

It is important to note that multistage hydrothermal events and/or cyclic fluid flows have been emphasized by several studies for their contribution to the formation of large ore deposits (e.g., Brugger et al., 2000; Meffre et al., 2016). In fact, in many large and giant hydrothermal ore deposits, extensive or multistage hydrothermal events are observed in the formation of large to giant ore deposits (e.g., Haynes et al., 1995; Meffre et al., 2016; Fougerouse et al., 2017). Metals can be introduced and accumulated by each stage fluids, or are upgraded and refined through remobilization driven by hydrothermal fluids, although in many cases, key

mechanisms for metal enrichment in forming large ore deposits are still not clear, due to the complexity of ore fluids and nature of the wall rock, inaccuracy in determining the P-T conditions for mineralization, and the destruction of original features (e.g., porosity) by later stage alteration.

In summary, the aim of this thesis is to investigate how fluid-rock interaction can affect the enrichment of metals and contribute to the formation of large to giant hydrothermal ore deposits. Several aspects of fluid-rock interaction including metal transport, metal partitioning during fluid-mineral equilibria, and mineral replacement reactions are investigated. Moreover, reactive transport modelling is performed to investigate the mechanisms of multi-stage hydrothermal events in contributing to the formation of large to giant hydrothermal ore deposits including Iron Oxide Cu-Au (IOCG) deposits and hydrothermal gold deposits.

1.1.1 Iron Oxide Cu-Au deposits

Iron Oxide Cu-Au (IOCG) deposits are one type of the most significant hydrothermal ore systems in the world, being usually low-grade but giant to supergiant in scale (Groves et al., 2016). The defining features of IOCG deposits include (1) voluminous hematite and/or magnetite; (2) elevated concentrations of Cu, Au associated with Ag, U, REE and F in the ore; (3) intensive hydrothermal alteration of the host rock (Hitzman et al., 1992; Williams et al., 2005).

The Olympic Dam (OD) is a leading example of IOCG deposits, which is also one of the largest ore deposits in the world (Groves et al., 2016). The formation of OD has been a hot topic since its discovery, regarding the source of metals, hydrothermal evolution, host rock controls and genetic model (e.g., Haynes et al., 1995; McPhie et al., 2011). Though, key factors for generating the unique feature of OD, as well as the IOCG-type deposits, are still under debate.

There are two subclass endmembers of IOCG deposits, which are the magnetite-rich deposits, such as Kiruna-type magnetite-apatite deposits, and the hematite-rich deposits, such as OD (Hitzman et al., 1992). The hematite-rich deposits usually have higher Cu-Au(±U±REE) content compared to the magnetite-rich deposits. However, the reason for elevated Cu-Au(±U±REE) grade in hematite-rich ores in IOCG deposits is weakly understood (e.g., Bastrakov et al., 2007). It is suggested that permeability of the ore breccia is a key factor controlling metal endowments in IOCG deposits, with the fact that ore grade (Cu, Au), brecciation intensity and hematite:magnetite ratio being positively correlated among deposits from the Olympic Dam Cu-Au province (Gow et al., 1994; Davidson et al., 2007). This is supported by the result of Bastrakov et al. (2007), showing that hematite-stage alteration may

be responsible for the upgraded Cu-Au content in hematite-rich ores for sub-economic IOCG deposits.

Fluorine (F) enrichment is an important feature of many IOCG deposits (Hitzman et al., 1992; Williams et al., 2005; Chen and Zhou, 2014; Montreuil et al., 2016). McPhie et al. (2011) pointed out that ore fluids that are responsible for OD should be F-rich. It is thought that F contributes to the generation of the ores because F may enhance metal mobility via formation of strong fluoride complexes (e.g., U, REE) in the ore-forming fluids (McPhie et al., 2011). Moreover, the F-rich nature of ore fluids is possibly inherited from the F-rich host granite and/or the regional silicic igneous rocks (McPhie et al., 2011), which may also reinforce the source link between host rock and the OD ore regarding U and REE. Furthermore, the enrichment of F in ore fluids is thought to form significant amount of HF(aq), which is very corrosive to silicate rocks and may help increase permeability and porosity of the wall rock and the breccia complex.

The genetic model of IOCG deposits has long been discussed, including fluid mixing model and multi-stage hydrothermal upgrading model (e.g., Haynes et al., 1995; Bastrakov et al., 2007; Schlegel et al., 2018). For many of the large IOCG deposits, the two-stage upgrading model can well explain the formation of elevated Cu-Au(±U±REE) ores in the hematite-rich deposits (e.g., Olympic Dam, Oak Dam, and Prominent Hill). It is suggested that the fluids in the hematite stage are able to drive remobilization of Cu-Au(±U±REE) and reprecipitate them to form upgrading (e.g., Bastrakov et al., 2007). Particularly, Bastrakov et al. (2007) modelled the formation of sub-economic IOCG deposits from the Olympic Dam Cu-Au province using thermodynamic methods and show that the oxidation of pre-existing low-grade Cu-Au ores is effective in enriching Cu and Au in the ores. The fluid mixing model where an oxidized Cu-Au-bearing fluid mix with reduced fluids or interacting with ferrous iron-bearing minerals may explain some deposits such as the Prominent Hill (Schlegel et al., 2018), however, the extensively oxidized nature of OD and several other deposits (e.g., Emmie Bluff; Gow et al., 1994) and the variation in the extent of oxidation in the ores of different IOCG deposits imply protracted hydrothermal evolution history and overlapping of several stages of oxidizing hydrothermal alteration. In this case, a general model regarding IOCG formation still need further investigation. By far, the two-stage model or multi-stage model seems more reasonable in explaining especially those large and giant IOCG deposits in general.

1.1.2 Hydrothermal Gold deposits

Key factors that control the formation of different types of hydrothermal gold deposits are usually different, regarding their tectonic settings, relation to magmatism, and source of metals

and ore fluids (Groves and Santosh, 2015; Groves et al., 2016). For example, tectonic settings have a first-order control on the formation of giant orogenic gold deposits, and there is generally no direct link to magmatism, compared to porphyry deposits or Carlin-type (Groves et al., 2016).

The formation of large gold deposits can be attribute to either a single unusual event or a combination of several hydrothermal events (e.g., Meffre et al., 2016). However, large gold deposits usually show complex multi-stage mineralization events, compared to smaller ones, making it a common feature of the giant gold deposits (Sibson et al., 1975; Brugger et al., 2000; Bateman and Hagemann, 2004; Sung et al., 2009; Cockerton and Tomkins, 2012; Meffre et al., 2016; Fougerouse et al., 2017). Examples of these deposits cover a wide range of types of deposits including Orogenic gold (Kalgoorlie in Western Australia, Obuasi in West Africa, Bendigo gold deposit in central Victoria in Australia, etc.; Muller, 2014; Fougerouse et al., 2017; Thomas et al., 2011), Carlin-type (Nevada in USA; Cline et al., 2005), porphyry (Chuquicamata in Chile; Campbell et al., 2006; Silitoe, 2010) and IOCGs (Olympic Dam; Williams et al., 2005; Bastrakov et al., 2007).

A better understanding of the evolution history of these gold deposits is of great practical significance to help with exploration. However, overprinting of early mineralization by later stage fluids usually makes it especially challenging to precisely quantify the contribution of metals during each mineralization stage based on textural and chemical analysis of ore samples. In case of orogenic gold and the Carlin-type deposits, especially those large in size showing complex ore forming histories, it is usually hard to quantify the gold mineralization in each stage due to the complexity of gold geochemical behaviour and varying P-T at each stage.

Several elements have affinity to Au, such as As, Ag, Bi, Te and Sb (Deditius et al., 2014; Tooth et al., 2008; Saunders et al., 2014). These elements have the potential to be used as tool to reveal the mineralization history of Au (e.g., Tooth et al., 2008). Among these elements, the association of As and Au has been widely observed in gold deposits and the hydrothermal mobilization of As in fluids has been relatively well studied (Brugger et al., 2016). Pyrite and arsenopyrite are important gold-hosting minerals, with As and Au usually being closely associated in these minerals (Deditius et al., 2014). This coupled As and Au geochemistry in pyrite and arsenopyrite makes As a potential tool to look at Au mineralization history. However, the partitioning behaviour of As between pyrite, arsenopyrite and hydrothermal fluids remains poorly understood due to the lack of knowledge for As in solid solutions of iron sulfide minerals. Currently, rare experiments have been performed on the partitioning of As between fluids and Fe-sulfide minerals, and there is no solid solution thermodynamic model for As in

pyrite and arsenopyrite that can be used for accurately predicting As behaviour using thermodynamic modelling.

1.2 Key aspects of fluid-rock interactions

1.2.1 Metal mobility in hydrothermal fluids

The stability of metal complexes depends on pressure, temperature and fluid chemistry (e.g., pH, fO_2). The basic understanding on how these factors control the stability of metal aqueous complexes is important predicting metal mobilization and deposition over the wide range of conditions relevant to hydrothermal ore systems.

The solubility of metals in hydrothermal fluids is strongly affected by ligands in fluids (e.g., Brugger et al., 2016). Metals form complexes with ligands such as F^-, Cl^-, HS^-, SO_4^{2-} and CO_3^{2-}. According to the soft-hard acid-base theory, hard ligands form strong complexes with hard metals while soft ligands form stable complexes with soft metals (Pearson, 1963). Therefore, fluids with specific ligands can selectively transport metals.

Fluoride (F^-) is classified as a hard ligand that can form strong complexes with hard cations such as Fe^{3+}, REE^{3+} and U(IV/VI) (Bastrakov et al., 2010; Pearson, 1963; Seward and Barnes, 1997). It has long been thought that F^- is the 'key' ligand for REE hydrothermal transportation (Williams-Jones et al., 2000). Recently, however, Williams-Jones et al. (2012) shows that REE chloride complexes are indeed the most important complexes for the hydrothermal transportation of REE, due to the prevalence of chloride ions in natural fluids, whereas fluoride acts as a 'precipitating ligand' as a result of the low solubility of REE-F minerals at elevated temperatures (Migdisov et al., 2016), and the increasing concentration of F in fluids may give rise to the precipitation of REEs. For IOCG systems such as Olympic Dam, the source of F and its role in contributing to the extraordinary metal endowment in the deposit is still under debate, regarding whether the F-rich host granite could be good source of F and the role of F in transporting metals including Fe, U and REE.

1.2.2 Fluid-mediated mineral replacement reaction

Mineral replacement reactions are common in hydrothermal ore systems and the catalysing effect of hydrothermal fluids on the mineral replacement reactions has been emphasized by several studies (e.g., Fougerouse et al., 2016; Li et al., 2015; Putnis, 2009). Most fluid-driven mineral replacement reactions happen via a coupled dissolution-reprecipitation reactions (CDR) mechanism, which consists of dissolution of the parent mineral and reprecipitation of new minerals (Putnis, 2009). Effects from mineral replacement reactions on forming ore deposits

include porosity and texture change, and sequestration and upgrading of metals in minerals (e.g., Altree-Williams et al., 2015; Xia et al., 2009). Altree-Williams et al. (2015) pointed out that CDR reactions can cause remarkable change on mineral textures. This may cause significant change on the ore porosity, which may further affect the efficiency of fluid-rock interaction.

For IOCG deposits, replacement of magnetite by hematite is an important reaction during the hematite stage alteration (Bastrakov et al., 2007). Generally, this reaction can happen via two pathways: redox pathway and non-redox pathway (Mücke and Cabral, 2005; Otake et al., 2007). These two mechanisms result in huge difference on the product volume: the redox reaction causes 1.66% volume increase whereas the non-redox reaction causes 32.22% volume decrease (Mücke and Cabral, 2005).

It has long been proposed that in hematite-rich IOCG deposits, replacement of magnetite by hematite happens via oxidation reaction due to the oxidative nature of hematite stage fluids (e.g., Bastrakov et al., 2007; Schlegel et al., 2018). However, the increased brecciation intensity in hematite-rich ores (e.g., Olympic Dam, Ernest Henry, Oak Dam) indicates that the hematite-stage alteration should introduce porosity, which is hard to explain by the oxidative reaction pathway (redox) that causes increased crystal volume.

Increased ore porosity can facilitate fluid flow and thus boost alteration (Altree-Williams et al., 2015). Therefore, apart from the possibility that hematite-stage fluids may introduce extra metals, the transformation from magnetite to hematite may also contribute to the Cu-Au mineralization by increasing porosity in the ore. By far, however, mechanisms of this particular transformation reaction are not well understood. Moreover, in IOCG hydrothermal systems, due to the existence of many redox sensitive components, such as Ce^{3+}, the reaction may happen in a totally different way than idealized conditions (e.g., Mücke and Cabral, 2005). As different reaction mechanisms can result in huge difference on the product texture (e.g., Altree-Williams et al., 2015), the nature of the fluids that are responsible for the observed reaction textures is hard to predict empirically with our current knowledge and requires further experimental and theoretical study.

1.3 Thesis structure

This thesis consists of six chapters, including the introductory chapter. The thesis is formatted as a thesis by publication. Chapter 2, 3, and 5 that have already been published in peer-reviewed journals and Chapter 4 is close to submission and has been formatted in the form of stand-alone journal articles. As such, there are some unavoidable repetitions in the introduction and

discussion sections of this thesis, mainly about the research background. Chapter 2 has been published in *Chemical Geology* in January 2019. Chapter 3 has been published in *Geofluids* in August 2018. Chapter 5 has been published in *Geology* in February 2019. Chapter 6 is the conclusion chapter that summarizes the main results of the thesis.

Chapter 2 investigates the role of fluorine in mobilizing Fe, U and REE and its influence on the formation of IOCG deposits. In this chapter, we report the first results from in-situ synchrotron XAS experiments on Fe-F complexation up to 450 ºC. Combining the experimental data and thermodynamic calculations, we discussed the role of F in the formation of IOCG deposits in the following aspects: (1) transporting Fe, U and REE; (2) precipitation of Fe; (3) the source link between ore fluids and the host rocks; and (4) enhancing permeability of the breccia and the wall rocks. The results show that: (1) fluoride is not a good transporting ligand for Fe and U but can contribute to U and REE mobility by affecting fluid chemistry; (2) fluoride may help precipitate Fe in IOCG deposits; (3) HF(aq) is the predominant fluoride species in fluids at T>300 ºC and can help increase silicate solubility; (4) the F-rich host granite can provide F to the ore fluids through fluid-rock interactions.

Chapter 3 reviews the thermodynamic properties of U(IV/VI)-F, U(IV/VI)-Cl, and U(IV/VI)-OH aqueous complexes. Based on this, we calculate the solubility of uraninite and U_3O_8(s) in acidic F-bearing solutions (Cl:F = 100, ppm based) at 25-450 ºC, 600 bar, which aims to compare the relative importance of F and Cl in the hydrothermal transport of U. We further use reactive transport modelling to simulate the alteration of low-Cu-U magnetite-dominated ores by hematite-stable fluids. The results show that: (1) U(IV)-F complexes and U(VI)-F complexes are predominant at T<250ºC, whereas above 250ºC, U(IV/VI) chloride complexes are predominant; (2) extensive alteration of low-grade magnetite-chalcopyrite ores by low temperature, oxidized fluids is an effective mechanism for forming ore-grade Cu-U mineralization; (3) F plays a less important role in controlling metal endowments in IOCG deposits, and the co-enrichment of F and U in IOCG ores can be achieved via second stage alteration and upgrading processes.

Chapter 4 investigates the transformation reaction of magnetite to hematite in acidic solutions under hydrothermal conditions (200 ºC). Trace amount of REE (La, Ce and Nd) are doped in the solution to see the possible effects from interconversion of Ce(III) and Ce(IV) on the replacement reaction. The results show that the presence of Ce increases the porosity of hematite formed in high-grade IOCG ores. Therefore trace amounts of Ce can increase the efficiency of the coupling between mineral reaction, fluid flow, and element mass transfer, catalysing and enhancing the ore formation process.

Chapter 5 presents the first thermodynamic model for arsenic in the solid solutions of pyrite and arsenopyrite and uses it to evaluate the partitioning behaviour of arsenic during fluid-mineral equilibria. This model makes it possible to use arsenic as a proxy of gold in hydrothermal gold systems. Based on this model, we perform reactive transport modelling and for the first time show that the widely observed As-Au enrichment in the alteration rims of arsenian pyrite can be formed by protracted alteration of low-As-Au fluids, which drives dissolution and reprecipitation of pre-existing minerals and results in supersaturation of As-Au in a local scale.

Chapter 6 summarizes the results and the findings of this thesis. Overall, this thesis integrates the findings from thermodynamic modelling and hydrothermal experiments and shows several aspects of fluid-rock interaction and how they contribute to the formation of large ore deposits. These include influence from F in metal mobilization, magnetite to hematite transformation reaction, arsenic in pyrite and arsenopyrite solid solutions, and remobilization and upgrading of metals by extensive hydrothermal fluid flows.

1.4 References

Altree-Williams, A., Pring, A., Ngothai, Y., and Brugger, J., 2015, Textural and compositional complexities resulting from coupled dissolution–reprecipitation reactions in geomaterials: Earth-Science Reviews, v. 150, p. 628-651.

Bastrakov, E., Jaireth, S., and Mernagh, T., 2010, Solubility of Uranium in hydrothermal fludis at 25º to 300ºC: Geoscience Australia, v. 29, no. 70633.

Bastrakov, E. N., Skirrow, R. G., and Davidson, G. J., 2007, Fluid Evolution and Origins of Iron Oxide Cu-Au Prospects in the Olympic Dam District, Gawler Craton, South Australia: Economic Geology, v. 102, p. 1415-1440.

Bateman, R., and Hagemann, S., 2004, Gold mineralisation throughout about 45 Ma of Archaean orogenesis: protracted flux of gold in the Golden Mile, Yilgarn craton, Western Australia: Mineralium Deposita, v. 39, p. 536-559.

Brugger, J., Lahaye, Y., Costa, S., Lambert, D., and Bateman, R., 2000, Inhomogeneous distribution of REE in scheelite and dynamics of Archaean hydrothermal systems (Mt. Charlotte and Drysdale gold deposits, Western Australia): Contributions to Mineralogy and Petrology, v. 139, no. 3, p. 251-264.

Brugger, J., Pring, A., Reith, F., Ryan, C., Etschmann, B., Liu, W. H., O'Neill, B., and Ngothai, Y., 2010, Probing ore deposits formation: New insights and challenges from synchrotron and neutron studies: Radiation Physics and Chemistry, v. 79, no. 2, p. 151-161.

Brugger, J., Liu, W., Etschmann, B., Mei, Y., Sherman, D. M., and Testemale, D., 2016, A review of the coordination chemistry of hydrothermal systems, or do coordination changes make ore deposits?: Chemical Geology, v. 447, p. 219-253.

Campbell, I. H., Ballard, J. R., Palin, J. M., Allen, C., and Faunes, A., 2006, U-Pb zircon geochronology of granitic rocks from the Chuquicamata-El Abra porphyry copper belt

of northern Chile: Excimer laser ablation ICP-MS analysis: Economic Geology, v. 101, no. 7, p. 1327-1344.

Cline, J. S., Hofstra, A. H., Muntean, J. L., Tosdal, R. M., and Hickey, K. A., 2005, Carlin-Type Gold Deposits in Nevada: Critical Geologic Characteristics and Viable Models: Economic Geology 100th Anniversary Volume, p. 451-484.

Cockerton, A. B. D., and Tomkins, A. G., 2012, Insights into the Liquid Bismuth Collector Model Through Analysis of the Bi-Au Stormont Skarn Prospect, Northwest Tasmania: Economic Geology, v. 107, no. 4, p. 667-682.

Davidson, G. J., Paterson, H., Meffre, S., and Berry, R. F., 2007, Characteristics and Origin of the Oak Dam East Breccia-Hosted, Iron Oxide Cu-U-(Au) Deposit: Olympic Dam Region, Gawler Craton, South Australia: Economic Geology, v. 102, p. 1471-1498.

Deditius, A. P., Reich, M., Kesler, S. E., Utsunomiya, S., Chryssoulis, S. L., Walshe, J., and Ewing, R. C., 2014, The coupled geochemistry of Au and As in pyrite from hydrothermal ore deposits: Geochimica et Cosmochimica Acta, v. 140, p. 644-670.

Fougerouse, D., Micklethwaite, S., Tomkins, A. G., Mei, Y., Kilburn, M., Guagliardo, P., Fisher, L. A., Halfpenny, A., Gee, M., Paterson, D., and Howard, D. L., 2016, Gold remobilisation and formation of high grade ore shoots driven by dissolution-reprecipitation replacement and Ni substitution into auriferous arsenopyrite: Geochimica et Cosmochimica Acta, v. 178, p. 143-159.

Fougerouse, D., Micklethwaite, S., Ulrich, S., Miller, J., Godel, B., Adams, D. T., and McCuaig, T. C., 2017, Evidence for Two Stages of Mineralization in West Africa's Largest Gold Deposit: Obuasi, Ghana: Economic Geology, v. 112, no. 1, p. 3-22.

Goldfarb, R. J., and Groves, D. I., 2015, Orogenic gold: Common or evolving fluid and metal sources through time: Lithos, v. 233, p. 2-26.

Gow, P. A., Wall, V. J., Oliver, N. H. S., and Valenta, R. K., 1994, Proterozoic iron oxide (Cu-U-Au-REE) deposits: Further evidence of hydrothermal origins: Geology, v. 22, no. 7, p. 633-636.

Groves, D. I., and Santosh, M., 2015, Province-scale commonalities of some world-class gold deposits: Implications for mineral exploration: Geoscience Frontiers, v. 6, no. 3, p. 389-399.

Groves, D. I., Goldfarb, R. J., and Santosh, M., 2016, The conjunction of factors that lead to formation of giant gold provinces and deposits in non-arc settings: Geoscience Frontiers, v. 7, no. 3, p. 303-314.

Haynes, D., Cross, K., Bills, R., and Reed, M. H., 1995, Olympic Dam Ore Genesis: A Fluid-Mixing Model: Economic Geology, v. 90, p. 281-307.

Heinrich, C. A., and Candela, P. A., 2014, Fluids and Ore Formation in the Earth's Crust, p. 1-28.

Hitzman, M., Oreskes, N., and Einaudi, M., 1992, Geological characteristics and tectonic setting of Proterozoic iron oxide (Cu-U-Au-REE) deposits: Precambrian Research, v. 58, p. 241-287.

James-Smith, J., Cauzid, J., Testemale, D., Liu, W. H., Hazemann, J. L., Proux, O., Etschmann, B., Philippot, P., Banks, D., Williams, P., and Brugger, J., 2010, Arsenic speciation in fluid inclusions using micro-beam X-ray absorption spectroscopy: American Mineralogist, v. 95, no. 7, p. 921-932.

Li, K., Pring, A., Etschmann, B., Macmillan, E., Ngothai, Y., O'Neill, B., Hooker, A., Mosselmans, F., and Brugger, J., 2015, Uranium scavenging during mineral replacement reactions: American Mineralogist, v. 100, no. 8-9, p. 1728-1735.

McPhie, J., Kamenetsky, V., Allen, S., Ehrig, K., Agangi, A., and Bath, A., 2011, The fluorine link between a supergiant ore deposit and a silicic large igneous province: Geology, v. 39, no. 11, p. 1003-1006.

Meffre, S., Large, R. R., Steadman, J. A., Gregory, D. D., Stepanov, A. S., Kamenetsky, V. S., Ehrig, K., and Scott, R. J., 2016, Multi-stage enrichment processes for large gold-bearing ore deposits: Ore Geology Reviews, v. 76, p. 268-279.

Migdisov, A., Williams-Jones, A. E., Brugger, J., and Caporuscio, F. A., 2016, Hydrothermal transport, deposition, and fractionation of the REE: Experimental data and thermodynamic calculations: Chemical Geology, v. 439, p. 13-42.

Mikucki, E. J., 1998, Hydrothermal transport and depositional processes in Archean lode-gold systems: A review: Ore Geology Reviews, v. 13, no. 1-5, p. 307-321.

Mücke, A., and Cabral, A. R., 2005, Redox and nonredox reactions of magnetite and hematite in rocks: Chemie der Erde - Geochemistry, v. 65, no. 3, p. 271-278.

Mueller, A. G., 2015, Structure, alteration, and geochemistry of the Charlotte quartz vein stockwork, Mt Charlotte gold mine, Kalgoorlie, Australia: time constraints, down-plunge zonation, and fluid source: Mineralium Deposita, v. 50, no. 2, p. 221-244.

Otake, T., Wesolowski, D. J., Anovitz, L. M., Allard, L. F., and Ohmoto, H., 2007, Experimental evidence for non-redox transformations between magnetite and hematite under H2-rich hydrothermal conditions: Earth and Planetary Science Letters, v. 257, no. 1-2, p. 60-70.

Pearson, R., 1963, Hard and Soft Acids and Bases: Journal of the American Chemical Society, v. 85, p. 3533-3539.

Putnis, A., 2009, Mineral Replacement Reactions: Reviews in Mineralogy and Geochemistry, v. 70, no. 1, p. 87-124.

Reich, M., Kesler, S. E., Utsunomiya, S., Palenik, C. S., Chryssoulis, S. L., and Ewing, R. C., 2005, Solubility of gold in arsenian pyrite: Geochimica Et Cosmochimica Acta, v. 69, no. 11, p. 2781-2796.

Richards, J. P., 2013, Giant ore deposits formed by optimal alignments and combinations of geological processes: Nature Geoscience, v. 6, no. 11, p. 911-916.

Saunders, J. A., Hofstra, A. H., Goldfarb, R. J., and Reed, M. H., 2014, Geochemistry of Hydrothermal Gold Deposits, p. 383-424.

Schlegel, T. U., Wagner, T., Walle, M., and Heinrich, C. A., 2018, Hematite Breccia-Hosted Iron Oxide Copper-Gold Deposits Require Magmatic Fluid Components Exposed to Atmospheric Oxidation: Evidence from Prominent Hill, Gawler Craton, South Australia: Economic Geology, v. 113, no. 3, p. 597-644.

Seward, T. M., and Barnes, H. L., 1997, Chapter 9: metal transport by hydrothermal ore fluids., Geochemistry of Hydrothermal Ore Deposits, John Willey & Sons, p. 435-486.

Seward, T. M., Williams-Jones, A. E., and Migdisov, A. A., 2014, The Chemistry of Metal Transport and Deposition by Ore-Forming Hydrothermal Fluids, Treatise on Geochemistry, p. 29-57.

Sibson, R. H., Moore, J. M., and Rankin, A. H., 1975, Seismic pumping – a hydrothermal fluid transport mechanism: Journal of the Geological Society, v. 131, p. 653-659.

Sillitoe, R. H., 2010, Porphyry Copper Systems: Economic Geology, v. 105, p. 3-41.

Sung, Y. H., Brugger, J., Ciobanu, C. L., Pring, A., Skinner, W., and Nugus, M., 2009, Invisible gold in arsenian pyrite and arsenopyrite from a multistage Archaean gold deposit: Sunrise Dam, Eastern Goldfields Province, Western Australia: Mineralium Deposita, v. 44, no. 7, p. 765-791.

Thomas, H. V., Large, R. E., Bull, S. W., Maslennikov, V., Berry, R. F., Fraser, R., Froud, S., and Moye, R., 2011, Pyrite and Pyrrhotite Textures and Composition in Sediments, Laminated Quartz Veins, and Reefs at Bendigo Gold Mine, Australia: Insights for Ore Genesis: Economic Geology, v. 106, no. 1, p. 1-31.

Tooth, B., Brugger, J., Ciobanu, C., and Liu, W., 2008, Modeling of gold scavenging by bismuth melts coexisting with hydrothermal fluids: Geology, v. 36, no. 10, p. 815-818.

Williams, P. J., Barton, M., Johnson, D., Fontbote, L., Haller, A., Mark, G., Oliver, N., and Marschik, R., 2005, Iron Oxide Copper-Gold Deposits: Geology, Space-Time Distribution , and Possible Modes of Origin: Economic Geology, v. 100th Anniversary Volume, p. 371-405.

Williams-Jones, A. E., Samson, I. M., and Olivo, C. R., 2000, The Genesis of Hydrothermal Fluorite-REE Deposits in the Gallinas Mountains, New Mexico: Economic Geology, v. 95, p. 327-342.

Xia, F., Brugger, J., Chen, G., Ngothai, Y., O'Neill, B., Putnis, A., and Pring, A., 2009, Mechanism and kinetics of pseudomorphic mineral replacement reactions: A case study of the replacement of pentlandite by violarite: Geochimica et Cosmochimica Acta, v. 73, no. 7, p. 1945-1969.

Chapter 2

The role of fluorine in hydrothermal mobilization and transportation of Fe, U and REE and the formation of IOCG deposits

Yanlu Xing[1], Barbara Etschmann[1], Weihua Liu[2], Yuan Mei[1,2], Yuri Shvarov[3], Denis Testemale[4], Andrew Tomkins[1] and Joël Brugger[1,*]

1. School of Earth, Atmosphere and the Environment, Monash University, Clayton, VIC 3800, Australia

2. CSIRO Mineral Resources, Clayton, VIC 3168, Australia

3. Lomonosov Moscow State University, Moscow, Russia

4. CNRS, Université Grenoble Alpes, Institut NEEL, F-38000 Grenoble, France

Chemical Geology 504 (2019) 158–176

Contents lists available at ScienceDirect

Chemical Geology

journal homepage: www.elsevier.com/locate/chemgeo

The role of fluorine in hydrothermal mobilization and transportation of Fe, U and REE and the formation of IOCG deposits

Yanlu Xing[a], Barbara Etschmann[a], Weihua Liu[b], Yuan Mei[a,b], Yuri Shvarov[c], Denis Testemale[d], Andrew Tomkins[b], Joël Brugger[a,*]

[a] School of Earth, Atmosphere and Environment, Monash University, Clayton, VIC 3800, Australia
[b] CSIRO Mineral Resources Flagship, Clayton, VIC 3168, Australia
[c] Lomonosov Moscow State University, Moscow, Russia
[d] CNRS, Université Grenoble Alpes, Institut NEEL, F-38000 Grenoble, France

ARTICLE INFO

Editor: Johannesson K

Keywords:
Fluorine
XAS
Complexing
IOCG
Hydrothermal transport and deposition
Reactive transport modelling

ABSTRACT

The fluorine(F)-rich nature in iron oxide-copper-gold (IOCG) deposits has received much attention since it was recognized that the giant Olympic Dam (OD) deposit contains > 2 wt% fluorite. Yet, the significance of the F-U-REE-Fe association remains poorly understood, with four existing hypotheses regarding the role of F: (**i**) fluoride increases the solubility of metals by forming stable aqueous complexes; (**ii**) fluoride acts as a precipitating rather than a transporting agent, due to the low solubility of some fluoride minerals; (**iii**) high F contents may simply reflect the source of the ore fluids; and (**iv**) the presence of HF(aq) in acidic aqueous solutions may improve leaching of metals and create fluid pathways. In this study, we investigated these hypotheses using thermodynamic modelling, and performed complementary experiments to evaluate the nature and stability of Fe(II/III)-F complexes at elevated temperature.

Our in-situ X-ray absorption spectroscopy (XAS) data show that at room temperature, the Fe(II/III) fluoride complexes are more stable than corresponding Fe(II/III) chloride complexes, and the Fe(III) fluoride complexes are important in F-only solutions at low temperature (≤100 °C). Increasing temperature causes precipitation of Fe from F-only solutions, so that above 200 °C there was little detectable Fe left in the solution. In mixed F-Cl solutions, the experimental data and the thermodynamic calculations show that Fe(III)-F complexes are important at low temperature (~≤150 °C) while Fe(II)-Cl complexes predominate at temperatures higher than 200 °C, causing an increase in Fe solubility.

We further investigated the potential of granitic rocks as a source for F and metals (Fe, REE and U) using thermodynamic calculations (hypotheses (**i**), (**ii**) and (**iii**)). Our results show that U and La solubilities are mainly controlled by temperature: U solubility is relatively high at $T < 200$ °C; La solubility is relatively high at $T > 250$ °C. Fluoride significantly enhances the solubility of U and La compared to F-free system by affecting fluid chemistry or forming stable complexes (La).

Our simulations also show that Si solubility is enhanced in F-bearing solutions (hypothesis (**iv**)), mainly attributed to the increased solubility of $H_3SiO_4^-$ and $NaHSiO_3$(aq). Moreover, the solubility of Si-F increases dramatically. These indicate that F may help breaking the Si—O bond in silicates and releasing Si into fluids. Therefore, fluorine may play a key role in enhancing the porosity of the wall rock and breccia, and in mineral replacement reactions. Collectively, these would enhance fluid-rock reaction, and thus may help to drive metal precipitation.

Overall, the thermodynamic considerations suggest that the common F + Fe + REE ± U association in IOCGs may not only reflect the source of the metals, but also that F contributes to the metal endowment of some IOCG deposits via a combination of processes, including increasing the metal (U and REE, but not Fe) carrying capacity of the fluids; and dissolving silicates and enhancing the porosity of the breccia and the wall rocks, thus contributing to increased fluid pathways and ore-forming reactions.

* Corresponding author.
E-mail address: joel.brugger@monash.edu (J. Brugger).

https://doi.org/10.1016/j.chemgeo.2018.11.008
Received 1 July 2018; Received in revised form 2 November 2018; Accepted 13 November 2018
Available online 17 November 2018

1. Introduction

Fluorine is enriched in many hydrothermal mineralizing systems, such as Iron Oxide-Copper-Gold (IOCG), Iron Oxide-Apatite (IOA) and REE deposits (Chen and Zhou, 2014; Hitzman et al., 1992; Montreuil et al., 2016; Pollard, 2000; Sillitoe, 2003; Smith and Henderson, 2000; Williams et al., 2005). Generally, F is widely distributed within these mineralized systems in the form of both fluorite and F-bearing minerals such as apatite, chlorite and biotite. The scale of the association between F and IOCG deposits has been highlighted for the supergiant Olympic Dam (OD) deposit (McPhie et al., 2011a), but extends to most IOCG (e.g., Prominent Hill, South Australia; Fab IOCG system, Canada; Lala deposit, South-West China; Chen and Zhou, 2015; McPhie et al., 2011a; Montreuil et al., 2016; Oreskes and Einaudi, 1990; Skirrow et al., 2007; Schlegel and Heinrich, 2015). At OD, the extracted ore contains ~2.5 wt% fluorite, adding up to ~100 Mt F (world production of F is ~5 Mt/year; McPhie et al., 2011a). Large amounts of F are also present in hydrothermal alteration minerals at OD, such as chlorite, sericite and apatite (Agangi et al., 2012; McPhie et al., 2011b). These studies relaunched the debate on the role of F in the generation of IOCG deposits. Similarly to OD, other IOCG, IOA (e.g., Grängesberg Mining District, Sweden; Jonsson et al., 2013) and REE deposits (e.g., Bayan Obo; Smith and Henderson, 2000; Ling et al., 2013) generally display an association between REE and Fe mineralization and F-bearing minerals, suggesting a F-rich nature of the mineralizing fluids (Salvi and Williams-Jones, 1996). Fluorine-bearing minerals such as bastnäsite-(Ce) and florencite-(Ce) usually make up the major REE ore phases at these deposits.

Although the association between F and REE is well established, the significance of F for the genesis of IOCG, IOA and REE deposits is still a subject of debate. Four main explanations have been proposed, which may work individually or in combination (Keppler, 1993; McPhie et al., 2011a; Williams-Jones et al., 2000).

(i) Fluoride (F^-) can increase the solubility of metals by forming stable coordination complexes. According to Hard-Soft Acid Base (HSAB) theory (Pearson, 1963), F^- is classified as a hard ligand that forms strong complexes with hard cations such as Fe^{3+}, REE^{3+} (Seward and Barnes, 1997; Williams-Jones et al., 2000) and U(IV/VI) (Bastrakov et al., 2010). In contrast, significant Cu(I)–F and Au(I)–F complexation is not expected because Cu(I) and Au(I) are soft bases that form stable complexes with soft acids such as HS^-. Keppler and Wyllie (1991) showed that U prefers to partition into the aqueous fluids with increasing HF content by forming U-F complexes during fluid-melt equilibrium. Furthermore, McGloin et al. (2016) revealed the close association between U and F enrichment in the source regions of orogenic U ores; they proposed that F-bearing saline fluids are the key to forming U mineralization, since F helps to release U from a granitic batholith. Moreover, it has long been proposed that F^- is an important transporting ligand for REE (McPhie et al., 2011a; Oreskes and Einaudi, 1990; Williams-Jones et al., 2000), due to the theoretically predicted formation of strong REE-fluoride complexes (Haas et al., 1995). Williams-Jones et al. (2000) proposed that for F contents between 10^{-5} and 10^{-1} m (ca. 0.01 ppm – 0.2%), thought to be realistic ore fluids, REEs are predominantly transported in the form of fluoride complexes.

McPhie et al. (2011a) suggested that F-rich hydrothermal fluids are responsible for the high metal contents at OD. This raises the possibility that some base metals may also be transported as fluoride complexes. For example, Fe^{3+} is a hard metal, and Fe^{2+} is classified as having intermediate hard-soft character. Room-temperature (25 °C) formation constants indicate that fluoride complexes are stronger than chloride complexes for both Fe^{2+} and Fe^{3+} (Sverjensky et al., 1997; Tagirov et al., 2000); however, this is yet to be confirmed at elevated temperatures. There is no experimental data on the temperature dependence of Fe(II/III)-F complexation.

(ii) Based on recent experimental data for REEs solubilities, Williams-Jones et al. (2012) proposed a new paradigm for the role of F in REE mineralization, by demonstrating that F acts as a precipitating barrier rather and a transporting agent under conditions typical for the formation of many hydrothermal REE deposits, such as the Bayan Obo deposit. They also suggested that REE-chloride complexes are the most important complexes for the hydrothermal transportation of REE, as a result of the prevalence of chloride ions in natural fluids, the high stability of the HF(aq) ion pair, and the extremely low solubility of REE-fluoride minerals at elevated temperature. This led Chen and Zhou (2014) to suggest a new explanation for the correlation between fluorite and REE mineralization at the Lala Fe-Cu-(REE) IOCG deposit in southwest China. Following Williams-Jones et al. (2012), they pointed out that instead of helping REE transport, the elevated concentration of F in fluids may be responsible for REE precipitation.

(iii) The high F contents of some deposits may reflect the source of the ore-forming fluids. For many IOCG deposits, close spatial and/or temporal connections are well established between felsic magmatic events and ore generation (Hitzman et al., 1992; Williams et al., 2005). For example, at OD, the Roxby Downs granite (RDG), which is classified as A-type granite and enriched in U, REE and F, is a potential source of U and REE (Ehrig et al., 2012; Johnson and Cross, 1995; Kontonikas-Charos et al., 2017; Skirrow et al., 2007). Recent U isotopic studies ($\delta^{238}U$) provide a direct evidence that at least part of the U at OD is sourced from the RDG (Kirchenbaur et al., 2016). An important feature is that these felsic wall rocks are also rich in F, which led McPhie et al. (2011a) to link the high concentration of F in the ores with fluids derived from the F-rich Mesoproterozoic Gawler silicic large igneous province (GSLIP). In the Lala deposit, it has been proposed that REE were derived from surrounding volcanic rocks (felsic and mafic), and that the fluids responsible for the main REE mineralization were all relatively enriched in F and of magmatic origin (Chen and Zhou, 2012; Chen and Zhou, 2015).

(iv) Fluorine may help dissolve silicates and create fluid pathways by forming HF(aq) in acidic aqueous solutions (Keppler, 1993). It is well known that HF(aq) is especially effective at breaking Si—O and M(metal)—O bonds in silicates and oxides (Kline and Fogler, 1981), which helps to dissolve silicates and oxides. In this case, the interaction between F-rich fluids and rocks may explain the rugged surface of the volcanic clasts in the OD breccia (McPhie et al., 2011a, 2012), and contribute to extensive brecciation and porosity.

In this study, we examine the possible mechanisms that can explain the association between F and base metal deposits, and in particular IOCG deposits, and address two significant knowledge gaps with new experimental data and thermodynamic modelling:

(1) To assess the role of F in metal transport in hydrothermal fluids, reliable thermodynamic properties of fluoride complexes of these metals, in particular Fe, REE, and U, are required (Brugger et al., 2016). A number of recent experimental studies have resulted in much improved thermodynamic properties for the transport of REE in F-Cl hydrothermal fluids (review by Migdisov et al., 2016). However, there are no experimental data available for hydrothermal Fe(II/III) fluoride complexation. Here, we provide the first experimental evidence for the nature and stability of Fe(II/III) fluoride complexes at elevated temperature (up to 450 °C) based on in-situ X-ray absorption spectroscopy (XAS) measurements. These experiments allow in-situ determination of stability and structural information of the dominant metal complexes (Brugger et al., 2007; Testemale et al., 2005).

(2) The available thermodynamic studies on reactive transport modelling and the sourcing of metals for IOCG deposit formation did not include F, REE or U (Bastrakov et al., 2007; Oliver et al., 2004). Given the common assumption that granitic rocks are good sources of U, REE and F, we conducted thermodynamic calculations to test the influences of F on the solubility of Fe, REE and U in aqueous solutions, and quantify the role of fluoride complexes in mobilizing metals through fluid-rock interaction over a wide temperature regime (50–450 °C). These calculations benefit from the new properties for Fe(II/III)-F complexes developed in the present study, and from the improved thermodynamic properties of REE complexes under hydrothermal conditions (Migdisov et al., 2016). Considering that biotite solid solution is a major F buffer, we included the non-ideal biotite mixing model of Zhu and Sverjensky (1992) in our calculations. The new modelling allows us to discuss the efficiency and likelihood of different processes that can explain the role of F in the formation of IOCG deposits.

2. Materials and methodology

2.1. In-situ XAS experiments

2.1.1. Solutions preparation

Sample solutions (Table 1) were prepared by dissolving FeF_2(s) and FeF_3(s) in acidified water (one drop of HCl/HBr/$HClO_4$) to ~50–80 mmol Fe concentration under nitrogen atmosphere. As O and F have a similar number of electrons and have similar X-ray cross sections, they are difficult to distinguish using XAS. In view of this, control experiments (e.g., Sols 2, 7, 11, 13, 16 and 18) were conducted with no F added in the solution, to determine the effect of F^- on the system via direct comparison with the chloride and bromide systems.

2.1.2. XAS measurements

Fe K-edge (7112 eV) fluorescence X-ray absorption near edge structure (XANES) and Extended X-ray absorption fine structure (EXAFS) data were collected at the European Synchrotron Research Facility (ESRF) in Grenoble, France, using beamline BM-30B (FAME) and the FAME high P-T XAS cell, which enables collection of high quality data on solutions up to supercritical conditions (Etschmann et al., 2016; Testemale et al., 2005; Tian et al., 2014). The spectroscopic autoclave consists of an external water-cooled high-pressure vessel equipped with three 1.5 mm thick beryllium windows enabling collection of fluorescence and transmission signals at a maximum pressure of ~600 bar. The sample was contained inside a glassy carbon tube with an internal diameter of 4 mm. The pressure was applied to the sample by two glassy carbon pistons, using helium as a pressure medium. The pressure is maintained within ± 0.2 bar during measurements using an automated regulation device (Bruyère et al., 2008). The glassy carbon tube was placed inside a small cylindrical resistive heater; the heater and tube are then installed inside the high-pressure vessel.

Table 1
Composition of the solutions studied by XAS.

Sample	Serial number	Conditions
FeF_3 (0.036 m) in 0.061 m $HClO_4$	Sol9	35–400 °C, 600 bar
FeF_3 (0.060 m) in 0.099 m HCl	Sol12	35–400 °C, 600 bar
$FeCl_2$ (0.050 m) in 4.23 m NaCl + 0.073 m HCl	Sol2	35–400 °C, 600 bar
$FeBr_2$ (0.106 m) in 4.20 m NaBr + 0.0023 m HBr	Sol11	35–400 °C, 600 bar
$FeCl_3$ (0.050 m) in 0.011 m HBr	Sol7	35–400 °C, 600 bar
$FeBr_2$ (0.070 m) in 0.0024 m HBr	Sol13	35–400 °C, 600 bar
$FeBr_2$ (0.071 m) in 1.05 m NaBr	Sol18	35–450 °C, 600 bar
$FeBr_2$ (0.116 m) in 10.08 m LiBr	Sol16	200–450 °C, 600 bar
FeF_2 (0.071 m) in 0.157 m $HClO_4$	Sol14	35–200 °C, 600 bar

Although the thermocouple sits near the sample, it is placed outside the glassy carbon tube and not exactly at the beam position. The solution temperature at the beam position was therefore calibrated by measurements of the density of water as a function of the thermocouple temperature at 600 bar (Etschmann et al., 2010, 2016; Liu et al., 2011), based on the equation of state of pure water (NIST database; Lemmon et al., 2000) and the X-ray mass attenuation coefficients tabulated by Chantler (1995). Based on this calibration, temperature accuracy is better that 3 °C. Temperature regulation maintains the temperature stable (within ≤0.2 °C) during data collection.

2.1.3. XAS data analysis

XANES and EXAFS data were analysed with the DEMETER package (Ravel and Newville, 2005), using FEFF version 8 (Rehr et al., 2009). Sols 9 and 12 were fitted in two ways: (i) the sum of the ligands was constrained to be between 4 and 6 (up to 200 °C) and to a maximum of 4.2 at 385 °C. However, this resulted in fits with four fluorine ligands at 35 and 93 °C. According to the thermodynamic modelling, there should be a maximum of three fluorine ligands, so the fits were repeated with the added constraint that the maximum number of fluorine ligands was three. While the goodness of fit (gof) parameters were slightly higher (but the difference was not statistically significant, Kelly et al., 2008), it is important to note that with this second constraint, the Fe(III)−O bond lengths (2.07 Å) were shorter than without this added constraint (2.15 Å). Hence the model constrained to ≤3 fluoride ligands is physically more reasonable, as from crystal structures Fe(III)−O bond lengths (2.05 Å for octahedral and 1.88 Å for tetrahedral geometry; Melnik et al., 1997) are shorter than Fe(II)−O bond lengths (~2.13 Å; Velbel, 1999).

XANES spectra of selected stoichiometries and geometries were simulated using the FDMNES package (Joly, 2001), following the procedure outlined in Brugger (2007), Testemale et al. (2009a, b) and Etschmann et al. (2010). The final states and resulting absorption cross-sections were calculated using the Finite Difference Method (FDM) to solve the Schrödinger equation. This method allows a totally free potential shape, thus avoiding the limitations imposed by the Muffin Tin (MT) approximation. Compared to methods that rely on the MT approximation, FDM is of particular interest for low symmetry and/or non-dense structures, as in the case of the aqueous complexes considered here (Etschmann et al., 2010).

Iron was soluble at room-T in Sol9 and Sol12 (Table 1), but the solubility decreased with increasing temperature. Iron concentrations in these solubility-limited runs were measured using the Fe step height in transmission ($\Delta\mu_{Fe}$) (e.g., Pokrovski et al., 2005; Etschmann et al., 2010), following

$$\Delta\mu_{Fe} = \Delta\sigma_{Fe} l M_{Fe} m_{Fe} d_{solution} \quad (1)$$

where $\Delta\sigma_{Fe}$ is the change of the total absorption cross-section over the Fe K-edge, taken from Chantler (1995); l is the optical path length travelled by the x-ray beam in the solution, which was determined from a measurement of a pure water sample; M_{Fe} is the atomic weight of Fe, m_{Fe} is the Fe aqueous concentration, and $d_{solution}$ is the density of the solution, approximated by the density of pure water since this study's solutions were relatively dilute.

2.2. Thermodynamic modelling

2.2.1. Software and source of thermodynamic properties

Most geochemical modelling was performed using the HCh package (Shvarov and Bastrakov, 1999), with Geochemist's Workbench (Bethke, 2008) being used mainly for creating activity-activity diagrams. The thermodynamic properties for minerals and aqueous species were sourced from an updated version of the Unitherm database (Shvarov and Bastrakov, 1999; Shvarov, 2008). Activity coefficients for charged aqueous species were calculated using the b-dot equation, which applies to ionic strengths of ~1 with high accuracy, and up to ~4 with

reduced accuracy (Helgeson and Kirkham, 1974; Shvarov and Bastrakov, 1999). HCh uses a Gibbs free energy minimisation approach for calculating the equilibrium rock and fluid compositions, and can handle solution density ≥ 0.35 g/cm^3 over a P-T range of 0–1000 °C and up to 5000 bar following the limitations of the Helgeson-Kirkham-Flowers (HKF) equation of state (Tanger and Helgeson, 1988).

In addition to the HKF formalism, the Unitherm database allows to describe the P-T change in energetics of aqueous species using the modified Ryzhenko–Bryzgalin (MRB) model (Borisov and Shvarov, 1992; Ryzhenko et al., 1985; Shvarov, 2015), which allows incorporation of species for which little information is available. MRB parameters were fitted to available stability constants using the OptimC program (Shvarov, 2015). The empirical MRB model describes the P-T dependence of the dissociation constant ($pK = -\log K$) of aqueous complexes as:

$$pK(T, P) = 298.15/T \cdot pK_{298°C,1bar} + f(T, P) \cdot (zz/a)_{eff} \quad (2)$$

where $pK_{298°C,1bar}$ is usually derived from experiments; T is the absolute temperature (K), P is pressure; $f(T, P)$ is a species-independent function that includes the dissociation constant of water; and $(zz/a)_{eff}$ is the temperature-dependant effective property of the complex (Ryzhenko et al., 1985; Shvarov, 2015). In the Unitherm database, $(zz/a)_{eff}$ is expressed as:

$$(zz/a)_{eff} = A + B/T \quad (3)$$

where A and B are empirical constants and T is the temperature in Kelvin (K).

The list of species used in the model and the source of thermodynamic properties are given in the Supplementary Material (Appendix 1). Hereby we briefly describe the major sources of thermodynamic data:

(i) We included the pure minerals, solid solutions, and aqueous species (in particular Cu, Au, Fe complexes) selected by Zhong et al. (2015a, b).
(ii) F-bearing endmembers of biotite and apatite are from Zhu and Sverjensky (1991).
(iii) F^- and HF(aq) properties are selected from Migdisov et al. (2016).
(iv) Properties for REE chloride, fluoride and hydroxide complexes are selected from the recent review of Migdisov et al. (2016).
(v) Uranium minerals and aqueous species are based on the Nuclear Energy Agency (NEA) review (Guillaumont et al., 2003) and the recommended values of Bastrakov et al. (2010) and Xing et al. (2018).
(vi) Stability constants for the formation of Fe(III) and Fe(II) fluoride complexes were extrapolated in this study – see Section 3.1.

2.2.2. Biotite and apatite solid solutions

Biotite and apatite account for a major part of F in granites, and are expected to play a significant role in buffering the F-Cl-OH contents of the fluids through fluid-rock interactions (Zhu and Sverjensky, 1992). We used an ideal mixing model to describe F-Cl-OH in apatite, following Zhu and Sverjensky (1992), who demonstrated good agreement with natural samples using this approach. Ideality is not a valid assumption for biotite, however, since nuclear magnetic resonance spectroscopy indicates that hydroxyl (OH^-) preferentially clusters around Fe in one type of domain, and F clusters around Mg in another type of domain (Munoz, 1984), resulting in the positive correlations between (Mg/Fe) ratio and F observed in natural biotite (e.g., Finch and Tomkins, 2017). In the present study, we modelled the biotite solid solution considering the F-OH partitioning between its Fe-Mg endmembers (annite and phlogopite) based on the reciprocal solid solution model described by Zhu and Sverjensky (1992). Note that Cl endmembers are not considered because of their very low concentration in natural biotites. In this case, our modelled biotite solid solution consists of annite, fluoroannite, phlogopite and fluorophlogopite (nomenclature following Rieder et al., 1998). The excess Gibbs free energy of mixing calculated using the equations of Zhu and Sverjensky (1992) were fitted to an empirical Redlich-Kister model that is compatible with the HCh free energy minimisation approach. Details of the implementation in the HCh model are given in the Supplementary Material (Appendix 1). The three endmembers for apatite solid solution are apatite-(CaOH), apatite-(CaF) and apatite-(CaCl) (nomenclature following Pasero et al., 2010).

2.2.3. REE minerals

Bastnäsite-(Ce) is the most abundant and widespread REE mineral phase at OD (Oreskes and Einaudi, 1990). In fact, in many large REE reserves, fluorocarbonate minerals, i.e., bastnäsite-(Ce), are usually the predominant REE phase (Smith and Henderson, 2000; Williams-Jones et al., 2012). Therefore, reliable thermodynamic properties of bastnäsite-(Ce) and other REE fluorocarbonate minerals are required for accurate modelling of REE and F mobility during fluid-rock interactions. However, the thermodynamic properties for REE fluorocarbonate minerals are scarce. In the present study, properties used for bastnäsite-(Ce) and parisite-(Ce) are estimated by Gysi and Williams-Jones (2015) based on the results of differential scanning calorimetric experiments conducted at 323–1022 K (Kelvin), 1 bar, which are the only reported thermodynamic data for calculations of REE fluorocarbonate solubility at elevated temperature. The stoichiometric formulae for bastnäsite-(Ce) is $Ce_{0.5}La_{0.25}Nd_{0.2}Pr_{0.05}CO_3F$, and for parisite-(Ce) is $CaCe_{0.95}La_{0.6}Nd_{0.35}Pr_{0.1}(CO_3)_3F_2$.

2.2.4. Simulations of fluid-granite interaction

We modelled the fluid-rock interaction with the assumption that hydrothermal fluids can leach metals from host felsic rocks and transport them to form mineralization. We used the aliquot-type model to calculate fluid-granite equilibrium (Oliver et al., 2004; Zhong et al., 2015a; Fig. 1). This model provides an estimate of the equilibrium composition of hydrothermal fluids and altered rocks under various P-T-salinity conditions for fluid-rock interaction. In our modelling, we reacted 1 kg of water (H_2O) with ~1 kg granite (fluid/rock = 1). The composition of the granite used for modelling (Table 2) is based on reported whole rock geochemical data of the silicic Gawler Range volcanics and RDG (Agangi et al., 2012; Ehrig et al., 2012). The fluid salinity was controlled at 0–20 wt% NaCl, i.e. 0–3.5 m Cl_{tot}. Calculations were conducted at 50–450 °C with a fixed pressure of 3000 bar; pressure has little effect on the model predictions as long as fluid

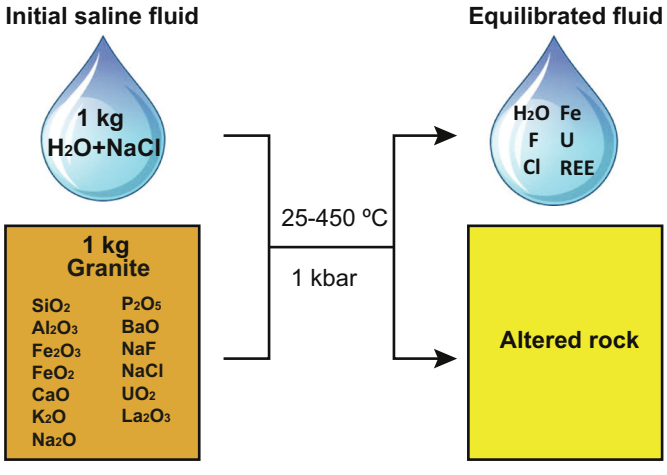

Fig. 1. Conceptual model used for geochemical simulation of fluid-rock interaction with HCh, which is simple aliquot-type mixing of 1 kg saline water with granite to produce equilibrated composition of fluid and the altered rock. Salinity of the initial fluid was controlled from 0 to 20 wt% NaCl equiv. Equilibrated composition of fluid and rock were calculated from 25 to 450 °C at a fixed pressure of 1 kbar.

Table 2
Granite composition used in the simulation (based on Agangi et al., 2012; Ehrig et al., 2012).

Components	Granite with F (wt%)	Granite with no F (wt%)
SiO_2	69.60	69.60
Al_2O_3	13.37	13.37
Fe_2O_3	1.70	1.70
FeO	1.50	1.50
MgO	0.83	0.57
CaO	0.57	0.85
Na_2O	3.40	3.40
K_2O	5.53	5.53
P_2O_5	0.07	0.07
CO_2	0.27	0.27
FeS_2	0.094	0.094
CaF_2	0.39	0
NaCl	0.057	0.057
H_2O	2.00	2.00
La_2O_3	0.0117	0.0117
Ce_2O_3	0.025	0.025
Nd_2O_3	0.007	0.007
U_3O_8	1.30E-03	1.30E-03

Calculated mineralogical composition at 450 °C, 3 kbar: 29.7% Albite, 29.6% Microcline, 27.8% Quartz, 4.3% Biotite, 3.9% Anorthite, 2.7% Magnetite, 1.7% Muscovite, 0.2% Apatite, 0.1% Pyrrhotite.

density remains > ~0.8 g cm^{-3} (e.g., Liu et al., 2008). Moreover, to investigate the effects of F, calculations were performed under both F-bearing (with a normal RDG) and F-free (F removed from a normal RDG) systems (Table 2).

3. Stability of Fe(II/III) fluoride complexes in hydrothermal fluids

We assessed the available thermodynamic data for Fe fluoride complexes and extrapolated their properties to elevated temperatures. In this section, we report our newly extrapolated properties of Fe fluoride complexes, as well as the new experimental data to cross-check the theoretical results.

3.1. Thermodynamic properties for Fe(II/III) fluoride complexes at room temperature

Experimental studies on Fe(II/III)-F complexation are scarce, and to date available only at room temperature. Formation constants for the Fe(III)-F complexes including FeF^{2+}, FeF_2^+, FeF_3(aq) and FeF_4^- at 25 °C from previous studies are listed in Table 3. We calculated the formation constants reported by Soli and Byrne (1996) and Walker and Choppin (1967) to zero ionic strength (log$K$ at I = 0; details in Appendix 1). The calculated log$K$ for Fe(III)F^{2+} constant based on Soli and Byrne (1996) and Walker and Choppin (1967) are in good agreement (within 0.5 log unit), and are also very close to values calculated with the HKF model of Sverjensky et al. (1997) (Table 3). For Fe(III)F_2^+ and Fe(III)F_3(aq), the data presented by Soli and Byrne (1996) and (Soli and Byrne, 1996; Walker and Choppin, 1967) are in excellent agreement (within 0.2 log unit).

Table 3
Equilibrium constants for the formation of Fe(III/II)-F complexes at 25 °C, 1 bar (at zero ionic strength).

Aqueous species	log$K$			
FeF^{2+}		6	5.9	6.44
FeF_2^+			11.03	11.2
FeF_3(aq)			14.25	14.42
FeF_4^-			16.03	
FeF^+	1.7	1.43		
Reference	Lemire et al., 2013	Sverjensky et al., 1997	Calculated from Soli and Byrne (1996)	Calculated from Walker and Choppin (1967)

Note: log$K$ values for high order Fe(II)-F complexes are reported by Wells and Salam (1967), which are $\log K_{FeF_2}$ = 2.30 (298.15 K) and $\log K_{FeF_3^-}$ = 2.72 (273.15 K). Details for log$K$ extrapolation are described in the Supplementary material.

The recent NEA review (Lemire et al., 2013) concluded that Fe(II)F^+ is currently the only Fe(II) fluoride complex for which a reliable formation constant can be selected, and recommended a value of 1.7 ± 0.2 for $\log K_{FeF+}$. This value is similar to Sverjensky et al. (1997)'s value (log$K$ = 1.43). Higher order Fe(II) fluoride complexes including FeF_2(aq) and FeF_3^- were reported only by Wells and Salam (1967). However, as argued by Lemire et al. (2013), the speciation derived by Wells and Salam (1967) is likely to be in error, since (1) their data analysis procedures are unclear; (2) the proposed temperature trends (increasing FeF_3^- stability at lower temperature) are inconsistent with the observations on other divalent transition metal complexes (e.g., Testemale et al., 2009a; Liu et al., 2011), and (3) their results were not reproduced by the more recent study of Solomon et al. (1983). Therefore, in the present study, Fe(II)F^+ is the only stable Fe(II) fluoride complexes considered.

In summary, for FeF^{2+}, FeF_2^+, FeF_3(aq) and FeF_4^-, we use the calculated log$K$ (at I = 0) at 25 °C based on Soli and Byrne (1996) for our extrapolation to elevated temperatures. For Fe(II)F^+, we use the HKF model of Sverjensky et al. (1997) for our calculations.

3.2. Extrapolation of thermodynamic properties for Fe(III)-F complexes to elevated temperature

There are no thermodynamic data for Fe(III)F_2^+, Fe(III)F_3(aq) and Fe(III)F_4^- at elevated temperatures. We used the one-term extrapolation method (Gu et al., 1994) to predict the dissociation constants of these Fe(III)-F complexes at elevated temperature. Gu et al. (1994) observed that the change in free energy of a well-balanced isocoulombic reaction is nearly independent of temperature, hence the temperature dependence of the free Gibbs energy of an unknown complex can be derived by comparison with a related complex of similar charge. In this case, we selected the Fe(III)-chloride complexes (Liu et al., 2006), and the isocoulombic reaction is:

$$FeF_n^{3-n} + nCl^- = FeCl_n^{3-n} + nF^- \quad (pK_{ic}) \tag{4}$$

The properties for the dissociation of the Fe(III) fluoride complexes (Reaction (5)) can then be derived from the known dissociation constants for chloride complexes (Reaction (6)) via Eq. (7):

$$FeF_n^{3-n} = Fe^{3+} + nF^- \quad (pK_{dissF}) \tag{5}$$

$$FeCl_n^{3-n} = Fe^{3+} + nCl^- \quad (pK_{dissCl}) \tag{6}$$

$$pK_{diffF} = pK_{ic} + pK_{dissCl} \tag{7}$$

Details of the extrapolation are described in Appendix 1.

We used the MRB formalism to add higher order Fe(III) fluoride complexes in HCh. The MRB parameters for FeF^{2+}, FeF_3(aq) and FeF_4^- optimized by the present study are listed in Table 4 and the extrapolated log$K$s are shown in Table 5.

Table 4
MRB parameters of Fe(III)-F species optimized in the present study.

Species	pK(298 K)	A(zz/a)	B(zz/a)
FeF_2^+	11.003	6.462	−1828
FeF_3 (aq)	14.254	1.696	0
FeF_4^-	16.185	1.451	0

Table 5
Comparison of equilibrium constants for the formation of selected Fe(II/III)-F and Fe(II/III)-Cl aqueous complexes at 25–450 °C, 1.0 kb.

Species	25 °C	50 °C	100 °C	150 °C	200 °C	250 °C	300 °C	350 °C	400 °C	450 °C
$Fe(II)Cl^{+}$ [a]	−0.23	−0.16	0.1	0.45	0.86	1.32	1.81	2.34	2.91	3.53
$Fe(II)F^{+}$ [a]	1.35	1.40	1.61	1.9	2.25	2.65	3.09	3.57	4.09	4.66
$Fe(III)Cl^{2+}$ [b]	1.58	1.91	2.54	3.16	3.76	4.37	4.98	5.60	6.20	6.80
$Fe(III)F^{2+}$ [a]	6.03	6.38	7.07	7.74	8.40	9.07	9.74	10.41	11.05	11.64
$Fe(III)Cl_2^{+}$	2.17	2.13	3.24	5.19	7.58	10.21	13.03	16.04	19.33	23.09
$Fe(III)F_2^{+}$	10.89	10.19	9.99	10.78	12.17	13.98	16.16	18.76	21.87	25.67
$Fe(III)F_3(aq)$	13.69	13.24	12.69	12.44	12.40	12.53	12.83	13.31	14.01	14.99
$Fe(III)F_4^{-}$	15.70	15.00	14.04	13.45	13.12	12.99	13.05	13.29	13.75	14.47

[a] Data from Sverjensky et al. (1997).
[b] Data from Tagirov et al. (2000), as recommended by Liu et al. (2006).

3.3. In-situ XAS study of Fe(II/III) in F-bearing fluids

3.3.1. XANES analyses

XANES spectra reflect the oxidation state and local structure (coordination number, geometry, nature of ligand) of the absorbing atom (Bunker, 2010). The position (energy) of the "white line", historically defined as the most intense peak in the XANES spectrum, generally shifts as a function of the formal oxidation state of the absorbing atom; however, it can also shift as a function of the ligand and/or structure (Bunker, 2010; Tromp et al., 2007). Therefore, XANES is an effective tool to understand the oxidation state of Fe and the structure of the Fe (II/III) species in F-bearing fluids (Brugger et al., 2016).

In this case, it is difficult to deconvolute the effects due to ligand, geometry and oxidation state of the Fe(II/III)-F/Cl/Br complexes by observing the normalized XANES spectra (Fig. 2A), and the first derivative of the XANES spectra was found to better differentiate between these (Figs. 2B and 3).

Fig. 2B shows the evolution of the first derivative of the XANES of four acidic solutions as a function of temperature. We first compare Sols 7 ($FeCl_3$ in 0.01 m HBr) and 9 (FeF_3 in 0.01 m $HClO_4$) to illustrate the main features from the measurements. In both solutions, Fe(III) existed in octahedral coordination in the initial solution. This Fe(III) complex was reduced to an octahedral Fe(II) complex around 200 °C, which in turn transformed into a tetrahedral Fe(II) complex around 400 °C. The octahedral (6-coordinate) to tetrahedral-like (4-coordinate) transition with elevated temperature or salt content is a well-established feature

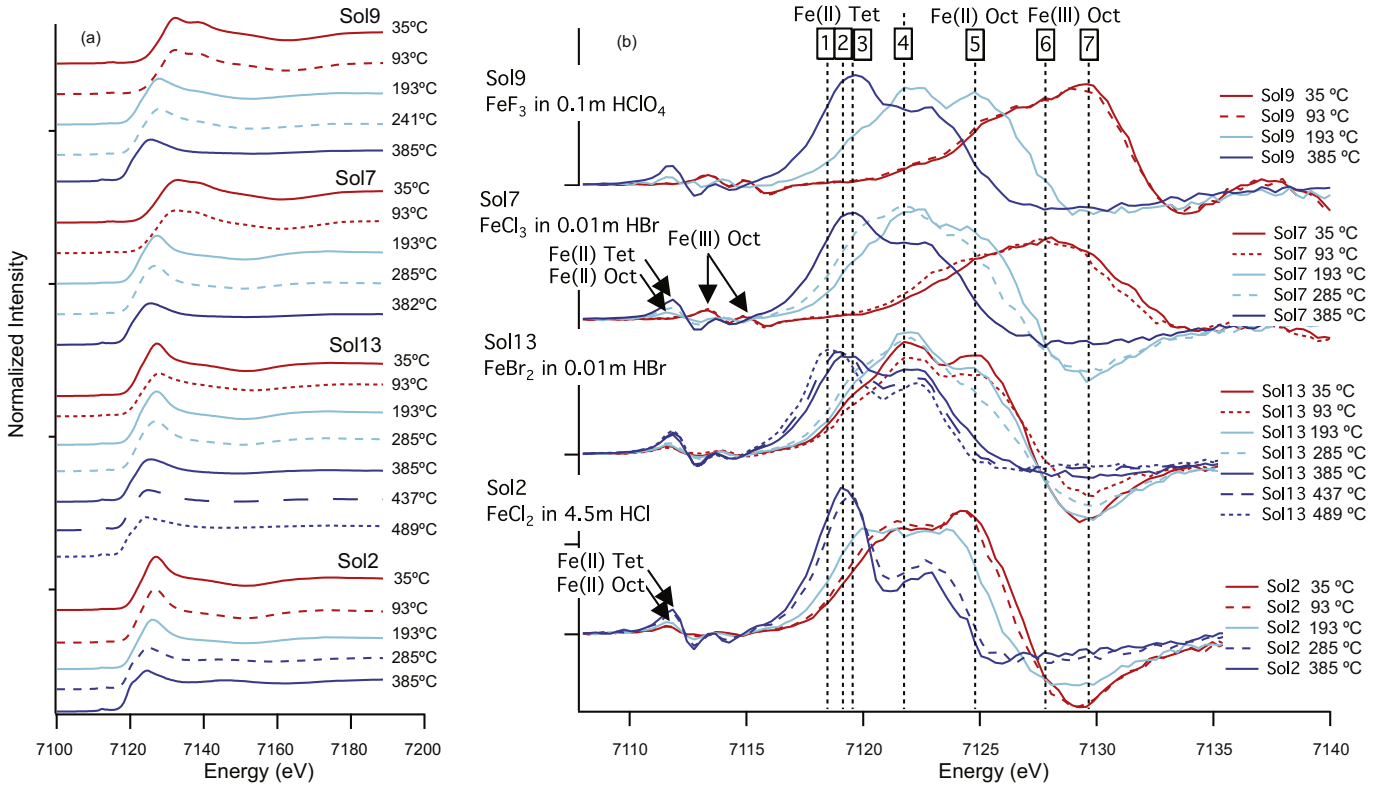

Fig. 2. XANES spectra for solutions 2 ($FeCl_2$ in 4.5 m NaCl), 7 ($FeCl_3$ in 0.01 m HBr), 9 (FeF_3 in 0.1 m $HClO_4$) and 13 ($FeBr_2$ in 0.01 m HBr). (a) Normalized XANES spectra. (b) The first derivative of the XANES. The first derivative of the principal peak position shifts as a function of oxidation state (Fe(II) = line5 and Fe (III) = lines6 and 7; all in octahedral geometry), geometry (octahedral vs. tetrahedral: see lines 5–7 vs 1–3) and ligand (F + O in octahedral geometry = line7, only O in octahedral geometry = line6, predominantly Cl in tetrahedral geometry = line2, predominantly Br in tetrahedral geometry = line1). Line5 indicates a predominantly 5-fold coordination, which occurs when transitioning between octahedral and tetrahedral geometries. The effect of salt concentration (comparing Sols 2 and 7) can be seen in that the 385 °C peak is higher for the saltier solution. Spectra for Sol14 show typical features of Fe(II) octahedral structures at 35 °C and 93 °C. It should be noted however, that no single "feature" has only one peak – e.g., Sol2 and Sol13 at 385 °C are predominated by Cl and Br ligands, however there is a second, smaller peak around line4. It does not make sense to look down line4 and assume that all the peaks there suggest the presence of some intermediate geometry.

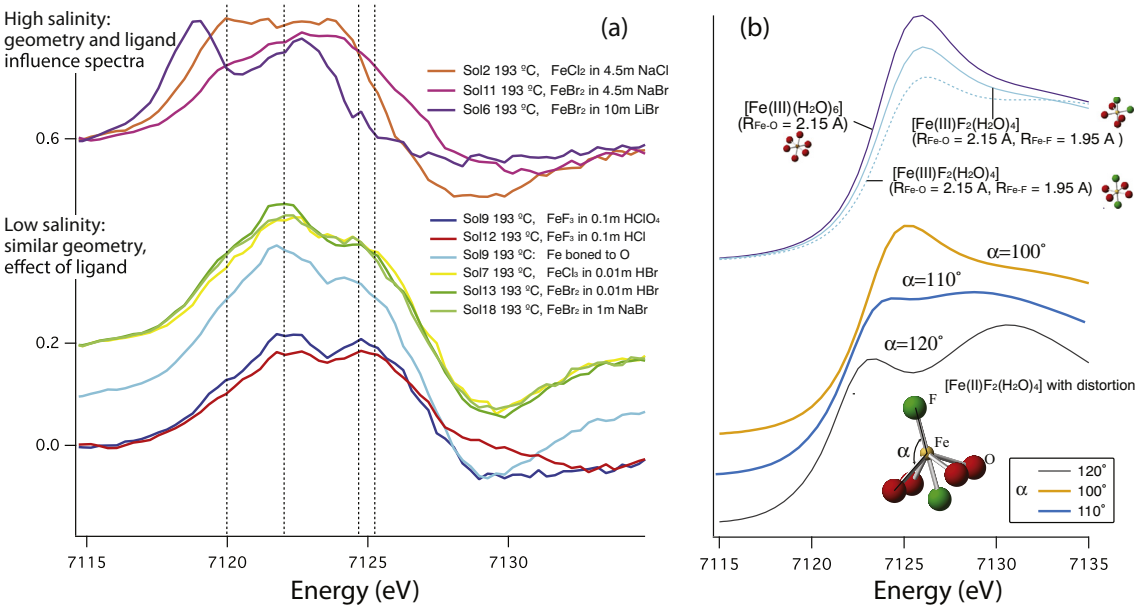

Fig. 3. (a) First derivative of XANES spectra for all solutions at 193 °C. Comparing low and high salinity solutions to determine the effects of ligand and geometry. Low salinity solutions have a similar geometry; thus, the variation is predominantly an effect of the ligand. At high salinity, the ligand affects the geometry in a more pronounced manner – e.g., the transition from octahedral to tetrahedral occurs at a higher temperature for Br compared to Cl. (b) Convoluted calculation of XANES spectra for octahedral Fe complexes. The simulation on $Fe(III)(H_2O)_6$ shows a single white line; with F replacing O, the spectrum changes and a second peak appears in $[Fe(III)F_2(H_2O)_4]$. Calculations also show that distortion of the $[Fe(III)_2(H_2O)_4]$ causes obvious changes on the white line region. The experiment results can be explained when 4 waters are at an angle of 110° rather than 120°.

of the hydrothermal geochemistry of divalent and trivalent first row transition metals (Brugger et al., 2016; Liu et al., 2011). The other prominent feature of the XAS data is the reduction of Fe(III) to Fe(II) with increasing temperature. Such a reduction of Fe(III) aqueous complexes has been observed previously by Testemale et al. (2016). As reviewed in Brugger et al. (2016), the ionizing X-ray beam can have complex effects on the oxidation state of transition metals in aqueous solutions under hydrothermal conditions. In this case, the evidence suggests that similarly to Cu(II/I) (Brugger et al., 2007; Fulton et al., 2000), the reduction of Fe(III) reflects the lower thermodynamic stability of Fe(III) at higher temperature, the transformation being kinetically favoured by beam-induced radiolytic species such as H^+, H, OH, OH^- and hydrated electron, e^-_{aq} (Jayanetti et al., 2001; Saffré et al., 2011).

We illustrate the effects of the ligands, in this case chloride versus bromide, by comparing the XANES spectra of Sols 2 and 13 at 35–400 °C (Fig. 2B). At 400 °C, both solutions contain tetrahedrally coordinated Fe(II), however Sol 2 has predominantly Cl ligands whereas Sol 13 has mainly Br ligands. The first derivative of the XANES spectrum is shifted to lower energy for Sol 2 ($FeCl_2$ in 4.5 m HCl) compared to Sol 13 ($FeBr_2$ in 0.01 m HBr). At 35 °C, Fe(II) is octahedrally coordinated in both solutions, and due to the difference of the predominant ligand (Br^- vs. Cl^-), the main peak is also shifted to lower energy for Sol 2. The effect of salt concentration can be seen by comparing Sols 2 and 7 ($FeCl_3$ in 0.01 m HBr) at 400 °C. Both solutions contain Fe(II) tetrahedrally coordinated to predominantly Cl (Sol 2) and a mixture of Cl + O (Sol 7); the principal peak in the first derivative is higher, sharper and shifted to a lower energy for Sol 2 (labelled 3 in Fig. 2B) compared to Sol 7 (labelled 2 in Fig. 2B).

The aim of this experiment was to assess qualitatively the extent and nature of Fe(II/III)-F complexing. The effects of fluoride can be clearly recognized by comparing Sols 7 and 9 at low temperatures (Fig. 2B). The principal peak of the first derivative for Sol 9 (FeF_3 in 0.1 m $HClO_4$) is sharper and is shifted to higher energy compared with Sol 7 ($FeCl_3$ in 0.01 m HBr) (Fig. 2B, lines 6 and 7). Under these conditions, thermodynamic calculations (Fig. 4) suggest that Sol 9 contains Fe(III) octahedrally coordinated to F and O, whereas Sol 7 contains Fe(III) octahedrally coordinated to only O. By comparing Sols 7 and 9 in Fig. 2B (lines 6 and 7), it is possible to see that there is Fe(III)-F complexing at 35 and 100 °C. The differences in the first derivative that distinguish fluoride complexes reflect a splitting of the 'white line' into two bands. XANES simulations (Fig. 3B) show that an octahedral Fe complex, even with a slight distortion, displays only one band for the white line (e.g., Testemale et al. (2009a) for Fe(II) chlorocomplexes). However, in the case of Fe(III), the white line consists of two bands (e.g., Liu et al., 2006). Calculations based on the $[Fe(III)F_2(H_2O)_4]$ moiety found in the crystal structure of β-$FeF_3.3H_2O$(s) (Teufer, 1964), shown in Fig. 3B, reveal that this duplication results from a strong distortion in the geometry of the complex. In this structure, the two fluoride ions form a linear moiety, and the four oxygens occur in a plane (Fig. 3B). The F-Fe-O angle is about 120° in $FeF_3.3H_2O$(s), resulting in a prominent splitting of the white line (octahedral would have an angle of 90°). An angle of ~110° reproduces the splitting observed in the solution. Such distortions are consistent with the large electronegativity and small ionic radius of F^- in comparison to Cl^-, differences which are expected to significantly affect the distortion of the Fe(III/II) complexes.

There is also Fe(II)-F complexing at 200 °C; this can be seen more clearly on Fig. 3A, a magnified section of Fig. 2B showing the first derivative of the XANES spectrum of all the measured solutions at 200 °C. For the low salinity solutions, where the geometry is similar, the effects due to F as opposed to Cl, Br or O can be clearly seen: both Sols 9 and 12 have two peaks close together, with both peaks having a similar intensity. Sols 7, 13 and 18, which do not contain F, also have two peaks, but with the peak located at lower energy being higher than the second peak. It is interesting to see that when Sol 9 was cooled back to 200 °C (following heating to 400 °C), its spectrum resembled that of Sols 7, 13 and 18, implying that there was no longer any Fe-F complexing in this solution; this reflects the fact that perchlorate breaks down at 200 °C, and shows that for Fe(II), chloride complexing is relatively stronger compared to fluoride complexing. The high salinity solutions are included merely to emphasise that the salt concentration has an

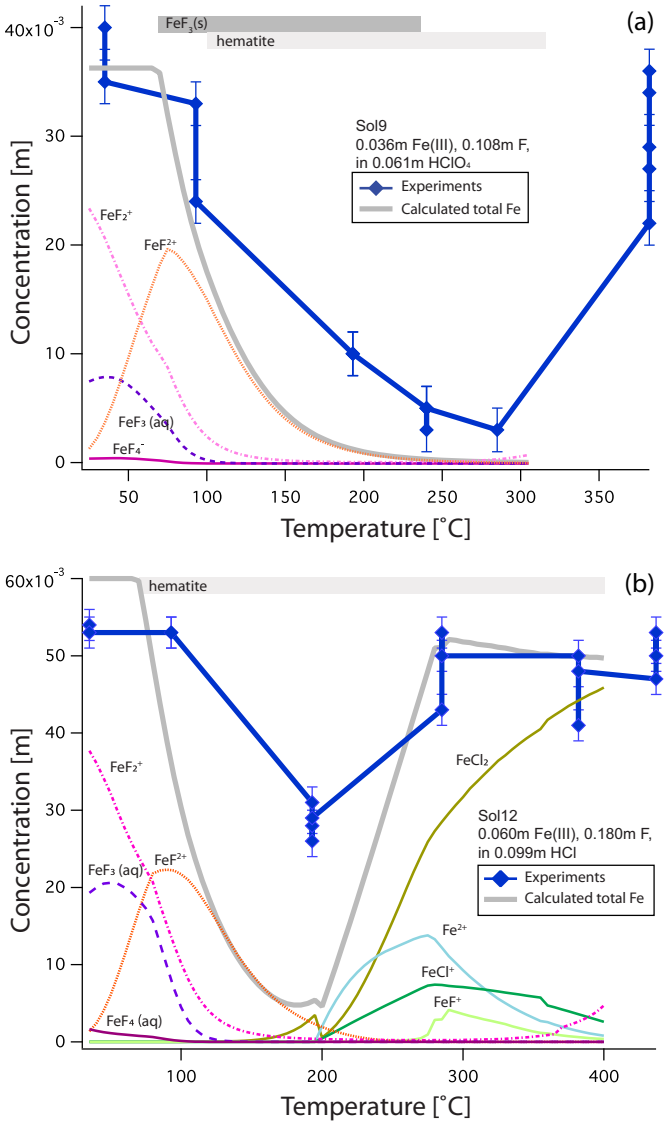

Fig. 4. Concentration of dissolved Fe calculated from XANES spectra and thermodynamic calculations on Fe concentration and speciation for (a) Sol9; (b) Sol12 (Table 1). The calculated Fe speciation is also plotted as thin coloured lines. (For interpretation of the references to colour in this figure legend, the reader is referred to the web version of this article.)

effect on the spectra, as it affects the temperature at which the octahedral to tetrahedral transition occurs. For the solution with FeF_2(s) as the starting salt (Sol 14), the spectrum showed the feature of typical Fe (II) octahedral structure at 35 °C and 100 °C (Fig. 3).

3.3.2. Solubility trend with increasing temperature

We plotted the calculated Fe concentrations with temperature calculated from the XANES step heights for solutions 9 and 12 in Fig. 4. For Sol 9 (FeF_3 in 0.1 m $HClO_4$ solution), the Fe concentrations are high when T is below 100 °C. Above 100 °C, the Fe concentration decreases quickly and reaches its lowest level at 250–300 °C. The Fe solubility increases again above 300 °C. This solution illustrates well the challenges of studying Fe speciation. According to the XANES spectra, Fe (III) is the main oxidation state of aqueous Fe up to 100 °C, but from 200 °C Fe(II) is the main Fe oxidation state (Table 6). The solubility trend observed to 200 °C is well explained by equilibrium thermodynamics assuming that Fe(III)-F complexes (FeF_x^{3-x}, x = 1,2,3) are the predominant forms of Fe in solution. The steep increase in Fe solubility above 300 °C is attributed to the breakdown of perchlorate

Table 6
Results of fitting ESRF EXAFS data and reference for $Fe(III)Cl_3$ and $Fe(III)F_3$ structure.

T (°C)	Main Fe oxidation state	Ligand	N[d]	R(Å)	σ^2(Å^2)	R-range
Sol 9, FeF_3 in 0.1 m $HClO_4$						
35	Fe(III)	F	4.2(5)	1.94(2)	0.004(3)	0–6
		O	1.8(4)	2.15(5)	0.004(3)	0–6
93	Fe(III)	F	3.5(8)	1.91(3)		0–6
		O	2.4(8)	2.13(4)		0–6
193	Fe(II)	F	1.4(1.0)	1.93(7)	0.001(7)	0–6
		O	3.5(1.0)	2.13(4)	0.001(7)	0–6
385	Fe(II)	Cl	1.5(3)	2.24(2)		0–6
		O	2.7(3)	2.12(2)		0–6
285	Fe(II)	O	4.0(9)	2.16(3)		0–6
193	Fe(II)	O	5.9(1.6)	2.10(4)		0–6
93	Fe(II)	O	5.4(1.1)	2.17(3)		0–6
Sol 12, FeF_3 in 0.1 m HCl						
35	Fe(III)	F	4.2(9)	1.94(2)		0–6
		O	1.8(9)	2.14(5)		0–6
93	Fe(III)	F	4.0(1.0)	1.94(3)		0–6
		O	2.0(1.0)	2.15(5)		0–6
193	Fe(III) + Fe(II)	F	1.3(7)	1.94(6)		0–6
		O	2.9(8)	2.15(4)		0–6
285	Fe(II)	O	4.4(8)	2.13(2)		0–6
385	Fe(II)	Cl	1.4(2)	2.22(2)		0–6
		O	2.6(3)	2.14(2)		0–6
437	Fe(II)	Cl	2.1(2)	2.22(1)		0–6
		O	2.1(2)	2.16(2)		0–6
$FeCl_3$ in H_2O[a]						
25		Cl	0.22(26)	2.26(6)	0.0002(1)	
		O	5.78(26)	2.00(1)	0.0036 (10)	
FeF_3 in solids[b]						
25		F	4	1.926		
Sol9, simulated[c]						
25		F	3.05			

[a] Liu et al., 2006.
[b] Teufer, 1964.
[c] Simulated using the thermodynamic properties in Soli and Byrne (1996).
[d] Determined from the XANES spectrum. Numbers in parentheses are 1-σ errors.

(ClO_4^-; Henderson et al., 1971), releasing chloride ions, and hence leading to the formation of Fe(II)-Cl complexes. Therefore, the solubility trends observed are a complex interplay between equilibrium and kinetics, both thermodynamically and beam-induced.

For Sol 12 (FeF_3 in 0.1 m HCl solution), Fe solubility was high below 100 °C, in agreement with thermodynamic calculations (Fe solubility controlled by hematite); FeF^{2+}, FeF_2^+ and FeF_3(aq) are predicted to be the most important Fe(II) complexes in these Cl-bearing solutions. Solubility starts to decrease from 100 °C and reaches its lowest level around 200 °C; above 200 °C, the Fe(II) chloride complexes (e.g., $FeCl_2$(aq)) become important and predominate in the solution at 300 °C, causing an increase of total Fe concentration. Beyond 300 °C the Fe solubility was unstable, but seems to reach the initial values at 400 °C.

3.3.3. EXAFS results and comparison with thermodynamic model

The EXAFS spectra were analysed to determine the coordination geometry of Fe-F/Cl/Br complexes. Note that even if the solutions are not in thermodynamic equilibrium with respect to solubility, ligand exchange reactions are fast for the halide complexes of interest (*ps* to *μs*), so that the speciation in the aqueous phase will be at steady state. The results of the fitting of the EXAFS spectra are shown in Table 6 and Fig. 5. Because of the similarity in the scattering factors of O and F, there are relatively large errors on the O/F ratios in the Fe complexes studied here. To guide the discussion, we compare the results of EXAFS fits with the prediction of the thermodynamic model. The aim of this

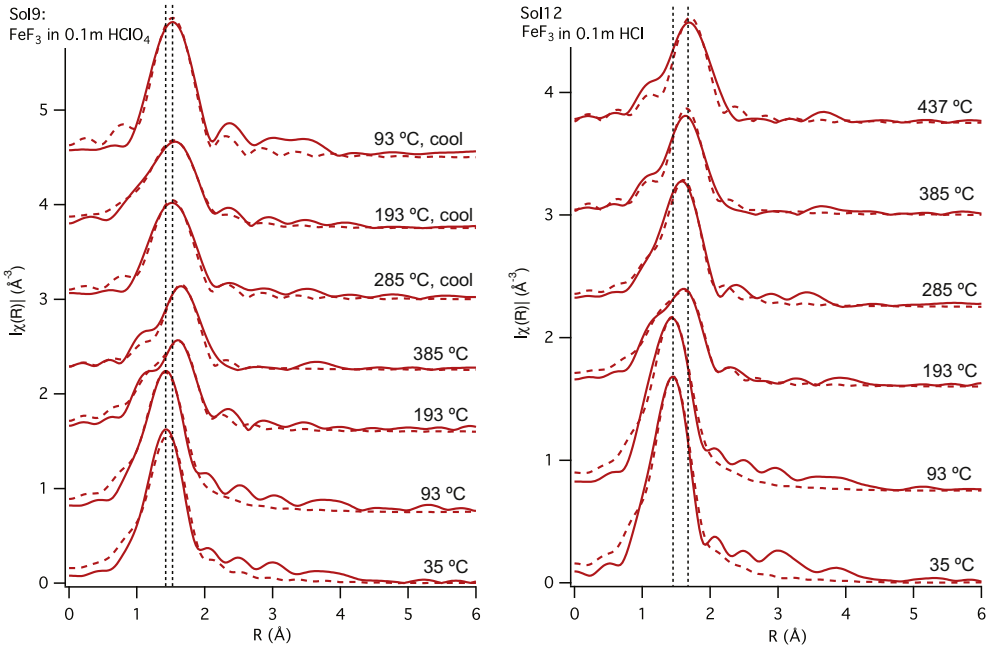

Fig. 5. Fourier transform of EXAFS spectra (not phase corrected, solid line) with fits (dashed line) for Sol9 and Sol12.

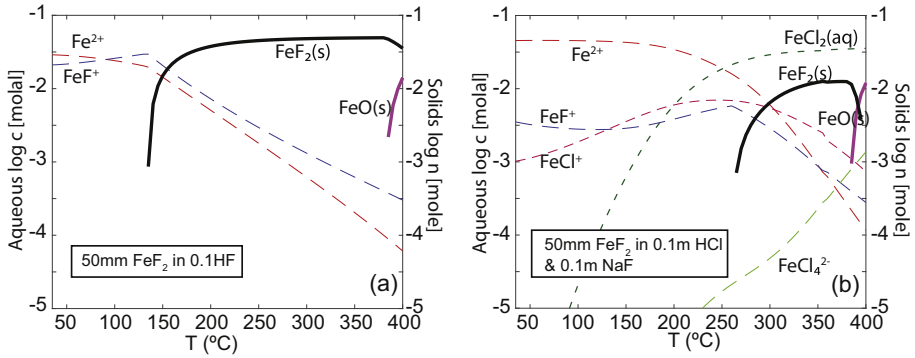

Fig. 6. Thermodynamic calculations on speciation and solubility of Fe(II) complexes as a function of temperature. (a) 50 mm FeF_2(s) in 0.1 m HF, 35–400 °C, 600 bar; (b) 50 mm FeF_2(s) in 0.1 m HCl and 0.1 m NaF, 35–400 °C, 600 bar. Minerals are shown in bold.

study is to provide a qualitative check of the predictions from the thermodynamic model. We calculated the solubility of Fe minerals and Fe speciation in experimental solutions at 25–400 °C, 600 bar according to Table 1, and the results are shown in Figs. 4 and 6.

For Fe(III), it is predicted that $Fe(III)F^{2+}$, $Fe(III)F_2^{+}$ and FeF_3(aq) are the predominant species in the F-bearing solution (Fig. 4A), even in the presence of 0.1 m HCl (Fig. 4B). At 35 °C, the predominant F complexes are predicted to be $Fe(III)F_2^{+}$ and FeF_3 (aq), and at 100 °C the predominant complexes are predicted to be $Fe(III)F^{2+}$ and $Fe(III)F_2^{+}$. The decrease in number of fluoride ligands is attributed mainly to the decrease in the activity of the F^- ion with increasing temperature due to the increase in the association constant of HF(aq). The results of the EXAFS fits are consistent with an octahedral Fe(III) complex containing an average of 3 to 4 fluoride ions in solutions 9 and 12 at 35 and 100 °C (Table 6), suggesting that fluoride complexing may be slightly stronger than expected in Fe(III) solutions.

At 200 °C, Fe(III) is fully (Sol 9) or partially (Sol 12) reduced to Fe (II) (Table 6). This is accompanied by a reduction of the number of F^- ligands in the complexes decreased to ~1, indicating predominance of the $Fe(II)F(H_2O)_5^{+}$ complex (Fig. 4). Above 200 °C, the EXAFS refinement shows increased Fe-Cl interaction in both Sol9 and Sol12 solutions (Table 6, Fig. 5). In particular, at highest temperature of 437 °C, Fe is bonded with 2.1 Cl and 2.1 O atoms, indicating tetrahedral $FeCl_2$(aq) species.

3.4. Solubility and speciation of Fe in fluoride solutions – a summary

In summary, our new XAS data show that in both Fe(II) and Fe(III) systems, Fe fluoride complexes are only important at low temperatures (< 150 °C). With increasing temperature (35–200 °C), Fe solubility decreases in fluoride-only systems. In Cl-bearing systems Fe solubility increases when chloride is available at high temperatures (> 200 °C) in the solutions. From the XANES data, it was evident that fluorine was no longer bonded to Fe(II) above 200 °C (Fig. 2). The EXAFS results reveal a decrease of coordination number of F in the Fe(III)-F complexes with increasing temperature (Table 6), which may be the reason for the decrease in Fe solubility.

Fe(II) fluoride complexes are more stable than Fe(II) chloride complexes at T < 150 °C (Fig. 6B). Fe(II) chloride complexes (e.g., $FeCl_2$(aq)) become increasingly stable at higher temperature and dominate the solution from 200 °C and above when both F and Cl are present, causing the retrograde Fe solubility at temperatures above 200 °C in mixed F-Cl solutions.

The above calculations show that the available data are able to correctly predict the solubility of Fe fluoride minerals in F-bearing solutions of our experiment, which provides us the confidence to model

the role of F in transporting Fe in geological hydrothermal systems.

4. Thermodynamic modelling of fluid-granite interaction

Extensive hydrothermal alteration has been recognized across the Olympic Dam breccia complexes (ODBC) and RDG (Ehrig et al., 2012). It is generally thought that the majority of mineralization in ODBC was produced by two main hydrothermal events: (1) a high temperature, high salinity magnetite stage (> 400 °C, 20–45 wt% NaCl equivalent), and (2) a low temperature, low salinity hematite stage (150–300 °C, < 10 wt% NaCl equivalent) (Bastrakov et al., 2007; Oreskes and Einaudi, 1992). The current mineralization also reflects a long history of fluid-flow resulting in (at least) small-scale element mobility (e.g., Kirchenbaur et al., 2016). Based on the thermodynamic data summarized in Appendix 1, we modelled the mobility of REE, U, Fe and F in hydrothermal fluids circulating in a typical granitic rock. The results are shown in the following sections.

4.1. Fluorine concentration and speciation

Our calculations show that F concentrations increase with increasing temperature and reach a maximum value of around 70 ppm at around 450 °C. Higher salinity favours F dissolution at 50–350 °C (Fig. 7A) but this effect becomes less significant above 400 °C. The Cl/F ratio reflects the relative importance of Cl and F in the fluids, and calculations show that it increases with increasing c[Cl] and decreasing temperature (Fig. 7C).

The aqueous speciation of F is mainly controlled by temperature. Fluoride ion (F^-) is the predominant species at $T < 200$ °C while CaF^+ dominates the solution at 200–300 °C. Above 350 °C, HF(aq) becomes the predominant species (Fig. 7B). Fig. 7D shows the F-bearing mineral assemblages versus temperature and fluid salinity. Biotite, apatite, fluorite and REE fluorocarbonates (i.e., parasite-Ce and bastnäsite-Ce) buffered F in the fluid. Note that biotite and apatite solid solutions are named after the predominant components in each solid solution in the figures. Fluorite is predicted to disappear from the assemblage at high temperature, especially in high salinity fluids.

4.2. Iron solubility and speciation

Regardless of the presence of F, aqueous Fe concentrations were found to increase with increasing temperature and salinity (Fig. 8A,B). Specifically, Fe concentrations are predicted to be extraordinarily low (< 1 ppm) at c[Cl] < 1 m, and the overall Fe solubility can be up to more than one order of magnitude lower in F-bearing fluids than in F-free fluids at similar conditions, especially at high temperatures (Fig. 8A,B). The differences in Fe solubility are explained by the higher pH of the F-bearing fluids (Fig. 8F) and by the effect of F on the Fe-mineralogy, which affects the redox state of the fluid. The fluid is more reduced for F-bearing fluids, which also contributes to decreased Fe solubility (Fig. 8C,D). The redox of the solution is mainly determined by the Fe^{2+}/Fe^{3+} ratio of the solution. The F-bearing solution is more reduced than the Fe-free solution because F facilitates the precipitation of hematite, which results in the decrease on Fe^{3+} concentration, and

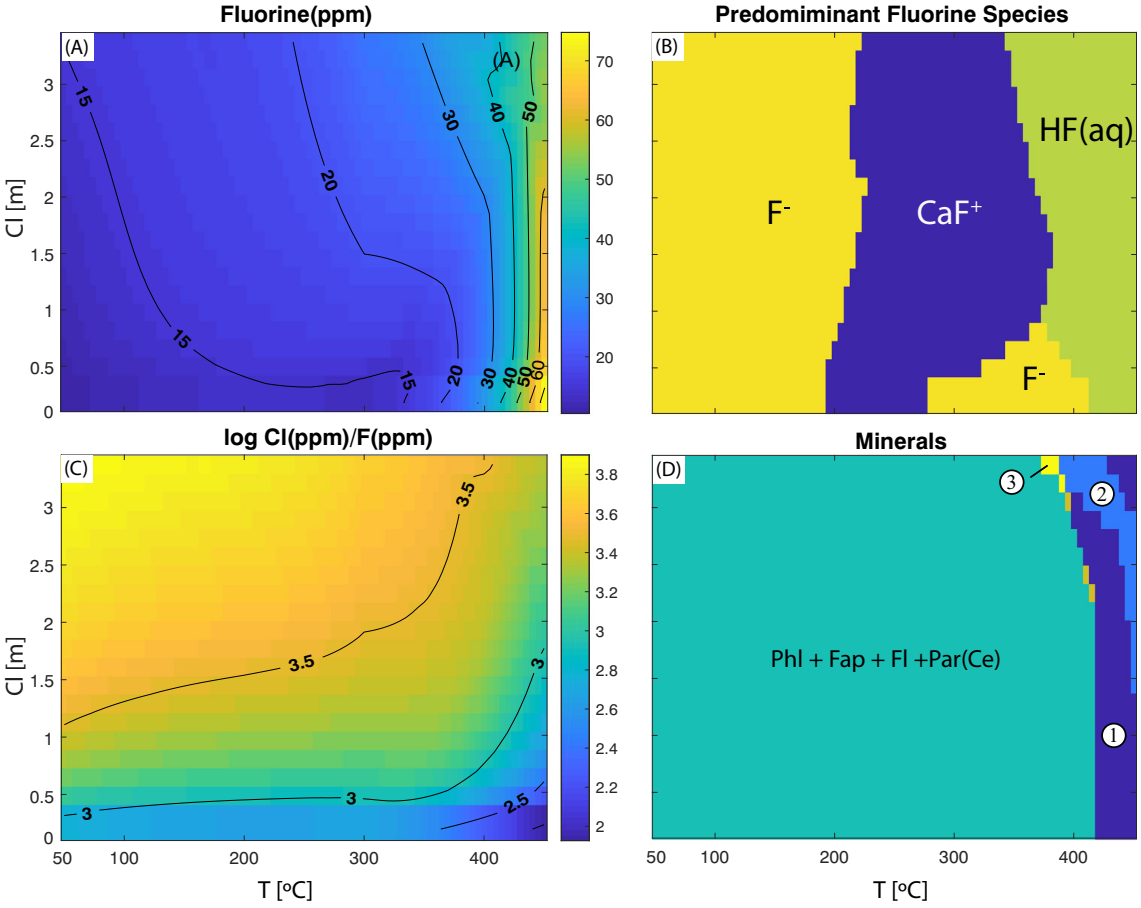

Fig. 7. Fluoride concentration and speciation as a function of salinity(Cl) versus T (°C). (A) Fluorine solubility map; (B) F speciation map; (C) log (Cl/F) ratio map (based on ppm); (D) F-bearing minerals map; field number (1) Phl + Fap + Fl + Bas(Ce); (2) Fphl + Fap + Bas(Ce); (3) Fphl + Fap + Par(Ce). Abbreviations: Phl = phlogopite and Fphl = fluorophlogopite (dominant components in biotite solid solution), Fap = apatite-(CaF) (dominant component in apatite solid solution), Fl = fluorite, Bas(Ce) = bastnäsite-(Ce), Par(Ce) = parisite-(Ce).

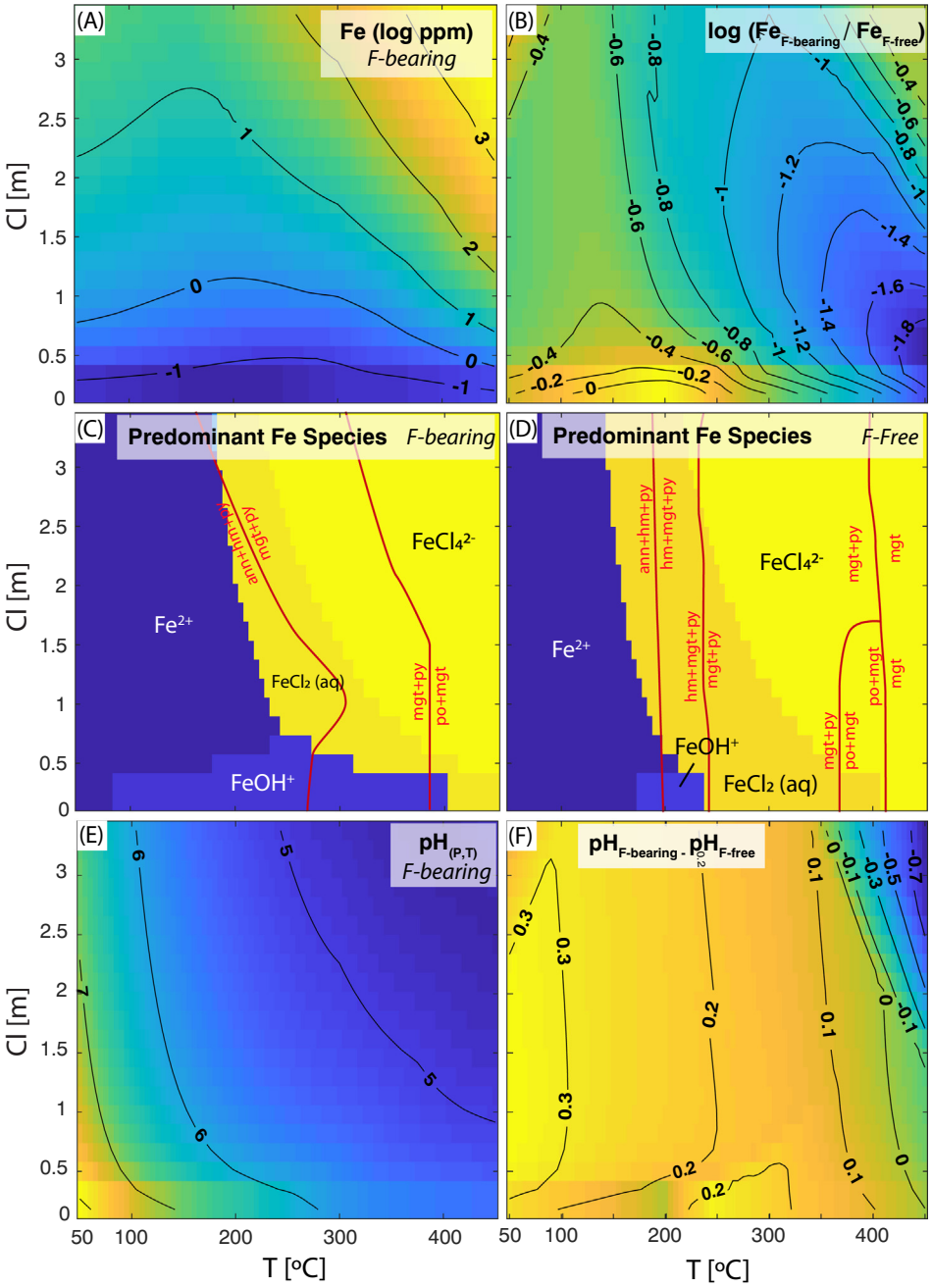

Fig. 8. Calculated Fe concentrations, speciation, and pH as a function of salinity (Cl) versus T (°C), in F-bearing and F-free model granite. (A) Solubility of Fe in F-bearing fluids. (B) Difference (expressed as log of ratio) in Fe-solubility between F-bearing and F-free fluids. (C) Predominant Fe complex in F-bearing and (D) F-free model systems; the minerals controlling Fe solubility are also shown (red lines). (E) pH of F-bearing fluids. (F) pH difference for F-bearing and F-free fluids. Note that the decreased Fe solubility in the F-bearing fluids is caused both by the increased pH and by the change in Fe-mineralogy. Abbreviations: ann = annite, hm = hematite, mgt = magnetite, po = pyrrhotite, py = pyrite. (For interpretation of the references to colour in this figure legend, the reader is referred to the web version of this article.)

higher Fe^{2+}/Fe^{3+} ratios in solution. The increased pH in the F-bearing solution is caused by the formation of HF(aq).

The aqueous speciation of Fe is mainly controlled by temperature while salinity is less important. The predominant Fe species is the Fe^{2+} aqua ion at $T < 200\,°C$. Above 200 °C, Fe chloride complexes, i.e., $FeCl_2$(aq) and $FeCl_4^{2-}$, dominate the solution (Fig. 8C,D) due to their increasing stability at higher temperatures, associated with the higher affinity of tetrahedral complexes for Cl than water (Testemale et al., 2009a; Mei et al., 2015). Note that the predominance of Fe(II) complexes is expected, since recent experimental and theoretical studies indicate that Fe(III) species are not stable at elevated temperatures (Brugger et al., 2016; Liu et al., 2006; Testemale et al., 2009a, b).

4.3. Rare Earth elements solubility and speciation

We included La, Ce and Nd in our simulations, since those are usually the most enriched REEs in IOCG deposits, i.e., the OD, as well as RDG (Ehrig et al., 2012). For discussion, we choose La to represent the REE group for the following reasons: (1) the chemical and thermodynamical properties of all REE are similar and they usually share similar geochemical behaviours; (2) compared to Ce, La has a single oxidation state La(III), whereas Ce can form Ce(III) and Ce(IV).

Our calculations show that both temperature and salinity have strong influence on La solubility in granite-buffered fluids (Fig. 9). The concentrations of La are relatively high over 2 regimes: (1) $T = 180–300\,°C$, c[Cl] < 0.5 m; and (2) $T > 300\,°C$, c[Cl] > 2 m. Comparing F-bearing and F-free systems, the overall concentration of La is enhanced by 0.5 to ~2 orders of magnitude in the F-bearing system relative to the F-free system (Fig. 9A,C).

The aqueous speciation of La is shown in Fig. 9B (F-bearing) and 9D (F-free). Regardless of the presence of F, the predominant La species is $LaCO_3^+$ below 100 °C, and La hydroxyl species dominate the solution at low salinity (c[Cl] < 1 m, 100–400 °C). Note that these predictions have low level of confidence, due to the limited experimental data on

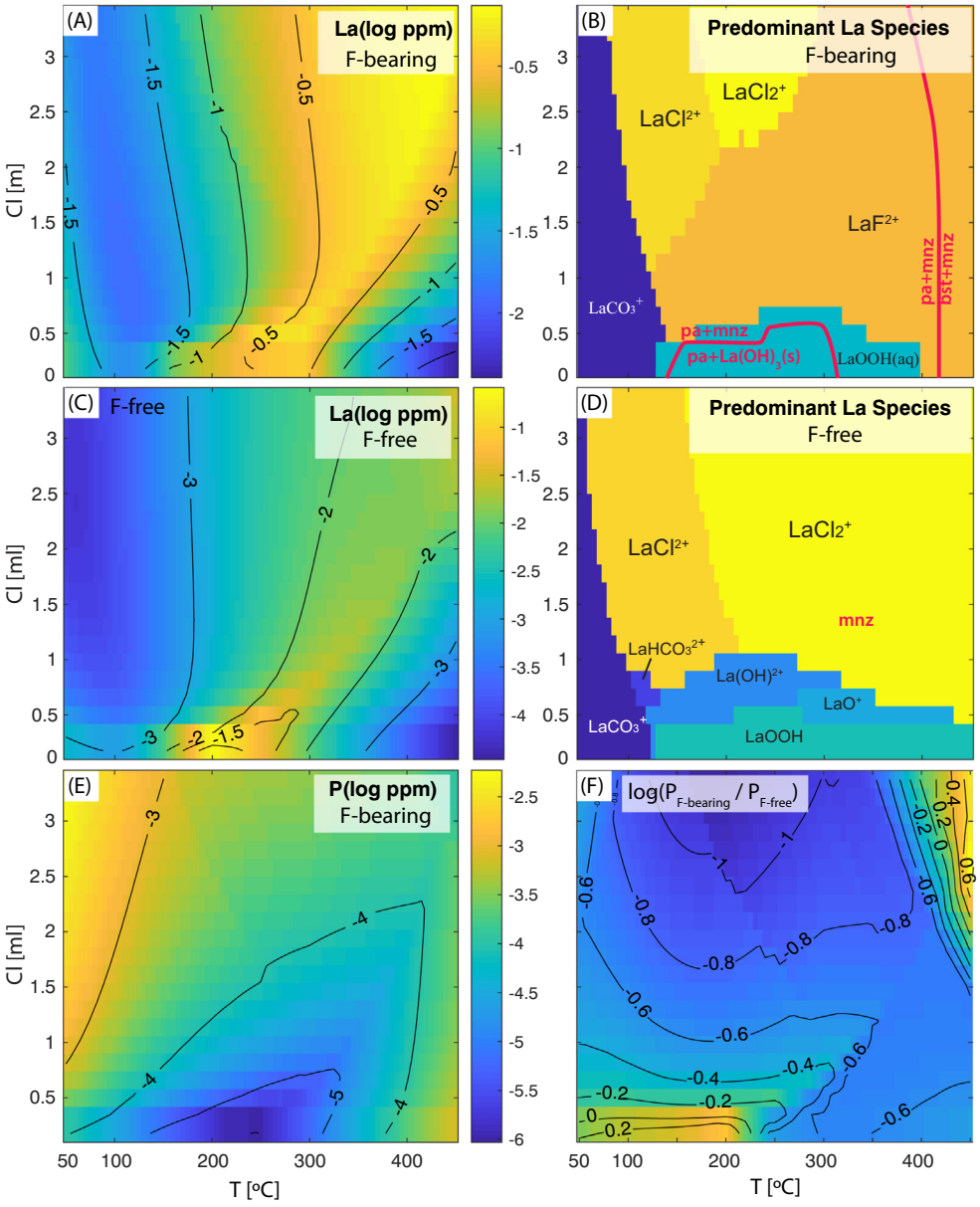

Fig. 9. Calculated La and P concentrations and speciation as a function of salinity(Cl) versus T for F-bearing (A, B and E) and F-free systems (C and D). Solubility-controlling minerals are shown in red, and include $La(OH)_3$(s), monazite-(La) (mnz), parasite-(Ce) ($Ca_2Ce_2LaNd(CO_3)_6F_4$; pa), and bastnäsite-(La) ($Ce_2LaNd(CO_3)_4F_4$; ba); monazite-(La) is the stable phase at all conditions in the F-free simulations. (E) Solubility of P in F-bearing fluids. (F) Difference on P solubility for F-bearing and F-free fluids (as log ratio of ppm concentration). (For interpretation of the references to colour in this figure legend, the reader is referred to the web version of this article.)

REE carbonate and hydroxide complexing (Migdisov et al., 2016). The predictions diverge at higher T and salinity depending on whether F is included in the model. Specifically, in F-bearing fluids, the predominant species are $LaCl^{2+}$ and $LaCl_2{}^{+}$ at 100–200 °C, while above 200 °C (or 100 °C when c[Cl] = 0.5–1.5 m), LaF^{2+} is the predominant species. For the F-free system, La chloride complexes dominate the fluid at T > 100 °C and c[Cl] > 1 m.

Hence, the higher La concentrations in the F-bearing simulations are due in part to the formation of REE fluoride complexes. However, since elevated concentrations are obtained even where La-fluoride complexes are not predicted to be dominant, another process must account for the increased mobility of REE in the F-bearing model. The dissolution of monazite-(La), a widespread predicted mineral in F-bearing (Fig. 9B) and the only one of the minerals in the F-free simulations, can be written as:

$$LaPO_4(s) + F^- + 2H^+ = LaF^{2+} + H_2PO_4^- \quad (8)$$

As shown in Fig. 8E and F, pH is higher in the F-bearing than in the F-poor simulations, resulting in a lowering of REE solubility. However, a lowering of the aqueous phosphate content would cause an increase in REE dissolution. Fig. 9E and F shows that phosphate concentrations are higher by more than an order of magnitude in the F-free simulations. This is the result of the control of phosphate solubility by apatite-(CaOH) in the F-free simulations, and by apatite-(CaF) in the F-bearing simulations, with the latter being less soluble than the former.

4.4. Uranium solubility and speciation

Calculations show that U solubility is mainly controlled by temperature while salinity plays a minor role (Fig. 10A,C). The predicted aqueous U concentrations are highest at T < 200 °C or T > 400 °C in both F-bearing and F-free systems. Uranium solubilities are higher in F-bearing fluids, especially at $T \leq 150$ °C and c[Cl] > 0.5 m (> 10 times more U in the F-bearing fluid). The reasons are complex, but the main control appears to be pH, which affects the HCO_3^- (predominant up to ~110 °C in F-free, and ~150 °C in F-bearing systems) – H_2CO_3(aq) equilibrium. However, the calculated solubility of U is very low (up to 0.1 ppb) in the fluids equilibrated with a normal fresh granite (Fig. 10A,C), which correlates with a relatively reduced mineral assemblage dominated by uraninite + magnetite + pyrite

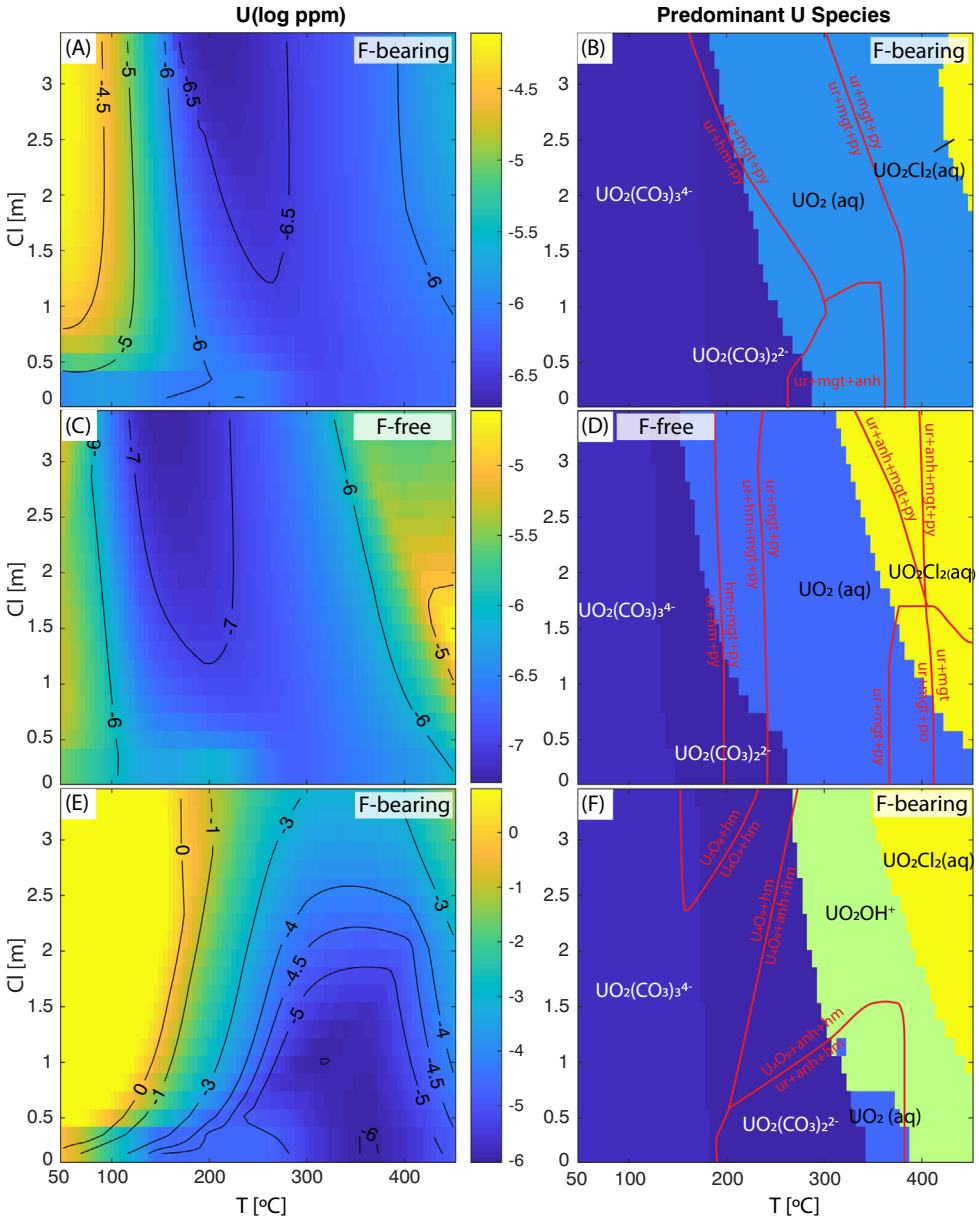

Fig. 10. Uranium solubility (ppm) and speciation T-salinity map for F-bearing (A, B, E, F) and F-free systems (C, D), for 'fresh' and oxidized (All Fe as Fe^{3+}, no reduced S) granite. Uranium concentration and speciation maps in F-bearing system (A and B) and in F-free system (C and D). (E) and (F) show the solubility and speciation of U in fluids after equilibrium interaction with an oxidized granite. Minerals controlling U solubility and redox are plotted in (B), (D) and (F) with boundaries shown as red lines. Abbreviations: anh = anhydrite, bt = biotite, hm = hematite, mt = magnetite, po = pyrrhotite, py = pyrite, ur = uraninite. (For interpretation of the references to colour in this figure legend, the reader is referred to the web version of this article.)

(± anhydrite ± hematite). Under these conditions uraninite (UO_2) is the solubility-limiting U mineral, and the fluid has poor capacity for mobilizing U, even if the recently discovered UCl_4(aq) species (Timofeev et al., 2018) is included in the model.

To explore the effect of the redox state of the granite, we modelled the interaction of an oxidized fluid (with 0.1 wt% SO_4^{2-}) and a weathered (sulfide-free; all Fe as Fe_2O_3) granite. The results show that U solubility is greatly enhanced (≫1 ppb) especially at low-T (< 250 °C), and at high temperature-high salinity (> 400 °C, > 2.5 m Cl) (Fig. 10E,F). The U-limiting phases are mixed uranium oxides (U_3O_8(s) and U_4O_9(s)), rather than stoichiometric uraninite. As expected, oxidized fluids are favourable for U mobilization and the redox state of the fluid is essentially the key factor controlling U solubility (Timofeev et al., 2018). However, there is no significant F complexation in the calculated systems (Fig. 10B,D,F). Instead, U(VI) carbonate species (i.e., U(VI)$O_2(CO_3)_3^{4-}$ and U(VI)$O_2(CO_3)_2^{2-}$) are predominant at T < 200–300 °C, while UO_2Cl_2(aq) dominates at high temperatures (T > 400 °C). Xing et al. (2018) obtained similar results by modelling equilibrium between an oxidized fluid with F-rich granite: U(VI) hydroxyl and chloride species are the predominant species (no carbonate species included in their calculations) responsible for extracting U from granite, while U(IV/VI)-F complexation plays a negligible role.

4.5. Silica solubility and speciation

Temperature is the main control on Si solubility (Fig. 11A,C): Si concentrations increase with increasing temperature. Increasing Cl concentration results in a small salting-out effect, but the addition of F to the model results in higher Si solubility in F-bearing fluids (compare Fig. 11A,C). The predominant aqueous Si species at 50–450 °C in both F-bearing and F-free fluids with a salinity of 10 wt% NaCl equivalent are shown in Fig. 11B and D as a function of temperature. For both fluids, the predominant Si species are H_4SiO_4(aq), $NaHSiO_3$(aq) and $H_3SiO_4^-$ under simulated conditions. Among fluoride complexes, the concentration of $Si(OH)_2F_2$(aq) increases dramatically with temperature, but remains a minor species overall even above 350 °C (Fig. 11B). In particular, the overall concentration of the $NaHSiO_3$(aq) and $H_3SiO_4^-$ species are 1–2 magnitudes higher in F-bearing fluids than in F-free fluids (Fig. 11B). These slightly elevated Si concentrations in F-bearing fluids are related to the higher pH in these fluids, which

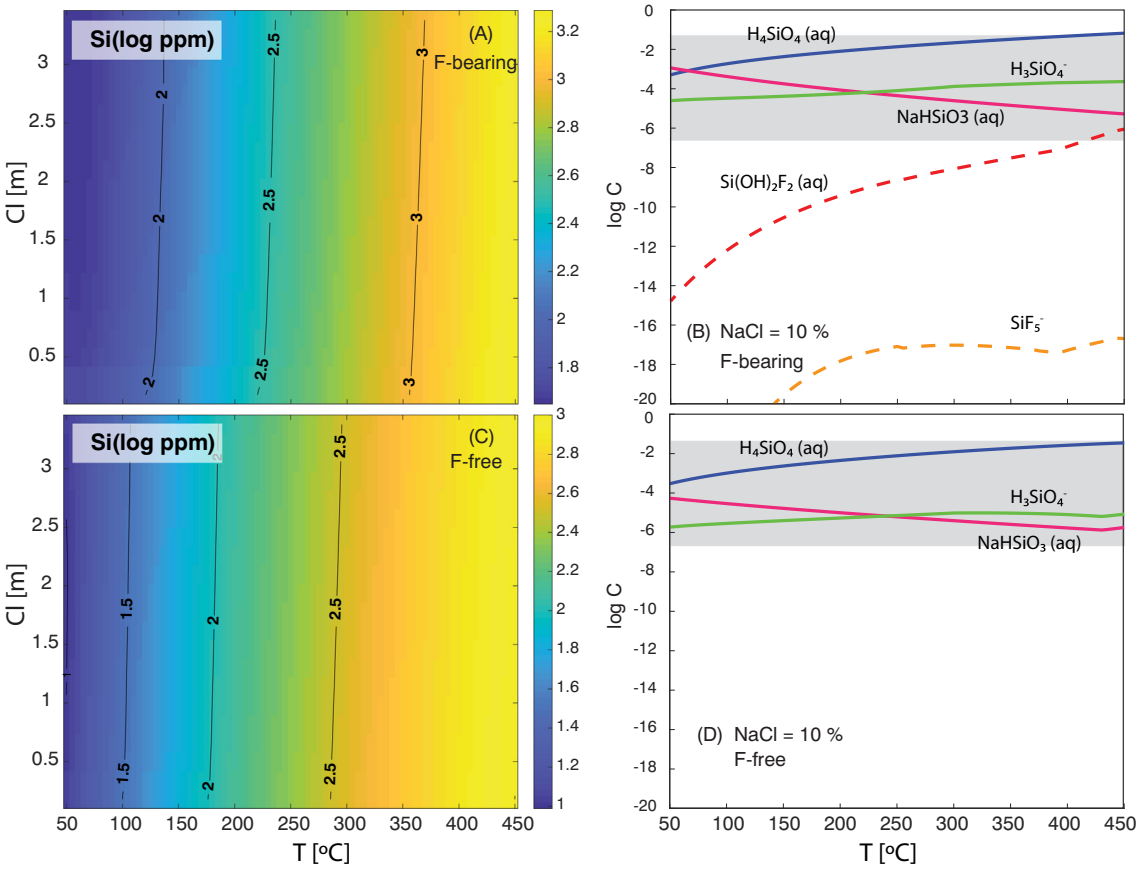

Fig. 11. Si solubility in fluids as a function of salinity (Cl) and temperature (°C) and predominant Si aqueous species in solutions with 10 wt% NaCl. (A) and (C) Si solubility in fluids of F-bearing and F-free systems respectively; (B) and (D) predominant Si aqueous species in fluids with 10 wt% NaCl under F-bearing and F-free systems. Grey area in (B) and (D) show the same concentration range.

increases the concentrations of the $H_3SiO_4^-$ (reaction (9b)) and $NaHSiO_3$(aq) (reaction (9c)) species while leaving H_4SiO_4(aq) unaffected (reaction (9a)):

$$SiO_2(s) + 2H_2O = H_4SiO_4\,(aq) \quad (9a)$$

$$SiO_2(s) + 2H_2O = H_3SiO_4^- + H^+ \quad (9b)$$

$$SiO_2(s) + Na^+ + H_2O = NaHSiO_3\,(aq) + H^+ \quad (9c)$$

5. Discussion

5.1. Fluorine mobility during water-rock interaction in granite

Fluorine is widely distributed in many types of hydrothermal fluids, for instance, sedimentary and basement formation waters, deep sea vent fluids, metamorphic and magmatic fluids (e.g., Banks et al., 1994; James et al., 2014; Seward et al., 2014; Yardley, 2005). Fluorine concentrations in these natural fluids vary over a large range from 20 to 5000 ppm and fluids with higher temperature tend to have higher F content, i.e., magmatic fluids and metamorphic fluids (e.g., Yardley, 2005; Fig. 12). Our simulations show that in the case of equilibrium granite-fluid interaction, the Cl/F ratio similarly increases with increasing temperature over the range of temperature and fluid salinity investigated, i.e., 50–450 °C, 0–3.5 m Cl (0–20 wt% NaCl equivalent) (Fig. 12).

The Cl/F ratio of the calculated fluids is higher compared to the magmatic and metamorphic fluids reported by Banks et al. (1994) and Yardley (2005), which is caused by the lower temperature of our calculated fluids (< 450 °C). Seawater has a higher Cl/F ratio than the values resulting from fluid-granite interaction in our model (Fig. 12;

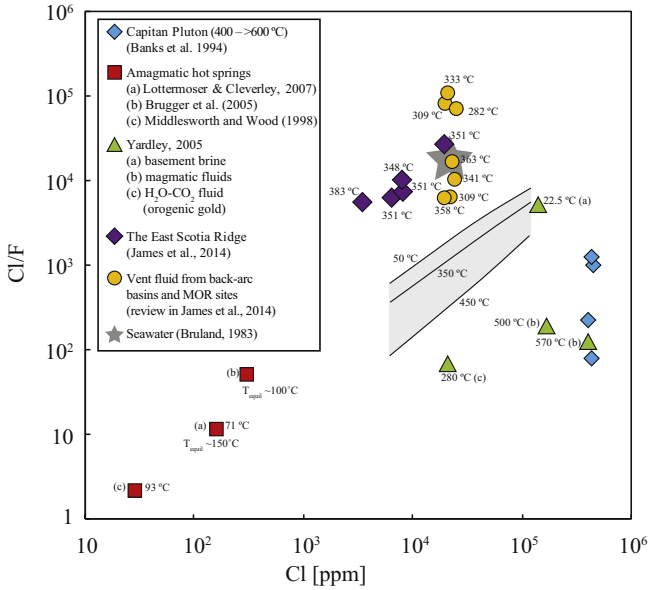

Fig. 12. Cl/F and Cl data for natural F-bearing fluids and the calculated fluids. Grey area shows the calculated fluids in equilibrium with fresh granite at 50–450 °C and salinity at c[Cl] = 0–3.5 m. Solid lines are the calculated isothermal lines. For natural samples, the temperatures of the fluids are shown besides the marker.

Bruland, 1983). In general, seafloor magmatic hydrothermal systems are dominated by seawater, and the Cl/F ratios in these fluids reflect that source (see Fig. 12; review in James et al. (2014)). Variations in F contents are attributed mainly to interaction with host rocks; host rocks with higher acidity (i.e. dacitic rather than basaltic) tend to result in higher F in fluids (James et al., 2014).

Low Cl/F ratios resulting from relatively high F concentrations in Cl-poor waters have been reported for some low-temperature granite-hosted hot springs (Brugger et al., 2005; Lottermoser and Cleverley, 2007; van Middlesworth and Wood, 1998). For Innot Hot Springs, Queensland, fluorite controls F solubility instead of silicates or apatite-(CaF), with F^- and CaF^+ the dominating F species in these fluids (Lottermoser and Cleverley, 2007).

In our simulations, full equilibrium is assumed for the fluid-granite interaction, which is increasingly valid with increasing temperature. The calculated fluids in our modelling present F concentrations over 70 ppm at ~450 °C, with a decreased Cl/F ratio, indicating that F is relatively more enriched in the fluids. Therefore, the modelling shows that the extensive interaction between fluids and F-rich granite could be a good mechanism generating F-bearing fluids, which contributes to the F enrichment in the case of the OD deposits and many other F-rich IOCG systems.

5.2. Fluoride as a transporting or precipitating ligand of Fe?

The F enrichment in many Fe-rich hydrothermal mineralization systems and the ability of F to form strong complexes with Fe suggest that F could contribute to Fe transport in hydrothermal fluids. However, this hypothesis is not supported by our results: both in-situ XAS experiments and thermodynamic studies give consistent results that Fe(II/III)-F complexes become less important in fluids at higher temperatures and the solubility of Fe decreases dramatically above 200 °C when F is the main ligand (Figs. 4 and 6).

We further tested the relative importance of F and Cl on complexing Fe(III) with the activity-activity diagram in Fig. 13A, showing that Fe (III)-F complexes are important at low temperature, whereas Fe(III)-Cl species become increasingly important with increasing temperature. Chloride is usually the predominant ligand in natural hydrothermal fluids and is considered to be the main ligand responsible for Fe transport (Brugger et al., 2016; Liu et al., 2006; Testemale et al., 2009a). Our calculations confirm that Fe forms predominantly chloride complexes above 200 °C regardless of the presence of F (Fig. 8C,D). Therefore, F^- is not a good ligand for the hydrothermal transport of Fe at temperatures > 200 °C.

Table 7
Equilibrium constant for reaction $FeCl_2(aq) + 2\,F^- = FeF_2(s) + 2\,Cl^-$ and Cl/F values at equilibrium at 25–300 °C, Sat.

T [°C]	log*K*	Cl/F
25	4.1217	115
60	4.6758	218
100	5.0521	336
150	5.9202	912
200	6.8014	2516
250	7.8646	8557
300	9.2468	42,015

Instead, F may drive precipitation of Fe. In-situ XAS results show that Fe solubility decreases at elevated T (typically > 200 °C) in F-rich solutions (Fig. 4). In general, Fe solubility is low at high F activity and high temperature. The fluid-granite interaction modelling also shows that the overall solubility of Fe is lower in F-bearing fluids than F-free fluids, as a result of the slightly higher pH of F-bearing fluids and the resulting slight differences in mineral stability and its effect on the redox state of the fluid (Fig. 8).

The effects of F activity and temperature are further illustrated in Fig. 13B. In particular, Fe(II)F_2(s) is predicted to precipitate as a result of increasing temperature and F activity, following:

$$FeCl_n^{2-n} + 2\,F^- = FeF_2(s) + n\,Cl^-, \quad (10)$$

The equilibrium constants (log*K*) of reaction (10) at 25–300 °C are listed in Table 7. We also calculated the Cl/F ratio at equilibrium with the assumption that $FeCl_2$(aq) is the predominant Fe species in fluids and a_{FeCl_2} equal to 1 (Table 7). The Cl/F ratio is 2516 at 200 °C, and increases with increasing temperature, reaching 42,015 at 300 °C. According to our simulation of fluid-granite equilibrium, the Cl/F ratio of the fluid is especially low at low salinity (Cl/F < ~1200, c[Cl] < 0.5 m; Figs. 7C, 12); this corresponds to a regime of very low Fe solubility in the fluid (Fig. 8A). Iron solubility is also predicted to be significantly lower in F-bearing fluids compared to F-free fluids at T > 350 °C and c[Cl] < 1.5 m (Fig. 8B), which corresponds to a low

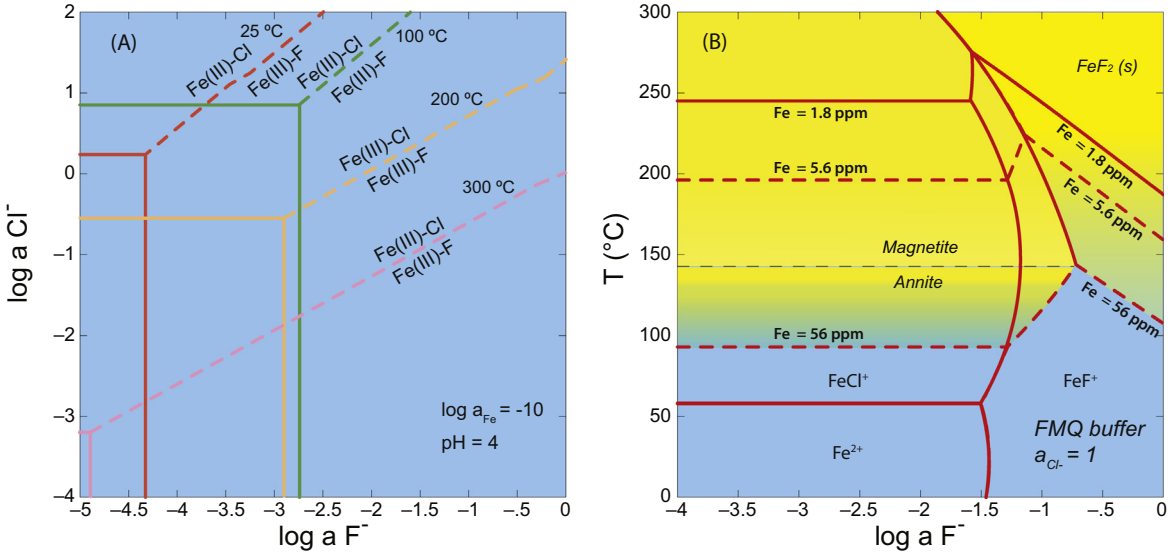

Fig. 13. Fe solubility and speciation. (A) F-Cl activity diagram for Fe(III) complexation at 25–300 °C, pH = 4, log $a_{Fe(III)} = -10$; the dashed line is the boundary between Cl dominated regime and F-dominated regime. The diagram shows that Fe chloride complexation becomes increasingly important with increasing temperature. (B) Effects of T and F activity on Fe solubility and speciation; pH is controlled by FMQ buffer; $a_{Cl^-} = 1$. The diagram shows Fe solubility decreases with increasing temperature and increasing F activity.

Cl/F area (Fig. 7A). Considering that natural magmatic F-rich fluids have Cl/F ratios at 100–1000 (Fig. 12), mixing of a F-bearing/rich magmatic fluid with granite-equilibrated fluids can be an effective mechanism to cause Fe precipitation. However, FeF_2(s) is not known as a mineral. In IOCG deposits, e.g., OD, fluorite is the predominant F-bearing mineral (Hitzman et al., 1992; Ehrig et al., 2012). The solubility of CaF_2(s) is much lower than FeF_2(s), and in addition even if FeF_2(s) forms locally it can be easily transformed to CaF_2(s) by Ca-bearing fluids. The processes can be described as:

$$FeF_2(s) + Ca^{2+} + 0.125\ SO_4^{2-} + H_2O = CaF_2(s) + 0.5\ Fe_2O_3(s) + 1.875H^+ + 0.125\ HS^-, \quad (11)$$

A positive correlation between Ca, Fe and the sulfide grade is recognized in the OD hematite ores, and fluorite is also the main Ca-bearing mineral phase (Ehrig et al., 2012). This phenomenon can be well explained by reaction (11), with an oxidized Ca-bearing fluid transforming FeF_2(s) to fluorite and precipitating hematite.

5.3. Role of fluorine-bearing fluids on extracting REE and U from granite

For REEs, our calculations show that LaF^{2+} is the predominant La species at $T > 100$ °C over a wide range in NaCl concentrations, with La chloride complexes being the most important at medium T (100–300 °C) in high salinity (> 2 m) brines (Fig. 9B). Although the calculated REE concentrations are rather low (< 1 ppm La), the presence of F does help increase REE solubility (compare Fig. 9A and C) during fluid-granite interaction.

Recent experimental studies pointed out that the stability of REE fluoride complexes had been overestimated by semi-empirical extrapolations, and concluded that Cl rather than F is responsible for REE transport in REE-rich (> 200 ppm) hydrothermal fluids (Migdisov et al., 2009; Williams-Jones et al., 2012; Migdisov and Williams-Jones, 2014). In our simulations, the fluid has lower REE concentration (< 1 ppm La in F-bearing fluids) than some natural REE ore-forming fluids, which can contain over 200 ppm REE (Banks et al., 1994). However, our calculated La concentrations are within the estimated concentration limit of REE that can be transported as fluoride complexes (< 1 ppm; Migdisov and Williams-Jones, 2014), and are consistent with earlier modellings that suggest that high temperatures and low pH are required to explain the high REE contents of some magmatic brines (Williams-Jones et al., 2012). Assuming granite as one of the possible sources of REEs at OD, the F-rich nature of the RDG granite will be a key factor enhancing REE extraction and leaching efficiency through fluid-rock interaction. Our modelling, however, suggests that the extraction of REE from granite by medium-salinity brines cannot produce highly enriched REE fluids such as those associated with hydrothermal REE mineralization at the Capitan Pluton, New Mexico (Banks et al., 1994). Extreme salinity (~40 wt% at Capitan), presence of additional ligands (e.g., sulfate), or low pH (i.e., more acidic than those resulting from rock-buffering) may be key to increasing REE solubility in these systems.

The transporting role of F on U is also a hot topic due to the common U-F association in many hydrothermal U deposits, including IOCGs (Hitzman and Valenta, 2005; Mark et al., 2000, 2006), volcanogenic U deposits (Chabiron et al., 2003), orogenic U deposits (McGloin et al., 2016) and vein-type deposits hosted in felsic rocks (Hu et al., 2008). It has been proposed that F can help transport U (Peiffert et al., 1996; McGloin et al., 2016) due to (1) the high stability of U(IV)-F and U(VI) O_2-F complexes relative to chloride complexes, resulting in higher U solubility in NaF solutions than in NaCl solutions (Peiffert et al., 1996), and (2) the increased partitioning coefficients between fluid and melt at higher HF concentrations (Keppler and Wyllie, 1991). Xing et al. (2018) show that U(IV/VI) fluoride complexes are the predominant species below 200 °C in F-Cl bearing (Cl/F = 100) fluids under both reduced and oxidized conditions. However, our calculations show that U(IV/VI) fluoride species never predominate under the simulated conditions. This is the result of the low F content (< 20 ppm) at lower T (< 300 °C) and high Cl/F ratios (> 1000) at salinities ≥ seawater (Fig. 7A,C) of the calculated fluid.

Taking granite as the primary source of F, the equilibrium reaction between fluids and granite is less likely to generate fluids with high F content due to the strong buffering effects of the granite (i.e., biotite, apatite and fluorite), which limits U-F complexation. In contrast, low temperature and oxidized fluids are more efficient and more likely to be the key in mobilizing U from the granite. Fluoride by itself may not be a key factor boosting the mobilization of U through hydrothermal alterations in granite-buffered hydrothermal systems.

5.4. Fluorine and porosity generation

Large scale brecciation is regarded as a defining feature of IOCG-type deposits since ores are usually hosted in breccias (Groves et al., 2010; Hitzman et al., 1992; Williams et al., 2005). The extensive brecciation has been attributed to the volatile fluids that are generated by contemporaneous magmatism during the ore formation (Groves et al., 2010; Williams et al., 2005). Our calculations show that HF(aq) is the predominant F species in fluids at 300–450 °C (Fig. 7B). Therefore, at OD, the high temperature and salinity magnetite-stage (Stage-I) mineralizing fluids favour the formation of HF(aq). Evidence for mineral dissolution from aggressive fluids can be found in the distinctively ragged and irregular shapes of the breccia clasts at OD (McPhie et al., 2011a, 2012).

The mechanism(s) responsible for the aggressive nature of the fluids remains uncertain. Three main hypotheses can be presented:

(i) Fluorine-rich fluids, most likely high temperature magmatic fluids similar for example to those plotted in Fig. 12, rise rapidly during tectonic events, reaching high level of disequilibrium with the host rock.
(ii) An aggressive fluid evolves via phase separation of a fluid that may have had an initial composition similar to that calculated here for fluid-granite interactions. Fig. 14 shows that a vapour evolving from such a fluid would have fHF(g)/fHCl(g) > 1 and hence would be highly aggressive. Phase separation is expected for shallow hydrothermal systems, which is likely to have relevance at OD given the large amounts of sediment clasts entrained at the top of the breccia (Williams et al., 2005). However, evidence for these vapours is expected to be limited, since they cause dissolution rather than mineral precipitation, and would be directly followed by fresh brines.
(iii) Our simulations show that fluids derived from the granite contain small but significant concentrations of HF(aq) and cause a dramatic increase of Si-F complexation at elevated temperature (Fig. 11). Therefore, even these relatively small amounts of dissolved F can help increase the permeability of the wall rocks by breaking Si—O bonds in silicates and releasing Si into fluids, helping to open grain boundaries and thereby weakening the rock. These could also possibly speed up mineral replacement kinetics, as has been shown for magmatic environments (Snow and Kidman, 1991).

6. Conclusions

We aimed to evaluate the role of F in extracting, transporting, and depositing metals in granite-related environments, with a special attention to explaining the nature of the association between F, U, REE and Fe found in typical IOCG deposits. As described in the introduction, four types of explanations have been proposed to explain the links between F, U, REE and Fe. The results of our thermodynamic modelling and in-situ XAS studies provide quantitative constraints on the feasibility and relative significance of each of these processes.

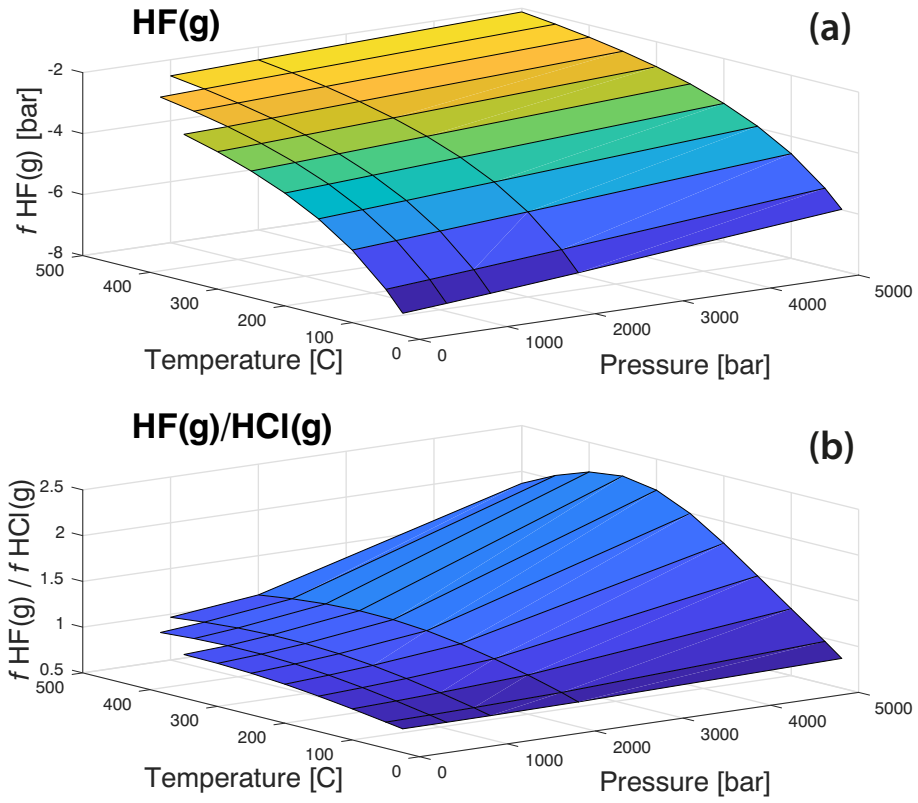

Fig. 14. Composition of vapour in equilibrium with a hydrothermal fluid assuming activities of HCl(aq) of 10^{-4} and HF(aq) 10^{-3} (corresponding to conditions at 450 °C in our simulations of fluid:granite equilibrium for the solution containing 3.5 m Cl_{tot}; Fig. 7). (a) *f* HF(g); (b) *f* HF(g)/*f* HCl(g).

(i) Fluoride increases the solubility of metals by forming stable coordination complexes.

Fluoride complexing was found to be insignificant for Fe and U transport. The modelling reveals that in the case of fluid-granite interaction, fluoride complexes play a significant role only in the case of REE (specifically, LaF^{2+} is the predominant species above 200 °C). However, addition of F did affect the solubility of U, Fe, and REE, albeit in a complex manner that is difficult to predict empirically. For example, higher REE contents in F-bearing models are the result of the difference in solubility of apatite-(CaOH) versus apatite-(CaF), which affects the phosphate contents of fluids and hence the solubility of REE-phosphate minerals such as monazite. The increased pH of the F-bearing fluids is responsible for the elevated U solubility in the form of uranyl carbonate complexes at low temperatures (< 250 °C).

(ii) Fluoride acts as a precipitating agent of Fe.

Our results show that F may act as a precipitating ligand for Fe under hydrothermal conditions (> 200 °C), due to the predicted reverse solubility of FeF_2(s). Mixing of F-rich fluids with ore-forming fluids may result in Fe precipitation due to the low solubility of Fe fluorides (reaction (10)), which may account for the F enrichment in the iron oxide ores in many IOCG deposits. In addition, fluoride appears to also reduce Fe solubility in models of fluid-granite interaction indirectly. The lower Fe solubility obtained in F-bearing compared to F-free models reflects the higher pH of the F-bearing fluids, and its effects on Fe-mineralogy and fO_2(g).

(iii) High F contents reflect the source of the ore fluids.

Our calculations show that F concentrations in fluids equilibrated with granite increase with increasing temperature, reaching a maximum value of ~70 ppm at ~450 °C. These F-concentrations are relatively low compared to F-concentrations in some magmatic fluids, yet the simulations confirm that a significant amount of F can be obtained by fluids via interaction with an assemblage of biotite, apatite-(CaF) and fluorite. However, extensive hydrothermal activities are required for significant amount of F to be mobilized from felsic rocks to form the large F endowment observed in some IOCG deposits (e.g., OD; Lala).

Our results also indicate that different hydrothermal events should be responsible for U (T < 200 °C) and REE (T > 250 °C) extraction, respectively. For OD, the magnetite stage fluids may favour REE mobilization from granite while the hematite stage fluids are preferential for U mineralization. The characteristic U-REE-F co-enrichment feature of the OD ore body may reflect the geochemical feature of the host granite and the regional felsic volcanic rocks, indicating the source link between genesis of IOCG deposits and hydrothermal alteration of regional felsic rocks.

(iv) The presence of HF(aq) improves leaching of metals and creates fluid pathways.

Our simulations show that the addition of F in the model results in a small increase in Si solubility, as a result of the higher pH of F-bearing fluids affecting the concentrations of $H_3SiO_4^-$ and $NaHSiO_3$(aq). Thermodynamic calculations indicate that Si-F complexes do not contribute significantly to solubility, even at 500 °C. However, even small concentrations of these species in solution could contribute to the effectiveness of fluid-rock interaction and fluid flow by helping to break Si—O bonds in silicate minerals. With respect to breccia formation, additional processes are required to create a large disequilibrium between fluids and rocks; this can be achieved by rapid flow of fluids along faults during seismic events, or by phase separation generating a HF-rich, highly aggressive vapour.

Overall, our data suggest that the common F + Fe + REE ± U association in many IOCG deposits may not only reflect the sourcing of the metals, but also that F contributes to the huge metal endowment of these deposits via a combination of processes, including changing the fluid pH, redox and the mineralogy, which further increase the metal (U and REE, but not Fe) carrying capacity of the fluids; and enhance the porosity and permeability of the breccia and the wall rocks, thus contributing to increased fluid pathways and ore-forming reactions. These provide a better understanding on how the F enrichment, a defining feature of IOCG deposits, is formed and the hydrothermal mineralizing histories of the deposits.

Acknowledgements

Research funding was provided by the Australian Research Council (grants DP140102765 to Joël Brugger and FT130100510 to Weihua Liu), and by the Russian Foundation for Basic Research (grant 17-05-00244 to Yuri Shvarov). The authors acknowledge the beamtime at the European Synchrotron Radiation Facility, as well as travel funding provided by the International Synchrotron Access Program (ISAP) managed by the Australian Synchrotron, part of ANSTO, and funded by the Australian Government. We are grateful to Allen Andersen and two anonymous reviewers for suggestions to improve the manuscript.

Appendix A. Supplementary data

Supplementary materials include Appendix 1. Details on thermodynamic modelling and Appendix 2. XANES spectra. Supplementary data to this article can be found online at https://doi.org/10.1016/j.chemgeo.2018.11.008.

References

Agangi, A., Kamenetsky, V.S., McPhie, J., 2012. Evolution and emplacement of high fluorine rhyolites in the Mesoproterozoic Gawler silicic large igneous province, South Australia. Precambrian Res. 208-211, 124–144.
Banks, D., Yardley, B., Campbell, A., Jarvis, K., 1994. REE composition of an aqueous magmatic fluid: a fluid inclusion study from the Capitan Pluton, New Mexico, U.S.A. Chem. Geol. 113, 259–272.
Bastrakov, E.N., Skirrow, R.G., Davidson, G.J., 2007. Fluid evolution and origins of iron oxide Cu-Au prospects in the Olympic Dam District, Gawler Craton, South Australia. Econ. Geol. 102, 1415–1440.
Bastrakov, E., Jaireth, S., Mernagh, T., 2010. Solubility of Uranium in hydrothermal fludis at 25° to 300 °C. Geosci. Aust. 29 (70633).
Bethke, C.M., 2008. Geochemical and Biogeochemical Reaction Modeling, 2nd ed. Cambridge University Press, New York.
Borisov, M.V., Shvarov, Y., 1992. Thermodynamics of Geochemical Processes (in Russian). Moscow State University Publishing House, Moscow (254 pp).
Brugger, J., 2007. BeerOz, a set of Matlab routines for the quantitative interpretation of spectrophotometric measurements of metal speciation in solution. Comput. Geosci. 33 (2), 248–261.
Brugger, J., Long, N., McPhail, D.C., Plimer, I., 2005. An active magmatic hydrothermal system: the Paralana hot springs, Northern Flinders Ranges, South Australia. Chem. Geol. 222 (1–2), 35–64.
Brugger, J., et al., 2007. An XAS study of the structure and thermodynamics of Cu(I) chloride complexes in brines up to high temperature (400 °C, 600 bar). Geochim. Cosmochim. Acta 71 (20), 4920–4941.
Brugger, J., et al., 2016. A review of the coordination chemistry of hydrothermal systems, or do coordination changes make ore deposits? Chem. Geol. 447, 219–253.
Bruland, K.W., 1983. Trace elements in seawater. In: Chemical Oceanography. Academic Press, London, pp. 157–220.
Bruyère, R., Prat, A., Goujon, C., Hazemann, J.-L., 2008. A new pressure regulation device using high pressure isolation valves. J. Phys. Conf. Ser. 121, 122003–122006.
Bunker, G., 2010. Introduction to XAFS - A Practical Guide to X-ray Absorption Fine Structure Spectroscopy. Cambridge University Press.
Chabiron, A., Cuney, M., Poty, B., 2003. Possible uranium sources for the largest uranium district associated with volcanism: the Streltsovka caldera (Transbaikalia, Russia). Mineral. Deposita 38 (2), 127–140.
Chantler, J., 1995. Theoretical form factor, attenuation, and scattering tabulation for Z = 1–92 from E = 1–10 eV to E = 0.4–1.0 MeV. J. Phys. Chem. Ref. Data 24, 71–591.
Chen, W.-T., Zhou, M.F., 2012. Paragenesis, stable isotopes, and molybdenite Re-Os isotope age of the Lala Iron-Copper Deposit, Southwest China. Econ. Geol. 107, 459–480.
Chen, W.-T., Zhou, M.F., 2014. Ages and compositions of primary and secondary allanite from the Lala Fe-Cu deposit, SW China: implications for multiple episodes of hydrothermal events. Contrib. Mineral. Petrol. 168, 1043.
Chen, W.T., Zhou, M.F., 2015. Mineralogical and geochemical constraints on mobilization and mineralization of rare Earth elements in the Lala Fe-Cu-(Mo, Ree) deposit, SW China. Am. J. Sci. 315 (7), 671–711.
Ehrig, K., McPhie, J., Kamenetsky, V., 2012. Geology and mineralogical zonation of the Olympic Dam iron oxide Cu-U-Au-Ag deposit, South Australia. Econ. Geol. Spec. Publ. 16, 237–267.
Etschmann, B.E., et al., 2010. An in situ XAS study of copper(I) transport as hydrosulfide complexes in hydrothermal solutions (25–592 °C, 180–600 bar): speciation and solubility in vapor and liquid phases. Geochim. Cosmochim. Acta 74 (16), 4723–4739.
Etschmann, B.E., et al., 2016. The role of Te(IV) and Bi(III) chloride complexes in hydrothermal mass transfer: an X-ray absorption spectroscopic study. Chem. Geol. 425, 37–51.
Finch, E.G., Tomkins, A.G., 2017. Fluorine and chlorine behaviour during progressive dehydration melting: consequences for granite geochemistry and metallogeny. J. Metamorph. Geol. 35 (7), 739–757.
Fulton, J.L., Hoffmann, M., Darab, J., 2000. An X-ray absorption fine structure study of copper(I) chloride coordination structure in water up to 325 °C. Chem. Phys. Lett. 330, 300–308.
Groves, D., Bierlein, F., Meinert, L., Hitzman, M., 2010. Iron oxide copper-gold (IOCG) deposits through Earth history: implications for origin, lithospheric setting, and distinction from other epigenetic iron oxide deposits. Econ. Geol. 105, 641–654.
Gu, Y., Gammons, C., Bloom, M., 1994. A one-term extrapolation method for estimating equilibrium constants of aqueous reactions at elevated temperatures. Geochim. Cosmochim. Acta 58 (17), 3545–3560.
Guillaumont, R., et al., 2003. Update on the Chemical Thermodynamics of Uranium, Neptunium, Plutonium, Americium and Technetium. Nuclear Energy Agency (NEA).
Gysi, A.P., Williams-Jones, A.E., 2015. The thermodynamic properties of bastnäsite-(Ce) and parisite-(Ce). Chem. Geol. 392, 87–101.
Haas, J., Shock, E., Sassani, D., 1995. Rare earth elements in hydrothermal systems: estimates of standard partial molal thermodynamic properties of aqueous complexes of the rare earth elements at high pressures and temperatures. Geochim. Cosmochim. Acta 59 (21), 4329–4350.
Helgeson, H.C., Kirkham, D.H., 1974. Theoretical prediction of the thermodynamic behavior of aqueous electrolytes at high pressures and temperatures: I. Summary of the thermodynamic/electrostatic properties of the solvent. Am. J. Sci. 274, 1089–1198.
Henderson, M.P., Miasek, V., Swaddle, T.W., 1971. Kinetics of thermal decomposition of aqueous perchloric acid. Can. J. Chem. 49, 317–324.
Hitzman, M., Valenta, R., 2005. Uranium in iron oxide-copper-gold (IOCG) systems. Econ. Geol. 100, 1657–1661.
Hitzman, M., Oreskes, N., Einaudi, M., 1992. Geological characteristics and tectonic setting of proterozoic iron oxide (Cu-U-Au-REE) deposits. Precambrian Res. 58, 241–287.
Hu, R.Z., et al., 2008. Uranium metallogenesis in South China and its relationship to crustal extension during the Cretaceous to Tertiary. Econ. Geol. 103 (3), 583–598.
James, R.H., et al., 2014. Composition of hydrothermal fluids and mineralogy of associated chimney material on the East Scotia Ridge back-arc spreading centre. Geochim. Cosmochim. Acta 139, 47–71.
Jayanetti, S., Mayanovic, R.A., Anderson, A.J., Bassett, W.A., Chou, I.M., 2001. Analysis of radiation-induced small Cu particle cluster formation in aqueous $CuCl_2$. J. Chem. Phys. 115 (2), 954–962.
Johnson, J.P., Cross, K., 1995. U-Pb geochronology constrains on the genesis of the Olympic Dam Cu-U-Au-Ag Deposit, South Australia. Econ. Geol. 90, 1046–1063.
Joly, Y., 2001. X-ray absorption near-edge structure calculations beyond the muffin-tin approximation. Phys. Rev. B 63, 125120–125129.
Jonsson, E., Troll, V.R., Hogdahl, K., Harris, C., Weis, F., Nilsson, K.P., Skelton, A., 2013. Magmatic origin of giant 'Kiruna-type' apatite-iron-oxide ores in central Sweden. Sci. Rep. 3, 1644 (8 pages).
Kelly, S., Hesterberg, D., Ravel, B., 2008. Analysis of solis and minerals using X-ray absorption spectroscopy (chapter 14), methods of solis analysis. In: Part 5. Mineralogical Methods. Soil Sciences Society of America, Madison, USA.
Keppler, H., 1993. Influence of fluorine on the enrichment of high field strength trace elements in granitic rocks. Contrib. Mineral. Petrol. 114, 479–488.
Keppler, H., Wyllie, P.J., 1991. Partitioning of Cu, Sn, Mo, W, U, and Th between melt and aqueous fluid in the systems haplogranite-H_2O-HCl and haplogranite-H_2O-HF. Contrib. Mineral. Petrol. 109, 139–150.
Kirchenbaur, M., et al., 2016. Uranium and Sm isotope studies of the supergiant Olympic Dam Cu–Au–U–Ag deposit, South Australia. Geochim. Cosmochim. Acta 180, 15–32.
Kline, W., Fogler, S., 1981. Dissolution of silicate minerals by hydrofluoric acid. Ind. Eng. Chem. Fundam. 20, 155–161.
Kontonikas-Charos, A., et al., 2017. Feldspar evolution in the Roxby Downs granite, host to Fe-oxide Cu-Au-(U) mineralisation at Olympic Dam, South Australia. Ore Geol. Rev. 80, 838–859.
Lemire, R., et al., 2013. Chemical Thermodynamics of IRON. OECD Nuclear Energy Agency Data Bank. North Holland Elsevier Science Publishers B. V., Amsterdam, The Netherlands.
Lemmon, E.W., McLinden, M.O., Friend, D.G., 2000. Thermophysical properties of fluid systems. In: Mallard, W.G., Linstrom, P.J. (Eds.), NIST Chemistry WebBook, NIST Standard Reference Database. National Institute of Standards and Technology, G., MD..
Ling, M.X., Liu, Y.L., Williams, I.S., Teng, F.Z., Yang, X.Y., Ding, X., Wei, G.J., Xie, L.H., Deng, W.F., Sun, W.D., 2013. Formation of the world's largest REE deposit through protracted fluxing of carbonatite by subduction-derived fluids. Sci. Rep. 3 (8 pages).
Liu, W., et al., 2006. UV–Vis spectrophotometric and XAFS studies of ferric chloride complexes in hyper-saline LiCl solutions at 25–90 °C. Chem. Geol. 231 (4), 326–349.
Liu, W.H., Brugger, J., Etschmann, B., Testemale, D., Hazemann, J.L., 2008. The solubility of nantokite (CuCl(s)) and Cu speciation in low-density fluids near the critical isochore: an in-situ XAS study. Geochim. Cosmochim. Acta 72 (16), 4094–4106.
Liu, W., et al., 2011. Speciation and thermodynamic properties for cobalt chloride complexes in hydrothermal fluids at 35–440 °C and 600 bar: an in-situ XAS study. Geochim. Cosmochim. Acta 75 (5), 1227–1248.
Lottermoser, B.G., Cleverley, J.S., 2007. Controls on the genesis of a high-fluoride thermal

spring: Innot Hot Springs, north Queensland. Aust. J. Earth Sci. 54 (4), 597–607.
Mark, G., Oliver, N.H.S., Willams, P.J., Valenta, R., Crookes, R., 2000. The Evolution of the Ernest Henry Fe-Oxide-(Cu-Au) Hydrothermal System, Hydrothermal Iron Oxide Copper-Gold & Related Deposits: A Global Perspective. PGC Publishing, Adelaide, pp. 123–136.
Mark, G., Oliver, N.H.S., Williams, P.J., 2006. Mineralogical and chemical evolution of the Ernest Henry Fe oxide–Cu–Au ore system, Cloncurry district, northwest Queensland, Australia. Mineral. Deposita 40 (8), 769–801.
McGloin, M.V., et al., 2016. Release of uranium from highly radiogenic zircon through metamictization: the source of orogenic uranium ores. Geology 44 (1), 15–18.
McPhie, J., et al., 2011a. The fluorine link between a supergiant ore deposit and a silicic large igneous province. Geology 39 (11), 1003–1006.
McPhie, J., Kamenetsky, V.S., Chambefort, I., Ehrig, K., Green, N., 2011b. Origin of the supergiant Olympic Dam Cu-U-Au-Ag deposit, South Australia: was a sedimentary basin involved? Geology 39 (8), 795–798.
McPhie, J., et al., 2012. The fluorine link between a supergiant ore deposit and a silicic large igneous province Reply. Geology 40 (8), e276.
Mei, Y., et al., 2015. Zinc complexation in chloride-rich hydrothermal fluids (25–600 °C): a thermodynamic model derived from ab initio molecular dynamics. Geochim. Cosmochim. Acta 150, 265–284.
Melnik, M., Ondrejkovicova, I., Vancova, V., Holloway, C.E., 1997. Structural aspects of iron coordination compounds. 1. Monomeric derivatives. Rev. Inorg. Chem. 17 (2–3), 55–286.
Migdisov, A., Williams-Jones, A.E., 2014. Hydrothermal transport and deposition of the rare earth elements by fluorine-bearing aqueous liquids. Mineral. Deposita 49, 987–997.
Migdisov, A., Williams-Jones, A.E., Wagner, T., 2009. An experimental study of the solubility and speciation of the rare earth elements (III) in fluoride- and chloride-bearing aqueous solutions at temperatures up to 300 °C. Geochim. Cosmochim. Acta 73 (23), 7087–7109.
Migdisov, A., Williams-Jones, A.E., Brugger, J., Caporuscio, F.A., 2016. Hydrothermal transport, deposition, and fractionation of the REE: Experimental data and thermodynamic calculations. Chem. Geol. 439, 13–42.
Montreuil, J.-F., Potter, E.G., Corriveau, L., Davis, W.J., 2016. Element mobility patterns in magnetite-group IOCG systems: the Fab IOCG system, Northwest Territories, Canada. Ore Geol. Rev. 72, 562–584.
Munoz, J., 1984. F-OH and Cl-OH exchange in micas with applications to hydrothermal ore-deposits. Rev. Mineral. Geochem. 13 (1), 469–493.
Oliver, N.H.S., et al., 2004. Modeling the role of sodic alteration in the genesis of Iron Oxide-Copper-Gold deposits, Eastern Mount Isa Block, Australia. Econ. Geol. 99, 1145–1176.
Oreskes, N., Einaudi, M., 1990. Origin of rare earth element-enriched hematite breccias at the Olympic Dam Cu-U-Au-Ag deposit, Roxby Downs, South Australia. Econ. Geol. 85, 1–28.
Oreskes, N., Einaudi, M., 1992. Origin of Hydrothermal fluids at Olympic Dam: preliminary results from fluid inclusions and stable isotope. Econ. Geol. 87, 64–90.
Pasero, M., Kampf, A.R., Ferraris, C., Pekov, I.V., Rakovan, J., White, T.J., 2010. Nomenclature of the apatite supergroup minerals. Eur. J. Mineral. 22, 163–179.
Pearson, R., 1963. Hard and soft acids and bases. J. Am. Chem. Soc. 85, 3533–3539.
Peiffert, C., Nguyen-Trung, C., Cuney, M., 1996. Uranium in granitic magmas: part 2. Experimental determination of uranium solubility and fluid-melt partition coefficients in the uranium oxide-haplogranite-H_2O-NaX(X = Cl, F) system at 770 °C, 2 kbar. Geochim. Cosmochim. Acta 60 (9), 1515–1529.
Pokrovski, G.S., Roux, J., Hazemann, J.L., Testemale, D., 2005. An X-ray absorption spectroscopy study of argutite solubility and aqueous Ge(IV) speciation in hydrothermal fluids to 500 °C and 400 bar. Chem. Geol. 217, 127–145.
Pollard, P.J., 2000. Evidence of a Magmatic Fluid and Metal Source for Fe-Oxide Cu-Au Mineralization. 1. PGC Publishing, pp. 27–41.
Ravel, B., Newville, M., 2005. ATHENA, ARTEMIS, HEPHAESTUS: data analysis for X-ray absorption spectroscopy using IFEFFIT. J. Synchrotron Radiat. 12, 537–541.
Rehr, J., et al., 2009. Ab initio theory and calculations of X-ray spectra. C. R. Phys. 10, 548–559.
Rieder, M., Cavazzini, G., D'Yakonov, Y.S., Frank-Kamenetskii, V.A., Gottardi, G., Guggenheim, S., Koval, P.V., Muller, G., Neiva, A.M.R., Radoslovich, E.W., Robert, J.L., Sassi, F.P., Takeda, H., Weiss, Z., Wones, D.R., 1998. Nomenclature of the micas. Can. Mineral. 36, 905–912.
Ryzhenko, B.N., Bryzgalin, O.V., Artamkina, Y., Spasennykh, M.Y., Shapkin, A.I., 1985. An electronic model for the electrolytic dissociation of inorganic substances dissolved in water. Geochem. Int. 22, 138–144.
Saffré, D., et al., 2011. In situ UV-visible spectrum acquisition of Br_3^-. Investigations of concentrated HBr aqueous solutions under 13-keV X-rays. J. Phys. Conf. Ser. 261, 012013.
Salvi, S., Williams-Jones, A.E., 1996. The role of hydrothermal processes in concentrating high-field strength elements in the Strange Lake peralkaline complex, northeastern Canada. Geochim. Cosmochim. Acta 60, 1917–1932.
Schlegel, T., Heinrich, C.A., 2015. Lithology and hydrothermal alteration control the distribution of copper grade in the prominent hill iron oxide-copper-gold deposit (Gawler Craton, South Australia). Econ. Geol. 110, 1953–1994.
Seward, T.M., Barnes, H.L., 1997. Chapter 9: metal transport by hydrothermal ore fluids. In: Geochemistry of Hydrothermal Ore Deposits. John Willey & Sons, pp. 435–486.
Seward, T.M., Williams-Jones, A.E., Migdisov, A.A., 2014. The chemistry of metal transport and deposition by ore-forming hydrothermal fluids. In: Treatise on Geochemistry, Second ed. Vol. 13. Elsevier Ltd, pp. 29–57.
Shvarov, Y.V., 2008. HCh: New potentialities for the thermodynamic simulation of geochemical systems offered by windows. Geochem. Int. 46 (8), 834–839.
Shvarov, Y., 2015. A suite of programs, OptimA, OptimB, OptimC, and OptimS compatible with the Unitherm database, for deriving the thermodynamic properties of aqueous species from solubility, potentiometry and spectroscopy measurements. Appl. Geochem. 55, 17–27.
Shvarov, Y., Bastrakov, E., 1999. HCh: A Software Package for Geochemical Equilibrium Modelling. User's Guide.
Sillitoe, R.H., 2003. Iron oxide-copper-gold deposits: an Andean view. Mineral. Deposita 38 (7), 787–812.
Skirrow, R., et al., 2007. Timing of iron oxide Cu-Au-(U) hydrothermal activity and Nd isotope constraints on metal sources in the Gawler Craton, South Australia. Econ. Geol. 102, 1441–1470.
Smith, M., Henderson, P., 2000. Preliminary fluid inclusion constraints on fluid evolution in the bayan Obo Fe-REE-Nb deposit, Inner Mongolia, China. Econ. Geol. 95, 1371–1388.
Snow, E., Kidman, S., 1991. Effect of fluorine on solid-state alkali interdiffusion rates in feldspar. Nature 349, 231–233.
Soli, A., Byrne, R., 1996. The hydrolysis and fluoride complexation behavior of Fe(III) at 25 °C and 0.68 molal ionic strength. J. Solut. Chem. 25 (8), 773–785.
Solomon, L.R., Bond, A.M., Bixler, J.W., Hallenbeck, D.R., Logsdon, K.M., 1983. Stability of monofluoride complexes of the Irving-Williams series acceptors in methanol. Inorg. Chem. 22, 1644–1648.
Sverjensky, D.A., Shock, E.L., Helgeson, H.C., 1997. Prediction of the thermodynamic properties of aqueous metal complexes to 1000 °C and 5 kb. Geochim. Cosmochim. Acta 6 (7), 1359–1412.
Tagirov, B., Diakonov, I., Devina, O., Zotov, A., 2000. Standard ferric–ferrous potential and stability of $FeCl^{2+}$ to 90 °C. Thermodynamic properties of $Fe^{3+}_{(aq)}$ and ferric-chloride species. Chem. Geol. 162, 193–219.
Tanger, J.C., Helgeson, H.C., 1988. Calculation of the thermodynamic and transport properties of aqueous species at high pressures and temperatures: revised equations of state for the standard partial molal properties of ions and electrolytes. Am. J. Sci. 288, 19–98.
Testemale, D., Argoud, R., Geaymond, O., Hazemann, J.-L., 2005. High pressure/high temperature cell for x-ray absorption and scattering techniques. Rev. Sci. Instrum. 76 (4), 043905.
Testemale, D., Brugger, J., Liu, W., Etschmann, B., Hazemann, J.-L., 2009a. In-situ X-ray absorption study of iron(II) speciation in brines up to supercritical conditions. Chem. Geol. 264 (1–4), 295–310.
Testemale, D., et al., 2009b. An X-ray absorption study of the dissolution of siderite at 300 bar between 50 °C and 100 °C. Chem. Geol. 259 (1–2), 8–16.
Testemale, D., Sanchez-Valle, C., Goujon, C., Pokrovski, G.S., Guyot, F., 2016. Speciation and solubility of Fe(III) in crustal fluids. In: Goldschmidt Abstracts. 2016. pp. 3112.
Teufer, G., 1964. The crystal structure of beta iron(III) trifluoride trihydrate, β-$FeF_3(H_2O)_3$. Acta Cryst 17, 1480.
Tian, Y., et al., 2014. Speciation and thermodynamic properties of manganese(II) chloride complexes in hydrothermal fluids: in situ XAS study. Geochim. Cosmochim. Acta 129, 77–95.
Timofeev, A., et al., 2018. Uranium transport in acidic brines under reducing conditions. Nat. Commun. 9 (1469).
Tromp, M., Moulin, J., Reid, G., Evans, J., 2007. CrK-edge XANES spectroscopy: ligand and oxidation state dependence - what is oxidation state? In: X-Ray Absorption Fine Structure-XAFS13. 882. pp. 699–701.
van Middlesworth, P.E., Wood, S.A., 1998. The aqueous geochemistry of the rare earth elements and yttrium. Part 7. REE, Th and U contents in thermal springs associated with the Idaho batholith. Appl. Geochem. 13 (7), 861–884.
Velbel, M., 1999. Bond strength and the relative weathering rates of simple orthosilicates. Am. J. Sci. 299, 679–696.
Walker, J.B., Choppin, G.R., 1967. Thermodynamic parameters of fluoride complexes of the lanthanides. Adv. Chem. 71, 127–140.
Wells, C.F., Salam, M.A., 1967. Complex formation between Fe(II) and inorganic anions. Part1. Effect of simple and complex halide ions on the Fe(II) + H_2O_2 reaction. Trans. Faraday Soc. 63, 620–629.
Williams, P.J., et al., 2005. Iron Oxide Copper-Gold Deposits: Geology, Space-time Distribution, and Possible Modes of Origin. Economic Geology, 100th Anniversary Volume. pp. 371–405.
Williams-Jones, A.E., Samson, I.M., Olivo, C.R., 2000. The genesis of hydrothermal fluorite-REE deposits in the Gallinas Mountains, New Mexico. Econ. Geol. 95, 327–342.
Williams-Jones, A.E., Migdisov, A.A., Samson, I.M., 2012. Hydrothermal mobilisation of the rare earth elements - a tale of "Ceria" and "Yttria". Elements 8 (5), 55–360.
Xing, Y., Mei, Y., Etschmann, B., Liu, W., Brugger, J., 2018. Uranium transport in F-Cl-bearing fluids and hydrothermal upgrading of U-Cu ores in IOCG Deposits. Geofluids 2018, 6835346 (22 pages).
Yardley, B., 2005. Metal concentrations in crustal fluids and their relationship to ore formation. Econ. Geol. 100, 613–632.
Zhong, R., Brugger, J., Chen, Y., Li, W., 2015a. Contrasting regimes of Cu, Zn and Pb transport in ore-forming hydrothermal fluids. Chem. Geol. 395, 154–164.
Zhong, R., Brugger, J., Tomkins, A.G., Chen, Y., Li, W., 2015b. Fate of gold and base metals during metamorphic devolatilization of a pelite. Geochim. Cosmochim. Acta 171, 338–352.
Zhu, C., Sverjensky, D., 1991. Partioning of F-Cl-OH between minerals and hydrothermal fluids. Geochim. Cosmochim. Acta 55, 1837–1858.
Zhu, C., Sverjensky, D., 1992. F-Cl-OH partitioning between biotite and apatite. Geochim. Cosmochim. Acta 56, 3435–3467.

Chapter 3

Uranium transport in F-Cl-bearing fluids and hydrothermal upgrading of U-Cu ores in IOCG deposits

Xing, Yanlu[1]; Mei, Yuan[1,2]; Etschmann, Barbara[1]; Liu, Weihua[2] and Brugger, Joël[1,*]

1. School of Earth, Atmosphere and the Environment, Monash University, Clayton, VIC 3800, Australia

2. CSIRO Mineral Resources, Clayton, VIC 3168, Australia

Hindawi
Geofluids
Volume 2018, Article ID 6835346, 22 pages
https://doi.org/10.1155/2018/6835346

Research Article

Uranium Transport in F-Cl-Bearing Fluids and Hydrothermal Upgrading of U-Cu Ores in IOCG Deposits

Yanlu Xing,[1] Yuan Mei,[1,2] Barbara Etschmann,[1] Weihua Liu,[2] and Joël Brugger[1]

[1]*School of Earth, Atmosphere and the Environment, Monash University, Clayton, VIC 3800, Australia*
[2]*CSIRO Mineral Resources Flagship, Clayton, VIC 3168, Australia*

Correspondence should be addressed to Joël Brugger; joel.brugger@monash.edu

Received 17 December 2017; Accepted 24 May 2018; Published 28 August 2018

Academic Editor: Ferenc Molnar

Uranium mineralization is commonly accompanied by enrichment of fluorite and other F-bearing minerals, leading to the hypothesis that fluoride may play a key role in the hydrothermal transport of U. In this paper, we review the thermodynamics of U(IV) and U(VI) complexing in chloride- and fluoride-bearing hydrothermal fluids and perform mineral solubility and reactive transport calculations to assess equilibrium controls on the association of F and U. Calculations of uraninite and U_3O_8(s) solubility in acidic F-rich (Cl : F = 100 [ppm-based]) hydrothermal fluids at 25–450°C, 600 bar, show that U(IV)-F complexes (reducing conditions) and uranyl-F complexes (oxidizing conditions) predominate at low temperature (T < ~200°C), while above ~250°C, chloride complexes predominate in acidic solutions. In the case of uraninite, solubility is predicted to decrease dramatically as $U(IV)Cl_2^{2+}$ becomes the predominant U species at T > 260°C. In contrast, the solubility of U_3O_8(s) increases with increasing temperatures. We evaluated the potential of low-temperature fluids to upgrade U and F concentrations in magnetite-chalcopyrite ores. In our model, an oxidized (hematite-rich) granite is the primary source of F and has elevated U concentration. Hydrothermal fluids (15 wt.% NaCl equiv.) equilibrated with this granite at 200°C react with low-grade magnetite-chalcopyrite ores. The results show that extensive alteration by these oxidized fluids is an effective mechanism for forming ore-grade Cu-U mineralization, which is accompanied by the coenrichment of fluorite. Fluorite concentrations are continuously upgraded at the magnetite-hematite transformation boundary and in the hematite ores with increasing fluid : rock (F/R) ratio. Overall, the model indicates that the coenrichment of F and U in IOCG ores reflects mainly the source of the ore-forming fluids, rather than an active role of F in controlling the metal endowment of these deposits. Our calculations also show that the common geochemical features of hematite-dominated IOCG deposits can be related to a two-phase process, whereby a magnetite-hematite-rich orebody (formed via a number of processes/tectonic settings) is enriched in Cu ± U and F during a second stage (low temperature, oxidized) of hydrothermal circulation.

1. Introduction

1.1. The U-F Association. Many hydrothermal uranium (U) ores are accompanied by high concentrations of fluorine (F) in the form of fluorite and/or other F-bearing minerals such as fluorapatite [1–4]. Such U-mineralizing systems include IOCG, orogenic U deposits, and volcanogenic and vein-type deposits hosted in felsic rocks [2, 5–7]. Examples of deposits in which both U and F are enriched are listed in Table 1.

The enrichment of fluorine is an important feature of many IOCG-mineralizing systems, including Olympic Dam (OD) [6, 8] and Ernest Henry in Australia [9, 10]; Salobo [11] and Igarape Bahia [8] in the Carajás district, Brazil; and Lala [12, 13] in southwest China. This led to the hypothesis that fluorine may play a key role in the leaching and transport of metals for IOCG and in controlling the element association found in this class [3, 11]. For example, in the Olympic Dam deposit, which represents the world's largest U resource [14–17], the mined ores contain about 2.5 wt.% fluorite, which adds up to 10^8 t of F from fluorite alone [3]. The Ernest Henry in Cloncurry district, Australia, has a total reserve of 167 Mt ores with up to 50 ppm U, and fluorite is one of the main accessory phases closely associated with Cu-U-Au mineralization [6, 10]. Similarly, fluorite is enriched in the

Table 1: Summary of uranium deposits that are rich in fluorine.

Deposit type	Name	Reserve (Mt)	Grade	Fluorine enrichment	Host rock	Ore-forming fluids	References
IOCG	Olympic Dam, Australia	545	480 ppm U	Up to 2.5 wt.% fluorite in ores; 10^8 t F; F-bearing minerals, that is, fluorapatite and REE minerals	Granite	Magnetite stage: $T > 400^{\circ}C$; hematite stage: $T = 150 – 300^{\circ}C$	Billiton [41]; Oreskes and Einaudi [16]; McPhie et al. [3]
	Ernest Henry, Australia	167	50 ppm U	Fluorite is one of the main gangue minerals in ores	Plagioclase-phyric meta-andesitic rocks	$T = 300 – 500^{\circ}C$	Mark et al. [9]; Hitzman and Valenta [6]; Mark et al. [10]; Williams et al. [17]
	Prominent Hill, Australia	97	97 ppm U	One of the main phases in Cu-Au-U ores	Meta-andesitic rocks	$T = 110 – 475^{\circ}C$	Hitzman and Valenta [6]; Tobias (2015)
	Salobo, Brazil	789	32–57 ppm	Main phase in the ores			de Melo et al. [11]
	Igarape Bahia, Brazil	219	99–170 ppm	Enriched in magnetite breccias	Metavolcano-sedimentary sequence		Tallarico et al. [8]
Orogenic U deposits	Mount Isa Inlier, Australia	225	6 ppm	High F content in ores and host rocks	Granitic intrusions		Gregory et al. [42]; Polito et al. [43]; McGloin et al. [2]
Granite/volcanic rock-hosted U deposits	Xiangshan, China	0.02–0.05	0.1–0.3% U	Fluorite consists of one of the main phase in ores	Felsic volcanic rock and granite porphyry	$T = 115 – 275^{\circ}C$	Chabiron et al. [22]; Hu et al. [7]
	Streltsovka caldera, Russia	0.127	0.18–0.2% U	1.4–2.7% F in rhyolite	Felsic volcanic rocks/ rhyolites		Chabiron et al. [22]; Cuney [27]
	Xiazhuang, China	0.003–0.01	0.1–0.3%	Ore-forming fluids have elevated F concentration	Granite	$T = 150 – 250^{\circ}C$	Hu et al. [7]

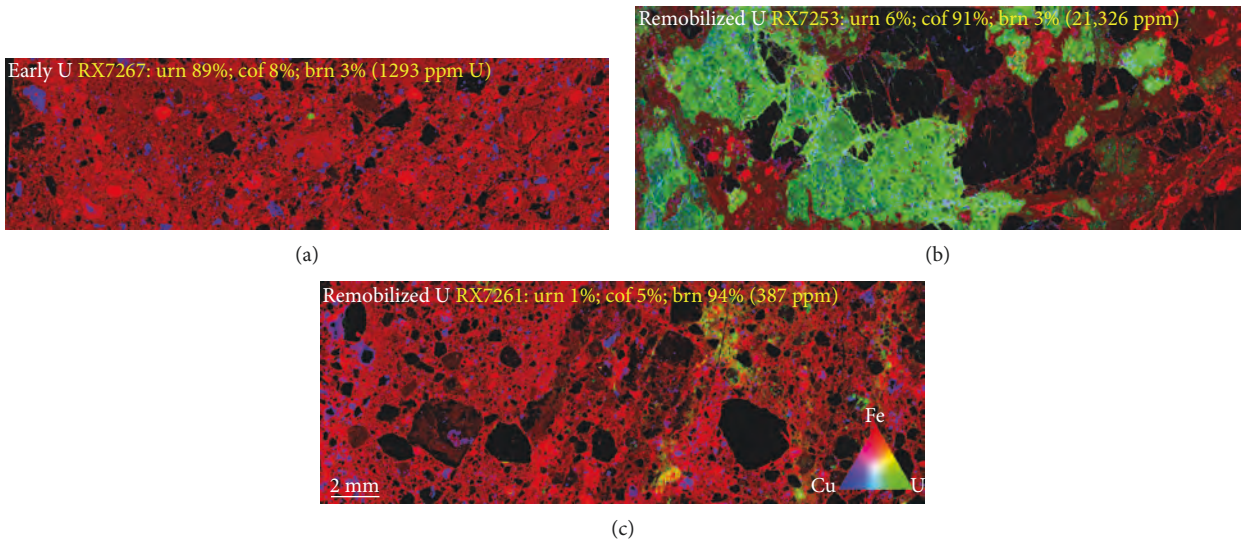

Figure 1: Contrasting U-Cu distribution in three samples from the Olympic Dam IOCG deposit, South Australia, illustrated by synchrotron-micro-XRF imaging of selected samples described in detail by Macmillan et al. [15]. Mineralogical and grade data are taken from Macmillan et al. [15]. The RGB maps show Cu (blue), U (green), and Fe (red) distribution (colour scale at the bottom right). In (a) (uraninite-dominated ore), Cu and U distribution mirror each other, suggesting coprecipitation of the two metals. Mineralogy is dominated by uraninite. In (b) and (c), the main U minerals are coffinite and brannerite, and U distribution is diffuse and overprints the ore textures, suggesting a secondary origin. The maps were collected at the XFM beamline, Australian Synchrotron. See Li et al. [40] for details of data collection and processing.

stage III ore assemblages together with Cu-Mo sulfides in the Lala deposit [18].

Fluorite is usually enriched in volcanogenic and vein-type U deposits that are related to igneous rocks [4, 19–21]. For example, fluorite veins are common at the Streltsovka caldera U deposit in Russia. The deposit is hosted in F-rich rhyolite (containing 1.4–2.7 wt.% F) over a granitic basement, and both rhyolite and granites are thought to be the source of F and U mineralization [22]. Many vein-type U deposits found in South China (e.g., Xiangshan, Xiazhuang, Hechaokeng, and Wuqilin) are hosted by felsic intrusive or volcanic rocks and formed from fluids (100–250°C) that were enriched in F [7]. A close association between fluorite and U has also been reported in some orogenic U deposits, such as in the Mount Isa Inlier, Australia [2]. Again, felsic rocks represent the source of U and F, with F assumed to facilitate U hydrothermal transport.

In summary, these studies reveal a clear association between F and U in the ores and sometimes in the likely source region of fluids/metals. Many studies suggest that this association is significant for understanding ore formation, with explanations focusing mainly on two aspects: (i) F helps extract U or (ii) the F-rich nature of the fluids reflects the source of the metals. In the case of felsic melt-aqueous-phase separation relevant for magmatic hydrothermal deposits (e.g., Rijssing alaskites from Namibia [23] and Kvanefjeld deposit in the Ilimaussaq intrusion [24]), high-temperature experiments show that the partitioning coefficient of U between aqueous fluid and melt ($K_D = c_{fluid}/c_{melt}$) strongly increases with increasing HF content at 750°C [25], as does the solubility of uraninite in uraninite-melt-fluid systems (up to twenty times more U than in chloride solution with the same salinity at 770°C [26]). These experimental studies demonstrate the role of complexing by fluoride for the hydrothermal transport of U in high-temperature (≥750°C) magmatic hydrothermal systems.

Several studies have investigated the mechanisms by which hydrothermal fluids mobilize U to form high-grade U mineralization from low- to medium-temperature hydrothermal fluids (≤400°C [22, 27, 28]). The current consensus is that oxidized fluids are favorable for U mobilization, while reduction is the key for U precipitation [27, 29–32]. In this context, the role of F in controlling U transport remains poorly understood. According to the hard-soft acid-base theory, U(VI) and U(IV) are hard cations that form strong complexes with the hard ligand F^- [33] but weaker complexes with the soft Cl^- ligand. The stronger affinity of U for F is balanced by the fact that in natural fluids, Cl : F ratios are high (usually > ~100 [34, 35]), because the solubility of F is limited by the solubility of minerals such as fluorite, fluorapatite, and F-bearing biotite. Hence, a quantitative approach is required to estimate the role of fluoride as a transporting agent for U in natural fluids.

1.2. Uranium Remobilization and Upgrading: the Olympic Dam Example. The main U minerals at the Olympic Dam are coffinite, brannerite, and uraninite-pitchblende, with minor to trace amounts of U hosted in hematite, thorite-uranothorite, thorianite, crandallite, xenotime-(Y), zircon, REE-group minerals, pyrite, chalcopyrite, bornite, and chalcocite [36]. At the deposit scale, the average proportions of U minerals are 56% coffinite, 31% brannerite, and 13% uraninite; however, individual samples show large variations ([36]; see Figure 1).

The relative timing of U versus Cu mineralization at OD has received much attention recently. Macmillan et al. [15] divided OD uraninite into four groups based on textural and compositional characteristics. Class 1 uraninite has a

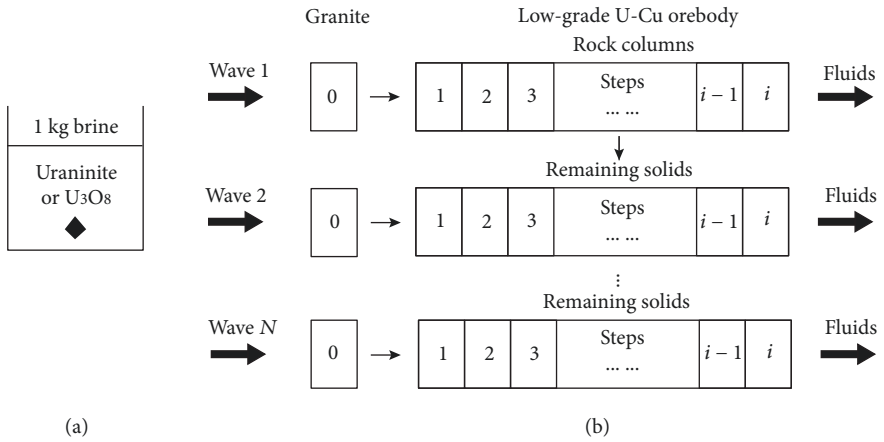

Figure 2: Diagram for models used for thermodynamic calculation: (a) aliquot model; (b) step-flow-through reactor model.

cubic-euhedral habit and relatively high Pb and ΣREY concentrations, as well as up to 7.42 wt.% ThO_2; this indicates precipitation from magmatic or high-temperature (>350°C) hydrothermal fluids. In contrast, other uraninite classes show low ThO_2 contents, suggesting precipitation from lower-temperature (<250°C) hydrothermal fluids [37]. The late, massive, Class 4 uraninite has the lowest Pb and ΣREE + Y, and Macmillan et al. [15] suggest that it evolved from earlier-formed uraninites (Classes 1–3). X-ray maps of U and Cu distribution in ores from OD (Figure 1) illustrate the importance of secondary U mobility at OD. In a sample where most U is hosted in uraninite, the Cu and U distributions mirror each other, suggesting coprecipitation (Figure 1(a)). In contrast, U and Cu distributions differ markedly in a sample containing abundant coffinite; U mineralization is overprinting the ore textures, as well as occupying late fractures (Figure 1(b)). Similarly, in samples dominated by brannerite, U distribution appears to overprint early ore textures (Figure 1(c)); this is consistent with textural observations by Macmillan et al., [38] indicating a secondary origin for the majority of coffinite and brannerite. A protracted U mobility at OD is further supported by the U and Sm isotope study of Kirchenbaur et al. [39], which adds to geochronological evidence for gradual addition of U in several stages over 1000 Ma at elevated temperatures. Kirchenbaur et al.'s [39] data also indicate that U is sourced primarily from upper crustal (likely igneous) lithologies.

1.3. Aims. We calculated U(IV/VI) speciation in the simplified U-F-Cl-H_2O-fO_2 system at 25–450°C to compare the relative importance of F and Cl on U transport based on our current understanding of U thermodynamics. We have updated the thermodynamic properties of relevant U minerals and complexes, in particular U chloride and fluoride species compiled and reviewed by Bastrakov et al. [30] with the latest published data, and briefly discussed the choice of the key properties in our model. We then conducted reactive transport simulations to model the fluid-ore/rock interactions to help understand the hydrothermal mobilization of U and U-Fe-Cu-F association in IOCG systems, taking Olympic Dam as an example with well-described geological and mineralogical features.

Table 2: Simulated system for U-Cl-F-H_2O equilibrium.

	Reduced fluid	Oxidized fluid	Units
H_2O	1	1	kg
Uraninite	60	0	mmol
U_3O_8(s)	0	20	mmol
HCl	0.5	0.5	mol
HF	0.5	0.5	mol
NaCl	150	150	g
NaF	1.5	1.5	g
O_2	0	1	g

2. Methods and Strategies for Thermodynamic Modelling

2.1. Mineral Solubility Calculations Using the Aliquot-Type Model. We use the aliquot-type equilibration model [44] to calculate the solubility of U minerals and the aqueous U speciation under simple P-T-x conditions for the H_2O-U-NaCl-NaF-HCl-HF system (Figure 2(a)). In these models, one kilogram of acidic saline water with fixed Cl : F ratio of 100 (solution compositions, see Table 2) was reacted with uraninite (60 mmol) and U_3O_8(s) (20 mmol) to investigate the relative effects of fluoride and chloride. This Cl : F ratio reflects the composition of F-rich fluids in nature, which usually have Cl : F ratios of 100–200 [34, 35]. The salinity of the fluids was fixed at 15 wt.% NaCl equivalent (2.56 molal), which is similar, for example, to the hematite stage fluids at Olympic Dam [16, 45].

2.2. Step-Flow-Through Reactor Model. The aliquot equilibration model is not well suited to investigate the deposition and remobilization processes of U during fluid-rock interaction, because many reactions take place at different times and locations. The step-flow-through reactor model is the simplest model that can simulate progressive alteration as a function of increasing fluid : rock (F/R) ratio. In this model, the rock is laid out as a one-dimensional column divided into a number of compartments labelled "steps" in Figure 2(b). Initially, each step has the same mass and composition. A batch of

Table 3: System composition used in the step-flow reactor model.

	Fluid	Granite	Protoore	Units
H_2O	1	0	0	kg
O_2	0.1	0	0	mol
NaCl	15	0	0	wt.%
Quartz	0	250	0	g
K-Feldspar	0	300	0	g
Albite	0	300	0	g
$KAl_3Si_3O_{12}H_2$	0	50	0	g
$KFe_3Si_3O_{12}H_2$	0	30	0	g
$KMg_3Si_3O_{12}H_2$	0	30	0	g
Fluorite	0	15	0	g
Magnetite	0	10	994	g
Pyrite	0	1	3	g
Chalcopyrite	0	0	3	g
Uraninite	0	0	0.02	g
U_3O_8(s)	0	0.013	0.02	g

fluid (wave) is equilibrated with the first compartment (step 1); minerals are allowed to precipitate and dissolve, changing the composition of the rock and fluid at step 1. The equilibrated fluid is then extracted and allowed to react with the second compartment (step 2) and so on until the fluid exits the rock column. Repeating this process with fresh batches of fluids (waves 2 to N) allows to simulate increasing F/R ratio. Hence, the number of waves represents the integrated effective F/R ratio, whereas the steps at each value of N represent a profile from the fluid source towards fresh rock (i.e., conditions buffered by fluids to conditions buffered by the rock).

In our model, we use an idealized composition for the protoores at Olympic Dam and a granite composition derived from published data of the Roxby Downs Granite (Table 3), which is the direct host for the ore-bearing hematite breccia at the Olympic Dam [36, 45]. The protoores consist of magnetite and contain low-grade U and Cu mineralization. The calculations were conducted at 200°C, 3000 bar. The temperature reflects the lower end of the hematite stage at OD [16, 45] and was selected because of the high uncertainties in the extrapolated logKs for critical U complexes at higher temperatures. Note that variation of pressure has little effect on the results in this temperature range, and test runs show that higher temperatures (to 300°C) are unlikely to change the fundamental results of the simulations.

3. Selection of Thermodynamic Properties for Aqueous U Chloride and Fluoride Complexes, Uraninite, and Coffinite

Thermodynamic calculations were conducted using the HCh package developed by Shvarov and Bastrakov [46]. Properties for minerals and aqueous species are mainly adopted from an updated version of the UNITHERM database [46, 47], and we also included minerals and aqueous species (mainly Cu and Fe complexes) selected by R. Zhong et al. [48] and R. Zhong et al. [49]. In particular, the thermodynamic properties of uranium minerals and aqueous species used for the calculations are listed in the supplementary material (Appendix, Table S1). Some plots were also drawn using Geochemist Workbench v.11 [50], with a customised thermodynamic database consistent with that of HCh. Here, we discuss the sources of properties for important U complexes and minerals. In general, we use the properties of U complexes selected by Bastrakov et al. [30], which are mainly based on the NEA (Nuclear Energy Agency) review of Guillaumont et al. [51]. Noticeable exceptions include uranyl chloride complexes, where we use the new properties obtained recently by Migdisov et al. [52]. We also use the one-term extrapolation method of Gu et al. [53] to propose new T-dependence for uranyl fluoride complexes based on the new knowledge of uranyl chloride complexes and U(VI) chlorides based on the knowledge of U(IV) fluoride complexes. Since the simulations indicated that some uranyl hydroxide complexes may be important as well, we also review the sources and reliability of these complexes.

3.1. U(IV) Aquo Complex. Despite the importance of low-oxidation state U in the nuclear energy industry, there is surprisingly little information about the nature and stability of U(IV) aquo complexes under hydrothermal conditions [30]. As reviewed by Brugger et al. [54], U(IV) forms a spherical cation surrounded by 9-10 water molecules in the first coordination sphere in acidic solutions at room temperature [55–58]. The thermodynamic properties of the U^{4+} aqua ion are taken from Shock et al. [59].

3.2. U(IV) Fluoride Complexes. The U(IV) fluoride complexes UF_n^{4-n} with $n = 1 - 6$ were included in this study.

For the complexes with $n = 1 - 4$, there is relatively good agreement at room temperature. Bastrakov et al. [30] selected the formation constants reported by Guillaumont et al. [51], which are the unweighted average values reported by Grenthe et al. [60], Noren [61], Kakihana and Ishiguro [62], Choppin and Unrein [63], and Sawant et al. [64]. These values are also close to those selected by Grenthe et al. [65]. In the absence of high-temperature data, Bastrakov et al. [30] used the van't Hoff equation to calculate the T-dependence of the complex to 100°C and then the modified Ryzhenko-Bryzgalin (MRB) model [46] to extrapolate these properties to higher temperature and pressure.

The MRB parameters for UF_5^- and UF_6^{2-} are based on the free Gibbs energy of formation at 25–150°C reported by Barsukov and Borisov [66]. This provides a conservative estimate of the stability of high-order U(IV) fluoride complexes compared to the values selected by Guillaumont et al. [51]. The formation constants for the reactions $U_4^+ + 5F^- = UF_5^-$ and $U_4^+ + 6F^- = UF_6^{2-}$ at 25°C are 25.0 and 27.6, respectively, lower than the values calculated by Guillaumont et al. [51] based on the solubility data of Savage and Browne [67], which are 27.73 ± 0.74 for UF_5^- and 29.80 ± 0.7 for UF_6^{2-}.

3.3. U(IV) Chloride Complexes. Hennig et al. [68] observed the complexes $[U(H_2O)_8Cl]^{3+}$, $[U(H_2O)_{6\text{-}7}Cl_2]^{2+}$, and $[U(H_2O)_5Cl_3]^+$ with $[Cl^-]$ increasing from 0 to 9 M at room

Table 4: Parameters of the MRB model for U(IV/VI) aqueous species fitted in the present study.

Species	$pK_{(298)}$	$A_{zz/a}$	$B_{zz/a}$
UCl^{3+}	1.72	1.628	0
UCl_2^{2+}	1.22	3.082	0
UO_2F^+	5.144	0.7	0
$UO_2F_2(aq)$	8.83	2.673	−884.6
UO_2OH^+	8.616	1.045	181.1

temperature in acidic ($pH_{25°C}$ 0.24–1.61) HCl + LiCl solutions via in situ EXAFS spectroscopy. The average number of chloride increased from 1.0 ± 0.2 (Cl_{tot} = 3 M) to 2.3 ± 0.4 (Cl_{tot} = 6 M) and to 2.9 ± 0.5 (Cl_{tot} = 9 M). We use the speciation information from these spectroscopic results as a benchmark to check the available thermodynamic properties for U(IV) chloride complexes.

The theoretical study of Shock et al. [69] uses UCl^{3+}, UCl_2^{2+}, UCl_3^+, and $UCl_4(aq)$, although HKF parameters or property sources are not listed. Shock et al.'s [69] model predicts high stability of U(IV) chloride complexes above 100°C at low pH; for example, UCl_2^{2+} can account for up to 8% dissolved U in the solution with a pH below 2, and UCl_3^+ and $UCl_4(aq)$ dominate above 250°C at pH = 1.

Bastrakov et al. [30] included just UCl^{3+} and UCl_2^{2+} in their model. The temperature dependence of the UCl^{3+} complex was extrapolated using the entropy and enthalpy values selected by Guillaumont et al. [51], and the properties for UCl_2^{2+} were taken from Barsukov and Borisov [66], who report free Gibbs energy of formation from the elements for UCl_2^{2+} at 25–150°C. Fitting to the MRB model provided extrapolation beyond 150°C [30]. However, including UCl_2^{2+} resulted in unrealistically high predicted U concentrations, which led Bastrakov et al. [30] to ignore UCl_2^{2+} for calculations at $T > 200$°C. However, the UCl_2^{2+} clearly needs to be included based on the average ligand number obtained from the study of Hennig et al. [68].

In order to attempt to obtain more realistic estimates for the stability of U(IV) complexes, we take advantage of the fact that U(IV)-F complexation is better constrained by experimental studies, which results in more reliable thermodynamic properties for U(IV)-F aqueous species at room temperature. We used the one-term isocoulombic extrapolation method developed by Gu et al. [53] to extrapolate thermodynamic properties for UCl^{3+} and UCl_2^{2+} to higher temperatures based on the properties of UF^{3+} and UF_2^{2+}. Then we fitted the properties with the OptimC program [70] and estimated new parameters of the MRB model for UCl^{3+} and UCl_2^{2+}. Note that the fitted logK data are based on the theory behind the isocoulombic approach [53] and that the MRB fitting is only a parameterisation of the logK data to be suitable for HCh database format. This is also the case for uranyl fluoride complexes discussed in Section 3.6. The newly fitted MRB parameters are listed in Table 4, and the extrapolated formation constants for UCl^{3+} and UCl_2^{2+} are compared with the extrapolations using Bastrakov et al.'s [30] parameters in Figure 3. The newly extrapolated formation constants (logK) for UCl^{3+} are higher than those of Bastrakov et al. [30], while the logKs of UCl_2^{2+} are lower than those from Bastrakov et al. [30] and Barsukov and Borisov [66].

We calculated the average numbers of chloride ligands using our thermodynamic model for the 3 M and 6 M Cl_{tot} solutions analysed by Hennig et al. [68] to be 0.6 and 0.7, respectively. This indicates that the predicted chlorination numbers in our model are lower than the experimental ones (1.0(2) and 2.3(4)) and that the model will tend to underestimate U concentrations in reduced brines. Although the properties of U(IV) chloride complexes at hydrothermal conditions clearly require more experimental evidence, the in situ XAS study of Hennig et al. [68] shows that UCl_2^{2+} is important in chloride brines and needs to be included in the speciation model. The proposed extrapolation in this study appears to provide realistic estimates of U(IV) solubility in chloride brines.

3.4. Uranyl Oxycation (UO_2^{2+}). Uranium (VI) is present in the form of the uranyl (UO_2^{2+}) ion, which forms a wide range of complexes with inorganic ligands such as hydroxide, halides, carbonate, or sulfate [54]. In the absence of these ligands, the uranyl ion is hydrated by 5 to 6 water molecules, located on an equatorial plane relative to the two axial uranyl oxygens; the hydration number decreases with temperature, to ~4 at 300°C, 250 bar [54]. The thermodynamic properties of UO_2^{2+} used in this study are compiled from Shock et al. [59], with HKF parameters based on regression of the experimental data of Hovey et al. [71] and Grenthe et al. [65]. As reviewed by Shock et al. [69], the predicted U solubility values show good consistency up to 200°C. However, it is difficult to evaluate the reliability of the thermodynamic properties at $T > 200$°C due to the lack of experimental data.

3.5. Uranyl Chloride Complexes. The formation of $UO_2Cl_n^{2-n}$ complexes is described by the following equation:

$$UO_2^{2+} + nCl^- = UO_2Cl_n^{2-n}, \quad (1)$$

The existence of UO_2Cl^+, $UO_2Cl_2(aq)$, and $UO_2Cl_3^-$ has been reported in several studies [68, 72, 73], and the nature and stability of uranyl chloride complexes under hydrothermal conditions were the focus of two recent experimental studies. Dargent et al. [74] reported the existence of $UO_2Cl_n^{2-n}$ ($n = 0 - 5$) in 0.3–12 M LiCl solutions at 21–350°C based on in situ Raman spectroscopy data. They suggest that highly charged uranyl chloride complexes, that is, $UO_2Cl_4^{2-}$ and $UO_2Cl_5^{3-}$, are especially important at high temperature (>250°C). The recent in situ UV-Vis study of Migdisov et al. [52] was unable to confirm this result in relatively dilute (<1.5 M) NaCl solutions; the discrepancy could be due to the highly concentrated nature of LiCl solutions in the Dargent et al. [74] work or to deviations from the Beer-Lambert law caused by the wide range in ionic strengths investigated by Dargent et al. [74] (e.g., [75]).

Bastrakov et al. [30] calculated the logKs for reaction (1) ($n = 1, 2$) at 25, 50, 75, and 100°C using the van't Hoff equation with ΔH_r (enthalpy change of the reaction) and ΔS_r (entropy change of the reaction) at 298.15 K recommended

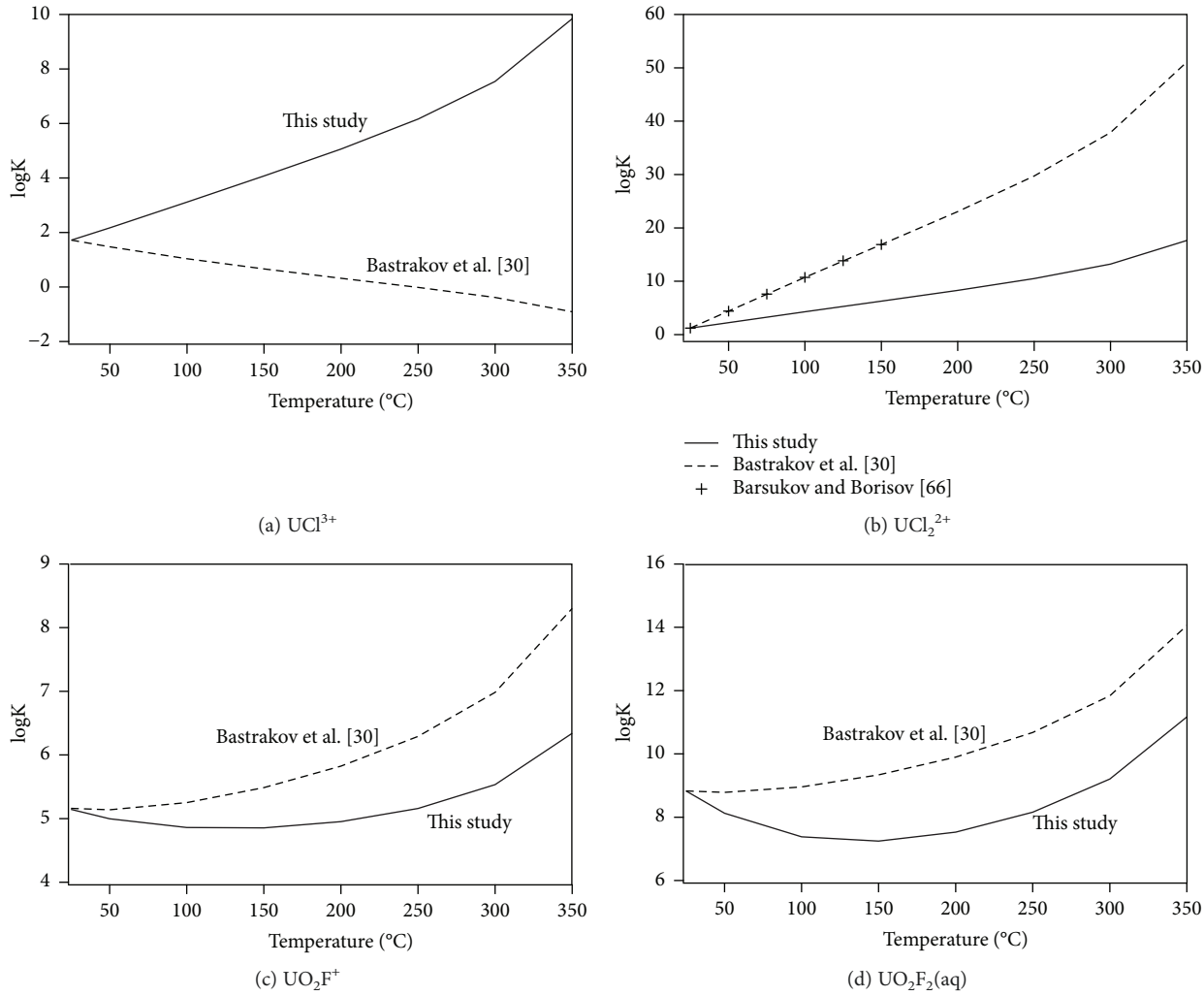

Figure 3: Formation constants (logK) for UCl^{3+}, UCl_2^{2+}, UO_2F^+, and $UO_2F_2(aq)$ extrapolated by this study and the values calculated based on Bastrakov et al.'s [30] estimation.

by NEA [51], and they fitted the calculated logKs to the MRB equation for high-temperature extrapolations.

We compare the logKs of reaction (1) ($n = 1, 2$) from Migdisov et al.'s [52] UV-Vis study and MRB model, and the values calculated using the van't Hoff equation based on NEA [51] and the extrapolated values using Bastrakov et al.'s [30] MRB equation in Figure 4. The formation constants for UO_2Cl^+ from Migdisov et al. [52] show good agreement with the values calculated from the van't Hoff equation and Bastrakov et al.'s [30] MRB at $T < 100$°C. However, above 100°C, the logKs from Migdisov et al. [52] become much higher than the values extrapolated using Bastrakov et al.'s [30] MRB model, indicating higher stability of UO_2Cl^+. For $UO_2Cl_2(aq)$, the logKs from Migdisov et al. [52] are larger than the values calculated using the NEA values [30]. Overall, Migdisov et al.'s [52] experimental study shows higher stability of UO_2Cl^+ and $UO_2Cl_2(aq)$ at elevated T (>100°C) compared with recommendations from NEA [51] used by Bastrakov et al. [30].

In our model, we chose to include only the complexes that were characterised by Migdisov et al. [52], namely, UO_2Cl^+ and $UO_2Cl_2(aq)$. The $UO_2Cl_3^-$ complex was present only in small quantities in Migdisov et al.'s [52] experiments and is therefore not included in our model.

3.6. Uranyl Fluoride Complexes. Guillaumont et al. [51] provided the formation constants of $UO_2F_n^{2-n}$ complexes with $n = 1$ to 4 ($\log \beta_1 = 5.16 \pm 0.06$, $\log \beta_2 = 8.83 \pm 0.08$, $\log \beta_3 = 10.90 \pm 0.10$, and $\log \beta_4 = 11.84 \pm 0.1$) at 25°C and zero ionic strength by reinterpreting the experimental study of Ferri et al. [76]. These values are in good agreement with data reported by Grenthe et al. [65]. There is no experiment for uranyl fluoride complexes at elevated temperature. For UO_2F^+ and $UO_2F_2(aq)$, we extrapolated properties to 350°C using the one-term extrapolation method of Gu et al. [53] based on the properties of UO_2Cl^+ and $UO_2Cl_2(aq)$ reported by Migdisov et al. [52]. The new parameters of MRB model are listed in Table 4.

We compare the formation constants based on our new estimations with the values calculated from Bastrakov et al.'s [30] MRB parameters based on the NEA compilation [51] in Figure 3. The formation constants extrapolated by

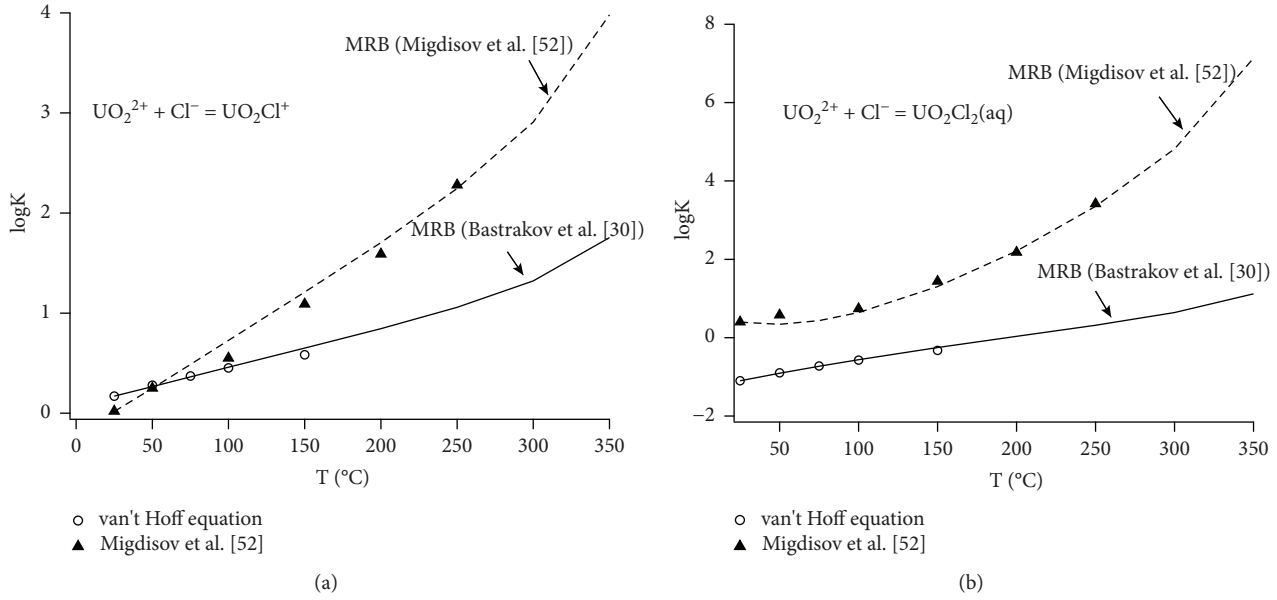

Figure 4: Comparison of values of formation constants of UO_2Cl^+ (reaction (1), $n = 1$) and $UO_2Cl_2(aq)$ (reaction (1), $n = 2$) from Migdisov et al.'s [52] experimental study and their fitted MRB models, values calculated using van't Hoff equation using ΔH_r and ΔS_r recommended by NEA [51] and predicted values from Bastrakov et al.'s [30] MRB model.

our new estimation are lower than those from Bastrakov et al.'s [30] estimation, indicating lower stability of uranyl fluoride species. For $UO_2F_3^-$ and $UO_2F_4^{2-}$, we use the extrapolations proposed by Bastrakov et al. [30]; these two species do not appear to play a significant role in U transport in geochemical systems.

3.7. Uranyl Hydroxide Complexes. Experiments have identified several uranyl hydroxide complexes under acidic conditions. These include the mononuclear species UO_2OH^+, $UO_2(OH)_2(aq)$ (also written as $UO_3(aq)$), $UO_2(OH)_3^-$(HUO^{4-}), and $UO_2(OH)_4^{2-}$(UO_4^{2-}) and polynuclear species such as $(UO_2)_2(OH)_2^{2+}$, $(UO_2)_3(OH)_4^{2+}$, $(UO_2)_3(OH)_5^+$, $(UO_2)_3(OH)_7^-$, and $(UO_2)_4(OH)_7^+$ [30, 77–79]. Under basic conditions, $UO_2(OH)_3^-$ and $UO_2(OH)_4^{2-}$ are important. These features are illustrated in Figure 5, which shows the calculated solubility of metaschoepite and $Na_2U_2O_7{\cdot}H_2O$(cr) together with the measurements of Altmaier et al. [77].

In Bastrakov et al.'s [30] compilation, the thermodynamic properties for UO_2OH^+ and $UO_2(OH)_2(aq)$ are expressed using the MHKF model based on Shock et al. [69] and NEA [51] data, while the properties of the polynuclear species are refitted with MRB equations based on the extrapolations of Plyasunov and Grenthe [80], which use the room-T thermodynamic data compiled by Grenthe et al. [65] and recommended by NEA [51]. Note that due to the effect of entropy, the stability of polynuclear complexes decreases with increasing temperature [81]. The recent experimental studies of Zanonato et al. [79] and Altmaier et al. [77] confirmed the reliability of the thermodynamic data for the polynuclear species recommended by NEA [51]. Therefore, in this study, we use the MRB model fitted by Bastrakov et al. [30] for $(UO_2)_2(OH)_2^{2+}$, $(UO_2)_3(OH)_4^{2+}$, $(UO_2)_3(OH)_5^+$, $(UO_2)_3(OH)_7^-$, and $(UO_2)_4(OH)_7^+$.

Zanonato et al. [79] reported new hydrolysis constants, ΔH_r and ΔS_r for UO_2OH^+ based on a temperature-dependent (10–85°C) potentiometric study. Predictions based on these values (van't Hoff equation to 100°C, fitted to MRB model) are compared to the NEA recommended values and to the extrapolations of Bastrakov et al. [30] in Figure 6(a). We also show the predictions based on the reviews of Nikolaeva [82] and Berto et al. [78]. In general, the new data of Zanonato et al. [79] are close to the NEA-selected values and those of Nikolaeva [82]. Berto et al. [78] underestimates the formation constant and is excluded from this discussion. We selected the new extrapolation based on the latest data of Zanonato et al. [79] for our calculations (Table 4).

For $UO_2(OH)_2(aq)$, Berto et al. [78] and Nikolaeva [82] provide higher formation constants than the NEA review (Figure 6(b)). Since Altmaier et al. [77] showed that the properties for UO_2OH^+ and $UO_2(OH)_2(aq)$ from NEA agree well with their experimental studies, we retain the extrapolation of Bastrakov et al. [30] based on the NEA properties.

3.8. Coffinite, Uraninite, and UO_{2+x} Oxides. Coffinite is one of the most common minerals in sandstone-hosted U deposits. Based on new solubility measurements, Szenknect et al. [83] obtained a free Gibbs energy of formation of coffinite ($\Delta_f G^0_{298K}$) of -1867.6 ± 3.2 kJ mol^{-1}, close to the -1883.6 kJ mol^{-1} recommended by NEA [51]. We used Szenknect et al.'s [83] value in this study. In the absence of experimental data, Bastrakov et al. [30] estimated the heat capacity (C_p) parameters of coffinite by assuming a $\Delta C_p \sim 0$ for the reaction $ZrSiO_4$ (zircon) + UO_2 (uraninite) = $USiO_4$ (coffinite) + ZrO_2(s). We use the same approach, with heat capacity parameters for uraninite, zircon, and ZrO_2(s) taken from Robie and Hemingway [84].

The thermodynamic properties for crystalline U oxides (listed in Appendix, Table S1) are taken from Guillaumont

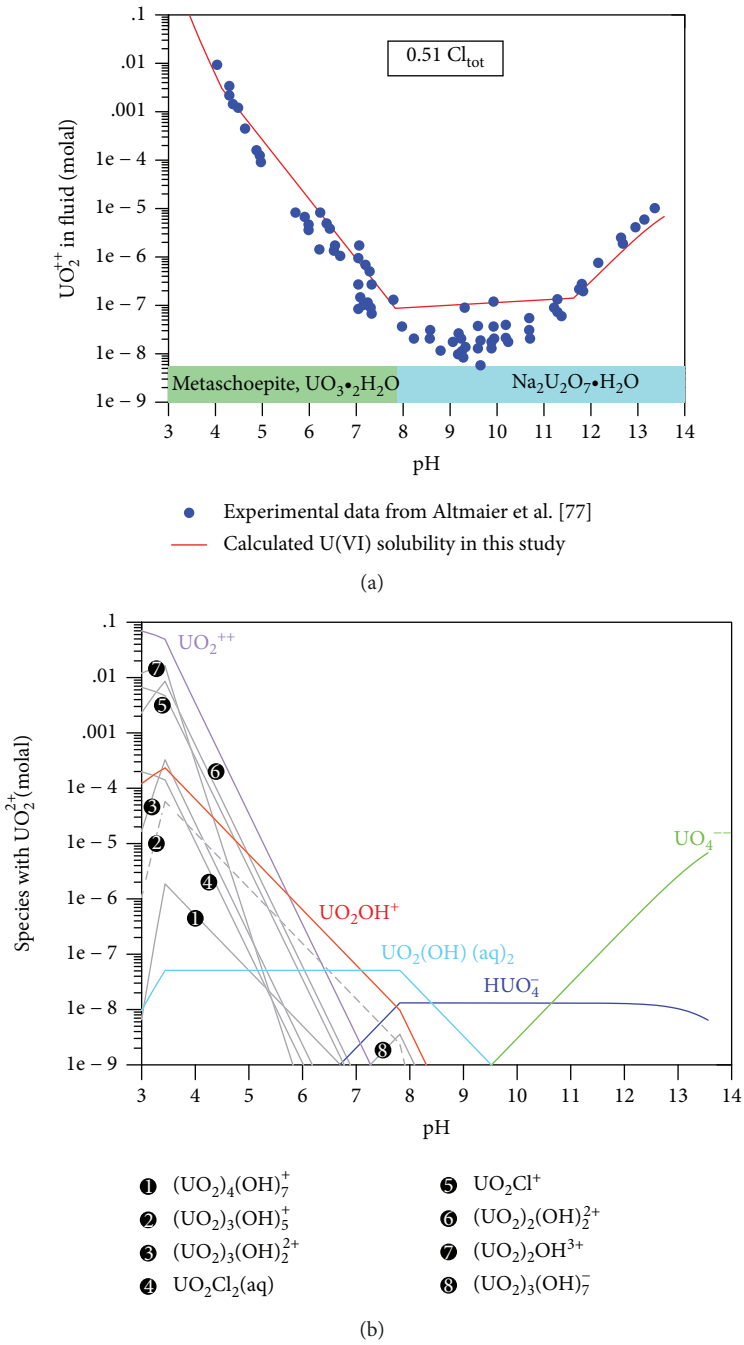

Figure 5: Uranium solubility in 0.51 molal NaCl solutions in equilibrium with metaschoepite or $Na_2U_2O_7{\cdot}H_2O$(cr) at 298.15 K plotted as a function of pH. (a) Uranium solubility calculated with the thermodynamic model used in this study, compared to the solubility data of Altmaier et al. [77]. (b) Distribution of species for the simulation in (a); predominant species are highlighted.

et al. [51]. The C_p parameters are collected from Grenthe et al. [65] and are valid at 250–600 K. These values are close to those reported by Fink [85] so that within the temperature range of our calculations, these values are reliable.

4. Results

4.1. Comparison of U-F and U-Cl Complexation. The effects of Cl and F on U complexation were compared by calculating the speciation of U in solutions containing up to 60 mmol U present as uraninite (Figure 7(a)) or U_3O_8(s) (Figure 7(c)). Figure 7(a) shows the speciation of U(IV) aqueous species in reduced fluids. At $T < 170^{\circ}C$, U(IV)F_4(aq) is the predominant species while U(IV)F_3^{+} and U(IV)F_2^{2+} are less important. Above 170°C, the concentrations of U-F species decrease quickly and U(IV)Cl_2^{2+} becomes predominant at $T > 260^{\circ}C$. As shown in Figure 7(b), the free chloride ion (Cl^{-}) dominates and its concentration remains relatively

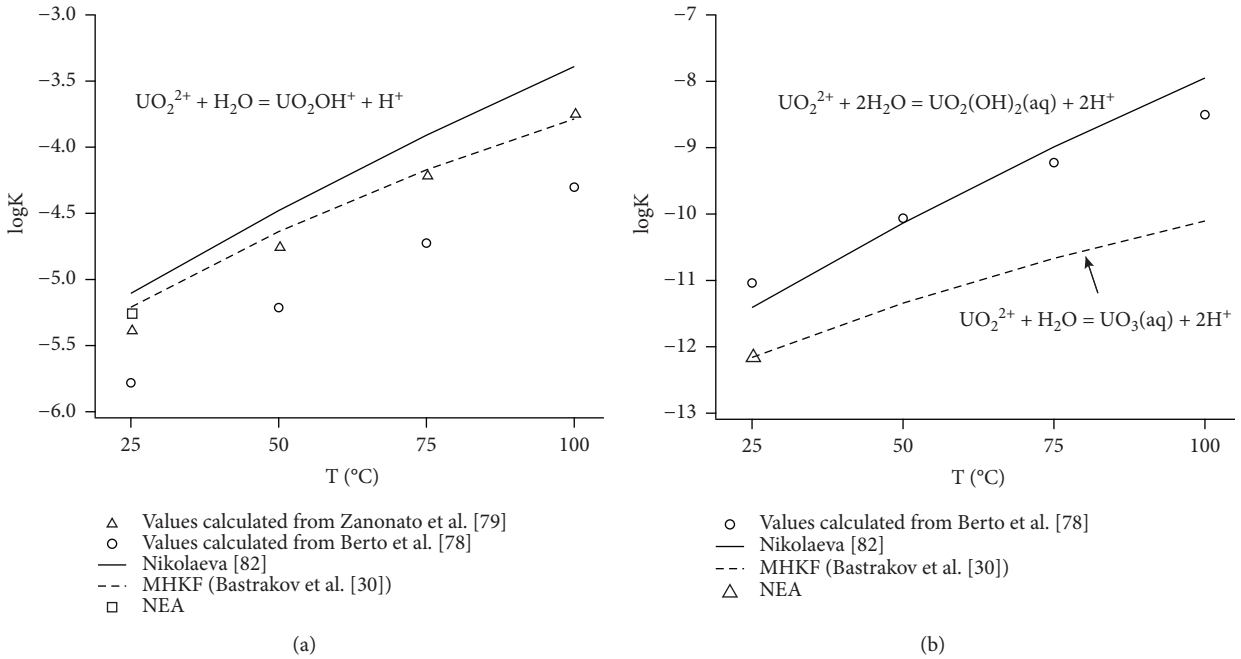

Figure 6: Equilibrium constants for the hydrolysis of UO_2OH^+ and $UO_2(OH)_2(aq)$.

stable with changing temperature, while the concentration of the free fluoride ion (F^-) decreases quickly with increasing temperature at the expense of forming the HF(aq) ion pair. Figure 7(c) shows the solubility of $U_3O_8(s)$ in oxidized fluids, with U(VI) species accounting for most of U in solution. U(VI)-F complexes ($U(VI)O_2F_2(aq)$, $U(VI)O_2F^+$, $U(IV)O_2^{2+}$, and $U(VI)O_2F_3^-$) predominate at $T < \sim 170°C$. With increasing temperature, the stability of U(VI)-F complexes decreases, while $U(VI)O_2Cl^+$ and $U(VI)O_2Cl_2(aq)$ become predominant above 200°C. In contrast to the reduced system (Figure 7(a)), the solubility of $U_3O_8(s)$ remains relatively high with increasing temperatures.

An important feature in both U(IV)- and U(VI)-dominated aqueous systems is that fluoride complexes are stable at low temperatures and chloride complexes at high temperatures. This is further illustrated in a temperature versus log $fO_2(g)$ diagram (Figure 8(a)) and is a result of the strong association of the hydrofluoric acid (HF(aq) ion pair) at elevated temperature compared to HCl(aq). Figure 8(b) shows that low pH favors uranyl chloride over fluoride species.

4.2. Mobilization and Precipitation of Uranium with Increasing Fluid: Rock Ratio in Magnetite-Rich Protoores. Results of the step-flow reactor model are shown in Figures 9 and 10. The dominant feature is the development of a sharp reaction front as a result of the replacement of magnetite in the protoore by hematite. Uranium and Cu concentrations are elevated in the ore at the hematite-magnetite transformation boundary (Figures 9(a) and 9(b)). Similar results were obtained by Bastrakov et al. [45] for Cu and Au enrichment at the hematite-magnetite reaction front and indicated that the oxidizing fluids remobilize redox-sensitive elements and (re-)precipitate them due to the changes in redox and pH conditions at the reaction front. A key result from our model is that fluorine is enriched in the form of fluorite at the reaction front. Fluorite concentrates together with Cu within the hematite zone ahead of the reaction front.

With increasing F/R ratio, the reaction front moves further into the protoore (Figures 9(a) and 9(c) versus Figures 9(b) and 9(d)). This is accompanied by the continuous upgrading of U, Cu, and F near the reaction front (Table 5). The calculated mineralogy of the ores at two F/R ratios is listed in Table 5. For a F/R ratio of 10 : 1, the uraninite concentration at the reaction front reaches 0.6 wt.%, which is 150 times higher than the weakly reacted ores (0.004 wt.% uraninite + $U_3O_8(s)$). At F/R = 15, the uraninite content at the reaction front increased to 0.92 wt.%. The model predicts that UO_2OH^+ is the predominant aqueous species; significant amounts of U are also carried as uranyl fluoride and chloride complexes (Figures 9(c) and 9(d)). Most U precipitated at the reaction front due to the destabilization of uranyl species caused by changes in pH and log fO_2 (Figure 10). The predominant sulfur species are SO_4^{2-} and HSO_4^- at the reaction front, but their concentration drops quickly towards the magnetite side. In contrast, HS^- and $H_2S(aq)$ become more important across the reaction front (Figures 10(a) and 10(b)). The pH decreases at the reaction front and increases dramatically as the fluid equilibrates with the protoore (Figures 10(c) and 10(d)); this is accompanied by a dramatic decrease in the oxygen fugacity of the fluids (Figures 10(e) and 10(f)). The main Cu minerals at/near the reaction front are bornite (±chalcocite) and chalcopyrite, with bornite usually more abundant than chalcopyrite (Table 6). Uranium is predicted to precipitate as uraninite. The simulations show the

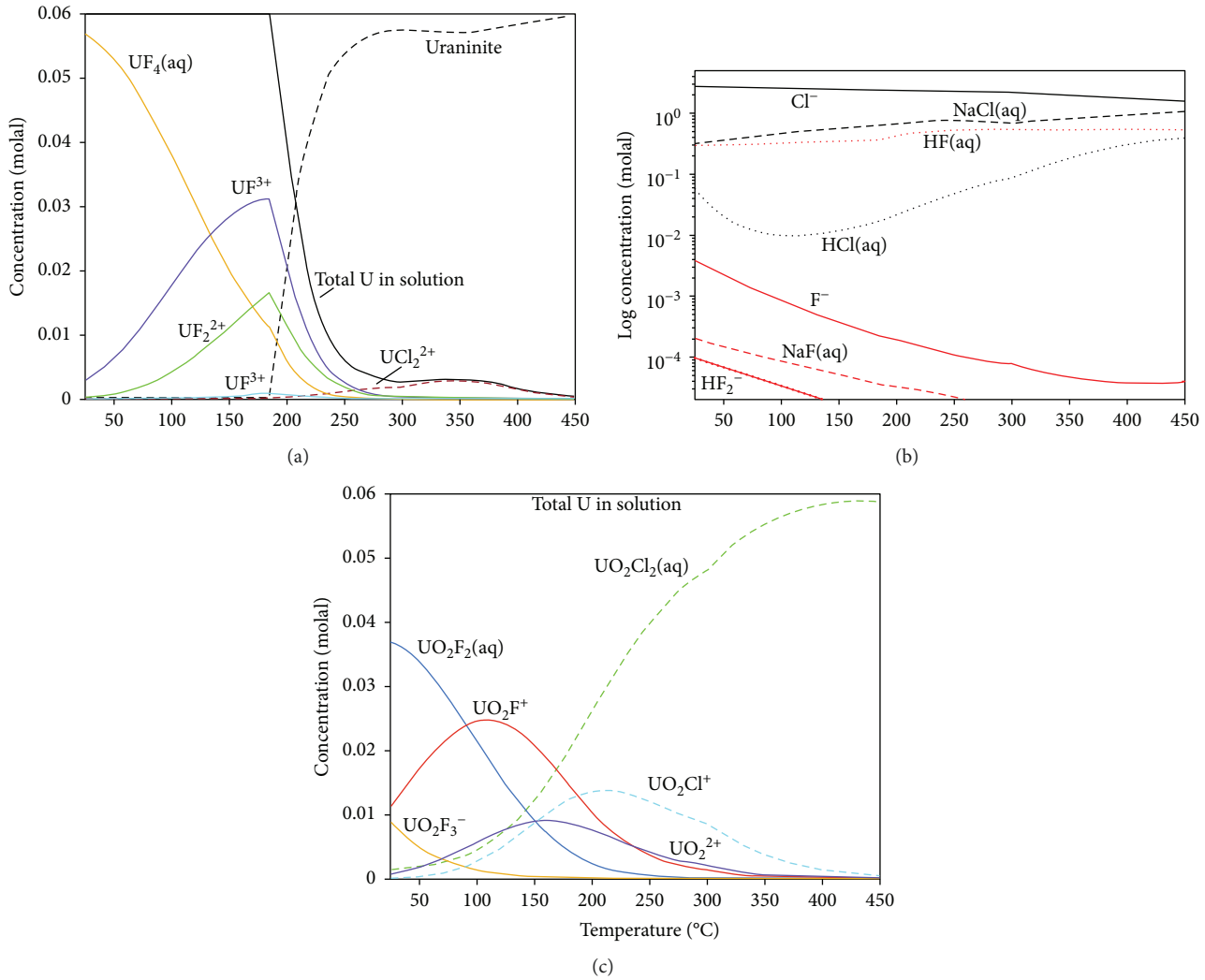

FIGURE 7: Calculation of U solubility and speciation in acidic F^-- and Cl^--bearing solutions at 25–450°C (see Table 2 for system composition). (a) Solubility of UO_2(s) under reduced conditions. Below ~260°C, U(IV)-F complexes predominate over U(IV)-Cl complexes. The overall solubility of UO_2(s) decreases with increasing temperature. (b) Speciation of the chloride and fluoride ligands for the simulation in (a). (c) Solubility of U_3O_8(s). The predominant species below ~170°C are U(VI)O_2F_2(aq) and U(VI)O_2F^+; uranyl chloride complexes become predominant at $T > 170$°C. These calculations were performed in a closed system, with pH and redox self-buffered. The system contains 60 mmolal U, and calculations are isobaric at 3 kbar.

following mineral zonation at the reaction front: chalcopyrite and fluorite are usually enriched towards the magnetite side, while bornite (±chalcocite) and uraninite are towards hematite ore side (Figure 9).

From these results, the predominant reaction is the oxidation of magnetite, which is coupled with the reduction of sulfate (and oxygen) and an increase in pH:

$$8\,\text{magnetite} + SO_4^{2-} + H^+ = 12\,\text{hematite} + HS^-. \quad (2)$$

The oxidized fluids (low reduced S contents) cause the transformation of chalcopyrite into Cu sulfides with higher Cu : S ratios, for example,

$$5\,\text{chalcopyrite} + 6H_2O = \text{bornite} + 6H_2S(aq) + 2\,\text{hematite}. \quad (3)$$

The redox front associated with the reduction of sulfate promotes the reduction of U as well; the deposition of uraninite can be expressed for example as

$$4\left[UO_2^{2+}(OH)\right]^+ + H_2S(aq) = 4\,\text{uraninite} + SO_4^{2-} + 6H^+. \quad (4)$$

4.3. Microenvironments Control the Mineralogy of U. We note that at Olympic Dam, the main U mineralogy in the ores is dictated by microenvironments. Coffinite and brannerite are both more abundant than uraninite (the only U mineral predicted to precipitate in our model). Figure 11 illustrates that (i) coffinite is not predicted to form above ~300°C, since it requires dissolved silica (SiO_2(aq)) concentrations that are oversaturated even with respect to amorphous silica, and (ii) at lower temperatures, coffinite will most likely form in

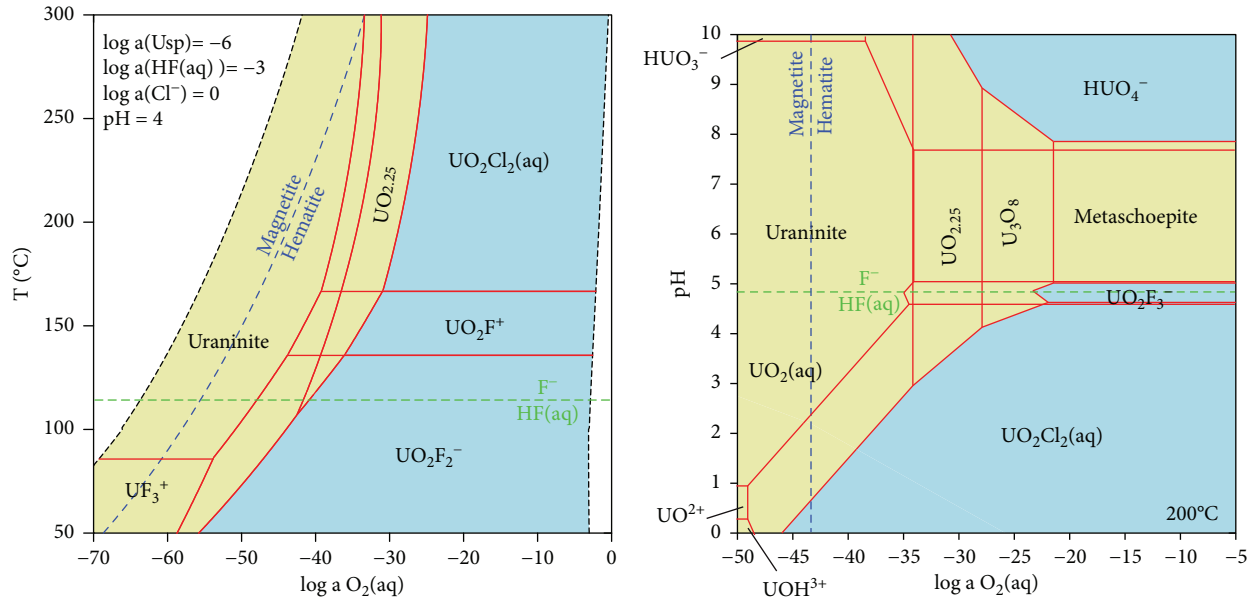

Figure 8: Mineral solubility and speciation for the U-F-Cl system. Minerals are labelled in bold; aqueous predominance fields are shown in the mineral solubility fields with thin red lines. (a) Diagram showing uraninite solubility and U speciation as a function of T (°C) and fO_2. Uraninite is poorly soluble at the phase boundary of magnetite and hematite, and at T < ~170°C, U(VI) fluoride complexes predominate while at T > 170°C, U(VI)O_2Cl_2(aq) is predominant. (b) Uraninite solubility and U speciation as a function of pH and O_2(aq) at 200°C.

microenvironments containing elevated (above quartz solubility) dissolved silica contents [30, 86].

These geochemical constraints are consistent with the textural observations of Macmillan et al. [38]. Brannerite similarly appears to be a late mineral, forming at least in part via interaction of U-bearing fluids with preexisting Ti minerals [38]. Hence, precipitation of coffinite and brannerite versus uraninite are controlled by temperature and by the presence of suitable microenvironments [87]. Our equilibrium model does not account for these microenvironments, but the results would be very similar if coffinite/brannerite were to precipitate rather than uraninite.

5. Discussion

5.1. Fluorite Enrichment with Cu-U Mineralization. A correlation between U and F enrichment has been found in the OD ores [15, 36, 38]. The U-F concentrations for Cu-unmineralized (Cu < 300 ppm), weakly mineralized (Cu = 300–1000 ppm), moderately mineralized (Cu = 1000–3000 ppm), and mineralized OD samples (Cu ≥ 3000 ppm) are plotted in Figure 12. Independently from Cu grade, U concentrations are generally positively correlated with F content, except for ores containing >60 wt.% hematite where fluorite concentrations drop down but U_3O_8 concentrations maintain an upward trend, especially for samples containing ≥1000 ppm Cu (Figures 12(c) and 12(d)). Macmillan et al. [15] reported that the highest U grades are often contributed by massive uraninite found in hematite breccia, and these uraninites are closely intergrown with Cu sulfides.

Our calculations show that U and Cu enrichment at the hematite-magnetite reaction front is associated with F enrichment (Figure 9; Table 5). Fluorine concentration in the hematite ores also increases with continuous hydrothermal alteration (Table 5). It is important to note that these enrichments result from interactions with fluids that are not particularly F-rich: the starting composition of fluid in each wave is in equilibrium with granite, and its F content is relatively low (F = ~80 ppm, Cl : F = ~1800) compared to natural F-rich fluids that can contain in excess of 300 ppm F (magmatic-derived fluids at the Capitan Pluton [34, 35]). In the step-flow reactor model, we assume there is no F in the protoores and the granite is the only unit that contributes F (Table 3). Therefore, F in the hematite ores originates from the granite and is transported by the fluids. For each wave of fluid, the F concentration dropped by about 9.5 ppm (12% of the total F in the fluid) at the hematite-magnetite reaction front, indicating that F kept being precipitated at the reaction front (up to 0.09 wt.% for a F/R ratio of 15). In general, the predicted F grades are lower than the observed grades. This reflects the fact that the protoore in our model does not contain F or Ca. Higher F grades would result in the protoore containing Ca in particular.

A typical textural relationship for uraninite, bornite, and chalcocite is illustrated in Figure 13 based on the observations of Macmillan et al. [15]. Bornite and chalcocite are more likely to be precipitated at the same stage while fluorite is overprinted by uraninite, bornite, and chalcocite (Figure 13). The formation of this texture indicates that fluorite formed earlier than uraninite and Cu sulfides; this is consistent with our simulations (Figure 9). The processes to form this bornite-uraninite-fluorite association are further illustrated in Figure 14. According to the model, fluorite precipitates several steps earlier than uraninite and Cu sulfides along

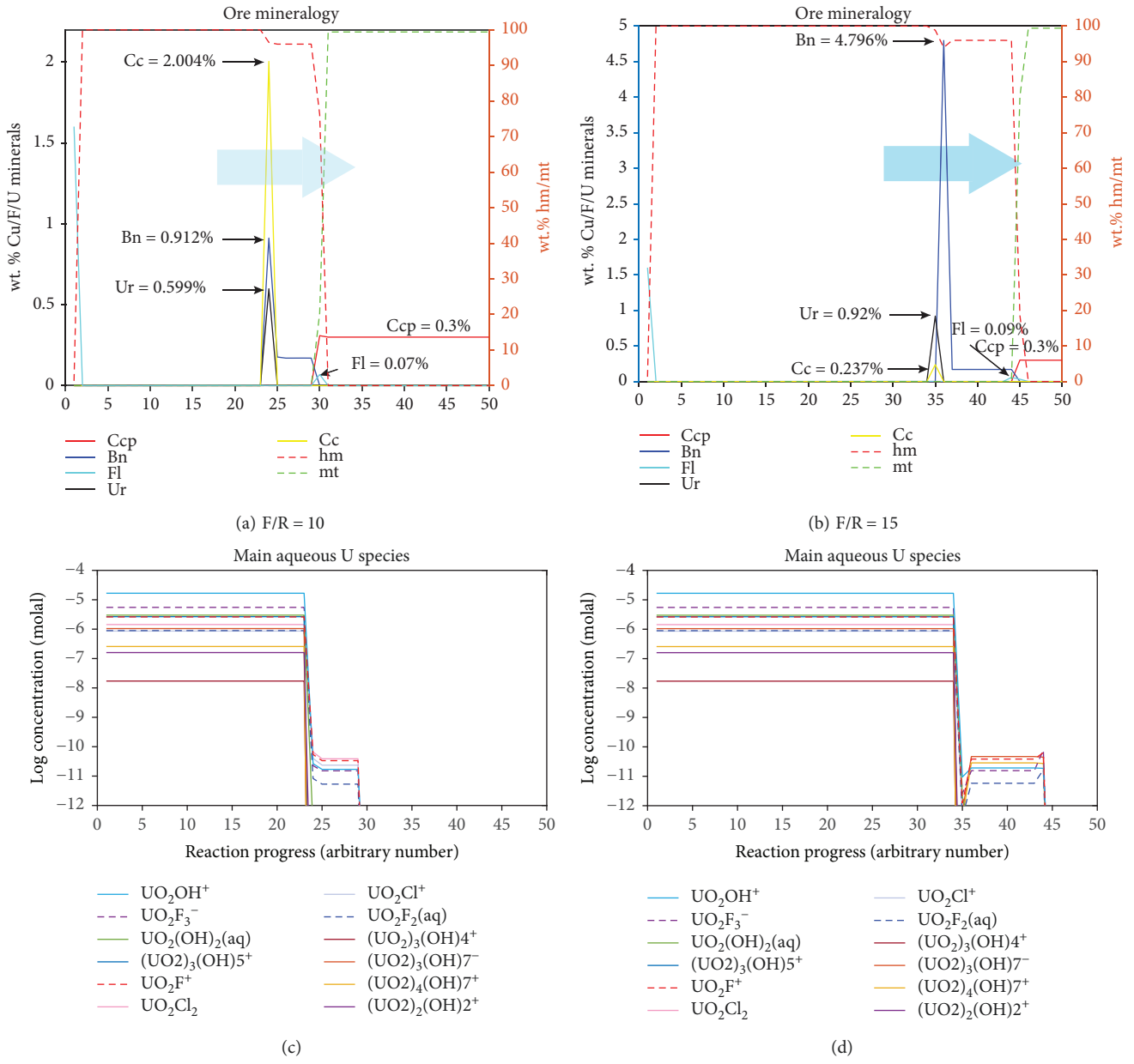

Figure 9: Results of the step-flow-through reactor model. (a-b) Ore mineralogy after 500 waves and 1000 waves, which represent the fluid/rock ratio at 10 : 1 and 20 : 1, respectively. The direction of the reaction front of magnetite replaced by hematite is indicated by the arrows in (a) and (b). Uraninites and Cu sulfides (Ccp and Bn) are precipitated at the reaction front, accompanied by fluorite coprecipitation. Fluorites are enriched in the fully reacted ores (hematite > 95%). Zonation is found at the reaction front, with chalcopyrite and fluorite enriched near the magnetite side and bornite (±chalcocite) and uraninite enriched at the hematite side. (c-d) Main aqueous U species.

the flow direction of fluids. This results in the local zonation from fluorite to uraninite and Cu sulfides upon increasing F/R ratio, as early formed fluorite is overprinted by the later formed uraninite – bornite ± chalcocite assemblage with the influx of new fluids. Hence, the F-U base metal association in this case does not reflect an active role of F as a transporting and/or precipitating ligand but rather results from conditions at the reaction front affecting F (via pH change), U, and Cu (pH and redox changes).

Therefore, the association of F and U-Cu enrichment may simply be formed by the coprecipitation of fluorite due to the similar local physical-chemical traps rather than the breakdown of U-F complexes, but it does not reflect the F-rich nature of the ore-bearing fluids, since the calculated F concentration in fluids indicates only low-F fluids, and the predominant U species is a uranyl hydroxyl complexes (UO_2OH^+) (Figures 9(c) and 9(d)), with contributions from chloride and fluoride complexes.

5.2. Uranium Transport in Cl-F-Bearing Fluids. A popular explanation of the F enrichment in U mineralization is that fluoride helps extract and mobilize U by forming stable U(IV/VI) fluoride complexes [2, 25]. However, our calculations show that fluoride may contribute to considerable U

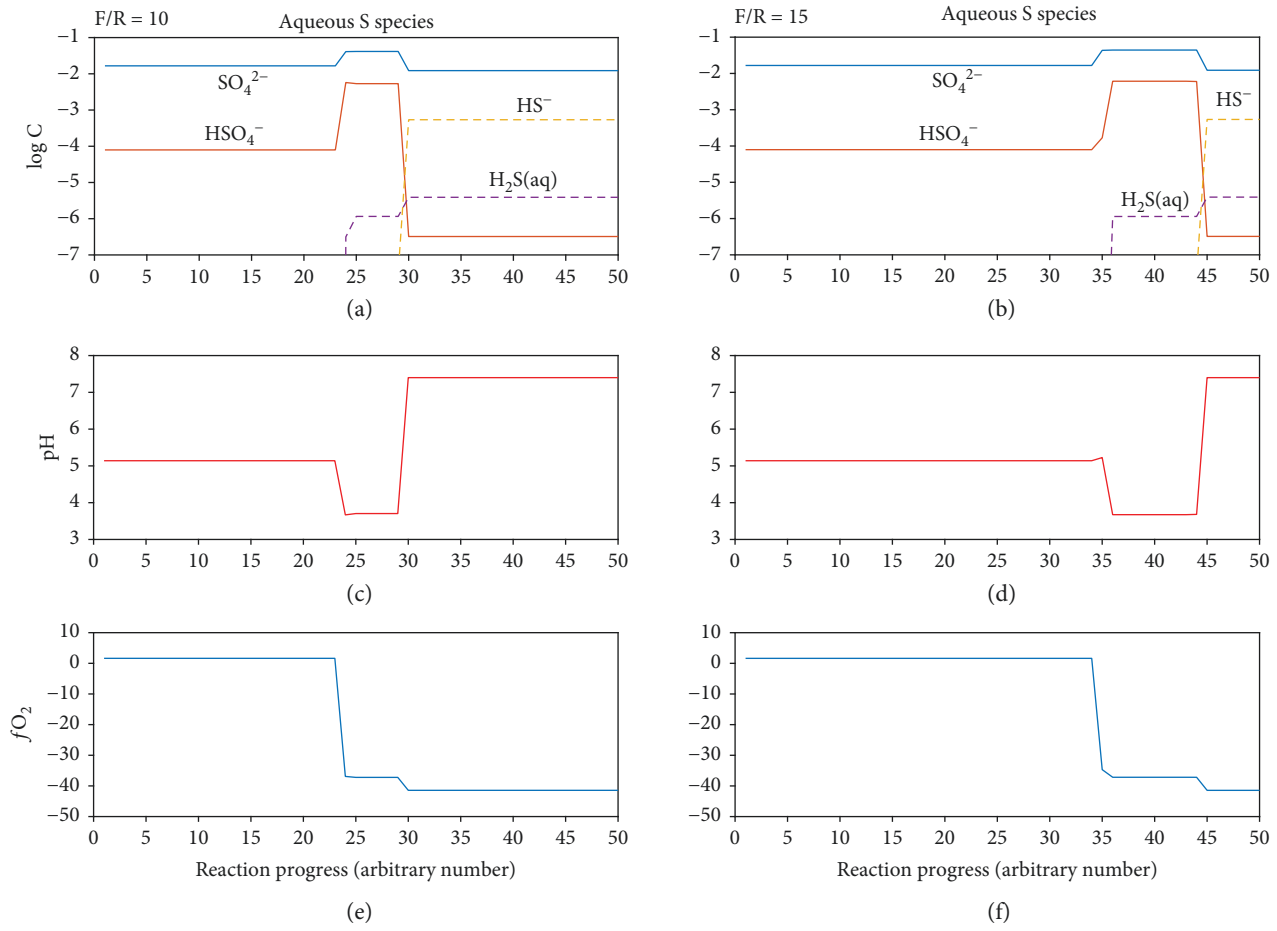

Figure 10: Main sulfur species, pH, and fO_2 in the solution for results from the step-flow-through reactor model at F/R = 10 (a, c, e) and 15 (b, d, f).

Table 5: Ore mineralogy after different waves.

Steps	Description	Mineralogy in wt.%, gold in ppm						
		Uraninite	Fluorite	Chalcopyrite	Chalcocite	Bornite	Hematite	Magnetite
F/R = 10	*Wave 500*							
Step 13	Fully reacted	0	0.0008	0	0	0	99.990	0
Step 24	Reaction front	0.599	0	0	2.004	0.912	96.474	0
Step 30	Reaction front	0.037	0.069	0.309	0	0	76.233	20.379
Step 35	Weakly reacted	0	0	0.300	0	0	0	99.399
F/R = 15	*Wave 750*							
Step 27	Fully reacted	0	0.0017	0	0	0	99.988	0
Step 35	Reaction front	0.920	0.002	0	0.237	3.456	98.830	0
Step 36	Reaction front	0.000	0.000	0	0	4.796	93.957	0
Step 44	Reaction front	0	0.057	0	0	0	95.927	0
Step 45	Reaction front	0	0.033	0.302	0	0	18.555	80.154

aqueous complexation only at relatively low temperature (50–200°C) while at elevated temperature (>200°C), the relative stability of U(IV/VI)-F complexes drops dramatically and U(IV/VI)-Cl complexes become more important in fluids (Figures 7 and 8). Uranyl hydroxide complexes also appear to be important even slightly acidic pH associated with silicate-buffered fluids; our simulations suggest that a mixture of hydroxide, chloride, and fluoride complexes transported U at OD (Figures 9 and 10).

As a hard ligand, fluoride forms strong complexes with cations such as Fe^{3+}, $U(VI)O_2^{2+}$, and REE^{3+}, which makes it a promising ligand for transporting these metals

Table 6: Maximum U, Cu, and F at reaction front.

Wave number	F/R ratio	Maximum U, F, and Cu content at reaction front (g/kg)			Maximum contents of Cu sulfides (g/kg)			Main Cu and U phases in protoore (g/kg)		
		Uraninite	Cu	Fluorite	Chalcopyrite	Bornite	Chalcocite	Chalcopyrite	Uraninite	U_3O_8
100	2	1.20	2.95	0.16	3.09	7.62	0.00	3.00	0.20	0.20
300	6	3.60	7.20	0.47	3.03	21.09	0.00			
500	10	5.99	11.42	0.69	3.09	9.12	20.04			
750	15	9.20	17.28	0.90	3.02	49.96	2.37			

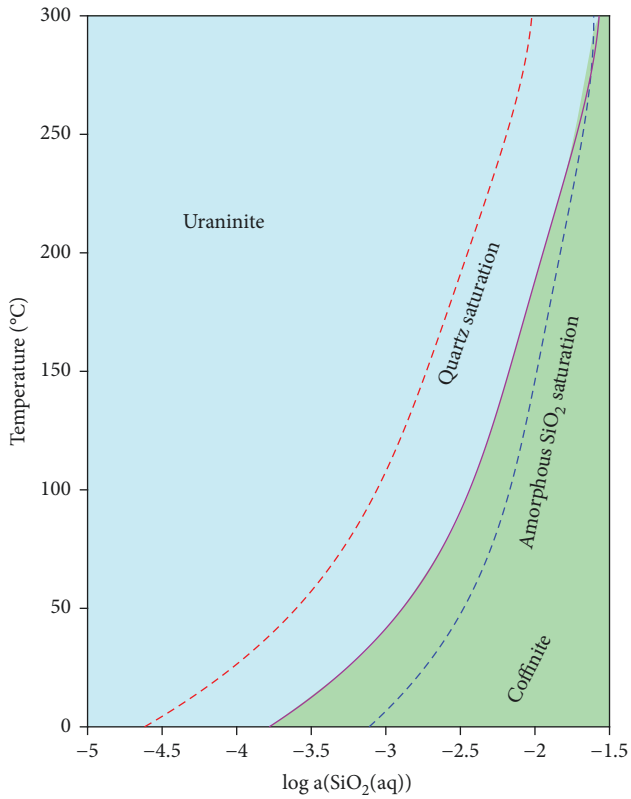

Figure 11: Stability of coffinite versus uraninite as a function of silica activity and temperature compared to the solubility of quartz and amorphous silica.

[2, 33, 88–90]. Consequently, it has long been proposed that F may play a key role for U transport in hydrothermal fluids [2, 25]. Comparing F and Cl, our calculations show that the fluoride complexes of both U(IV) and U(VI) dominate in fluids only at relatively low temperatures (<~200°C). At elevated temperatures (>200°C), U-F complexation is not important. When T is above 200°C, uranyl chloride complexes dominate in acidic oxidized fluids (Figures 7 and 8). As illustrated in Figure 15, U(IV/VI) fluoride complexes are much stronger than the corresponding chloride complexes; the difference in formation constants decreases with increasing temperature but remains significant at 300°C. The increasing importance of chloride versus fluoride complexes hence reflects the stability of the HF(aq) ion pair at high temperature, which competes with the formation of fluoride complexes. Another important factor is that the availability of the fluoride ion in ore fluids is very much limited by extremely low solubility of many fluoride minerals. For example, the solubility of fluorite (CaF_2) is very low ($K_{sp} = 6.6 \times 10^{-8}$ at 200°C), but $CaCl_2$ is very soluble, thus causing the high Cl : F ratio in the fluid. In summary, the transport of U by fluoride may only be of significance in fluids with $T < 200$°C while at elevated temperature, U-F complexes are not stable and contribute little to U transport.

5.3. Remobilization and Upgrading of Uranium by Hydrothermal Fluids. At OD, large-scale hydrothermal activity was responsible for ore formation, and the hydrothermal history of the deposit was complex and protracted [36, 39, 91–93]. As discussed before, our calculations show that U is highly enriched at the magnetite-hematite transformation front (Figure 9). The relative enrichment of U depends on the F/R ratio. According to our calculations, the major U and Cu minerals at the reaction front are uraninite, chalcopyrite, bornite, and chalcocite (Table 5; Figure 9). The relative enrichment of U compared to protoore ($U_{\text{reaction front}}/U_{\text{protoore}}$) is 150 at F/R = 10 and 225 at F/R = 15. Similarly, the Cu contents increase rapidly with increasing F/R, resulting in a zoning of chalcopyrite-bornite (±chalcocite) around the reaction front (Figure 9). In detail, the model predicts that bornite (±chalcocite) is usually accompanied by uraninite enrichment, while chalcopyrite is accompanied by fluorite enrichment. Li et al. [94] demonstrated experimentally that reactions among sulfide minerals create microenvironments that result in efficient scavenging of U from solution and provide evidence that kinetic factors also favor the enrichment predicted by the equilibrium thermodynamic calculations [95].

Results from the step-flow reactor model are consistent with mineralogical observations from OD. Deposit-scale bornite-chalcopyrite zonation is a well-established feature of the deposit, and the highest Cu mineralization is also found along this boundary [91, 96]. Uraninite is often locally enriched near the chalcopyrite-bornite interface, accompanied by fluorite enrichment [16]. Therefore, continuous alteration by oxidized fluid will cause the local dissolution and reprecipitation of the U-Cu ores, which keeps upgrading the U-Cu grade around the bornite-chalcopyrite interface, at deposit but also at the local scale (Figures 9 and 16).

5.4. Sourcing and Deposition of U by Hydrothermal Fluids. The sourcing processes of U to form deposits have long been

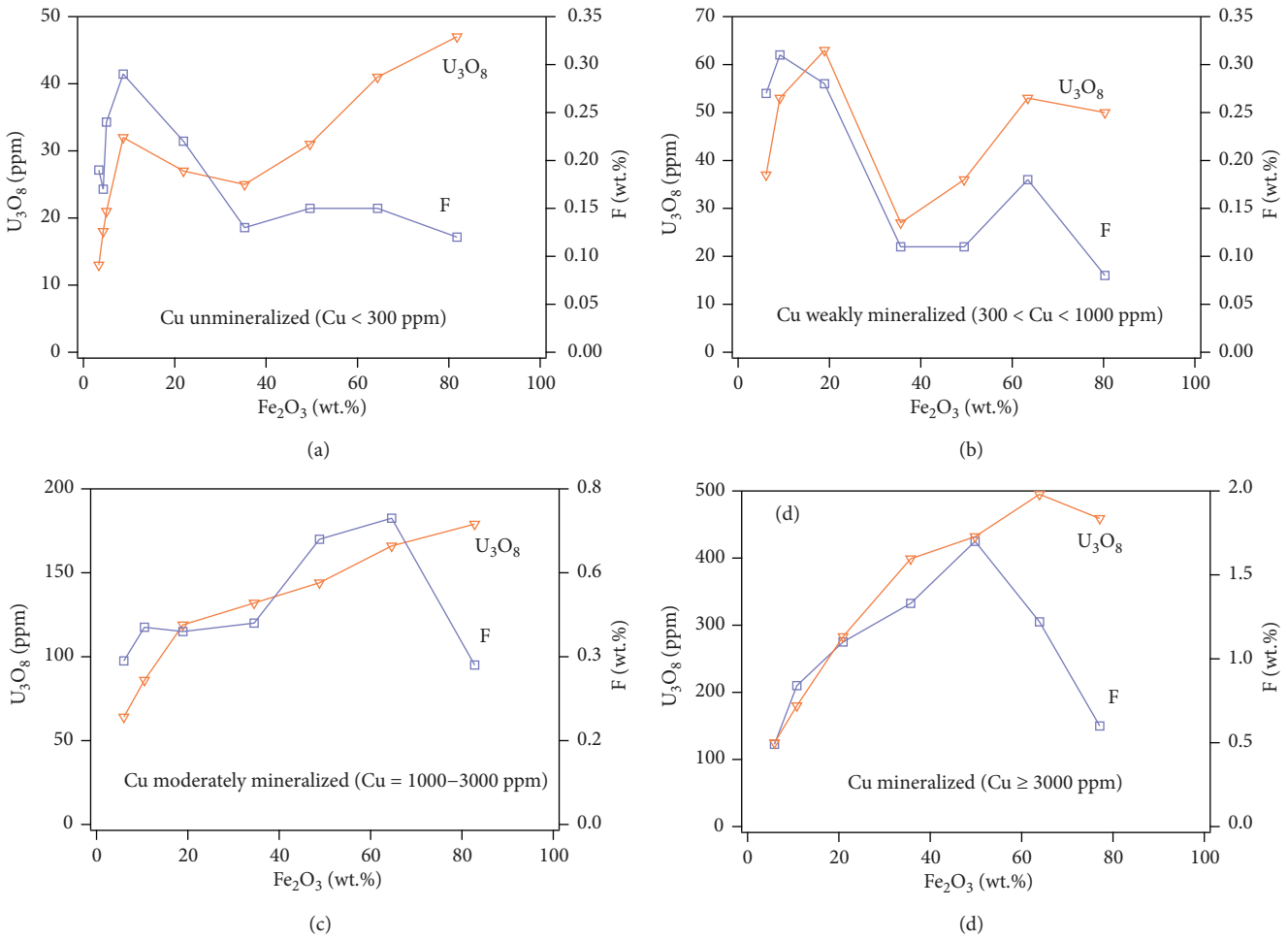

Figure 12: Uranium versus F concentrations in the Olympic Dam ores, as a function of Fe (mainly hematite) content and Cu grades. (a) Cu unmineralized samples (Cu < 300 ppm); (b) Cu weakly mineralized samples (300 < Cu< 1000 ppm); (c) Cu moderately mineralized samples (Cu = 1000–3000 ppm); and (d) high-grade Cu samples (Cu ≥ 3000 ppm). Data from Ehrig et al. [36].

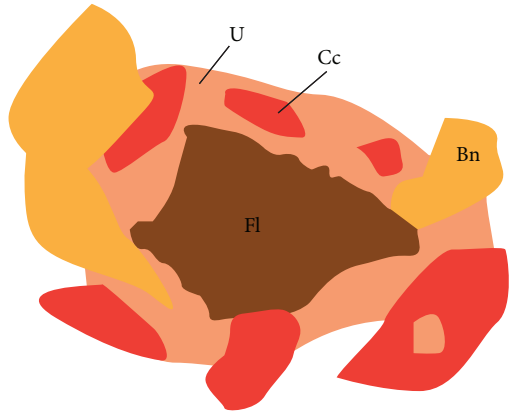

Figure 13: Conceptual textural relationship for uraninite, fluorite, bornite, and chalcocite for ore samples with highest U content at the Olympic Dam. The diagram is abstracted based on Macmillan et al. [15]. U: uraninite; Cc: chalcocite; Bn: bornite; Fl: fluorite.

a controversial topic [2, 39]. The relationship between U solubility, fluid salinity, and pH has been investigated by Richard et al. [32] on natural fluid inclusions and with experiments. Their results show that acidic (pH = 2.5 – 4.5) saline solution caused more U to be dissolved, indicating that chloride and acidic conditions are important for U transport. However, as indicated by our calculations, fluoride is important for U mobilization only at relatively low temperatures (<250°C). Hence, the F-rich nature of Olympic Dam and other U deposits may not necessarily reflect a F-rich nature of the ore-forming fluids but more likely reflects the nature of source rocks or circulation pathways of fluids. This is further supported by the case of the Oak Dam IOCG deposit, where F is absent in the Cu-U ores [97], as a result of the absence of a F-rich igneous unit in the region.

An interesting outcome of the model is the importance of the U(IV) complexes at high temperature under reduced conditions (Figure 7(a)). As discussed in Section 4 and highlighted by Bastrakov et al. [30], confirming these results requires new experimental data, although the room temperature properties are well established. Aside from confirming the stability of U(IV) halide complexes at elevated *T*, experimental studies need to assess the role of mixed halide-hydroxide-aquo complexes at elevated P-T. Ferri et al. [76] found no evidence for such ternary complexes at room

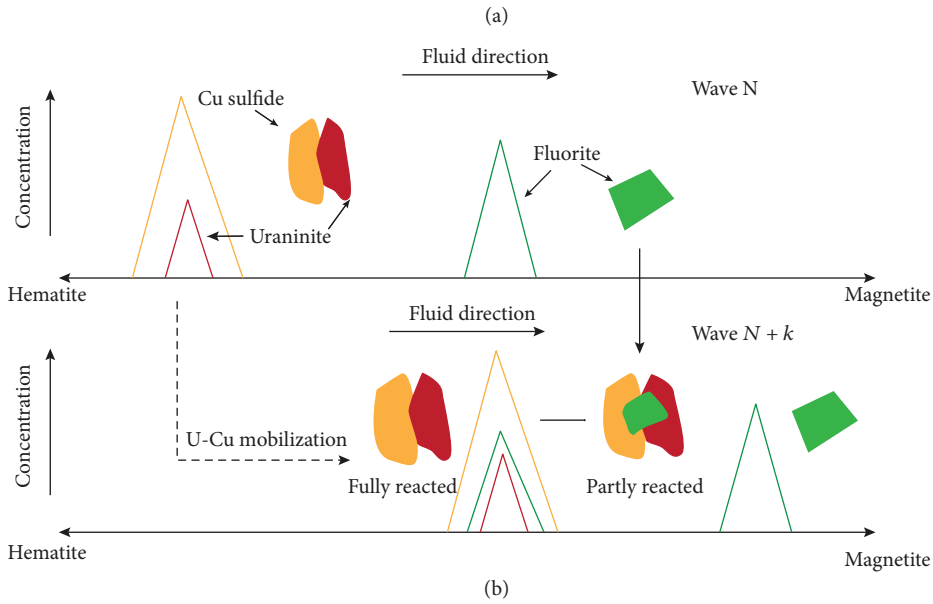

Figure 14: Schematic model for the formation of uraninite-bornite-fluorite intergrowth textures formed at the reaction front according to the step-flow-through reactor calculations. (a) Mineralogy at the reaction front after N waves; fluorites are precipitated a bit earlier than uraninite and Cu sulfides, forming mineralogical zonation; (b) mineralogy at the reaction front after $N + k$ waves; the reaction front is moved towards the fluid penetration direction, causing U-Cu and fluorite mineralization to be moved in the same direction. Due to this movement, early formed fluorite will be overprinted by uraninite and bornite (and/or chalcocite) when fluorites are not fully mobilized.

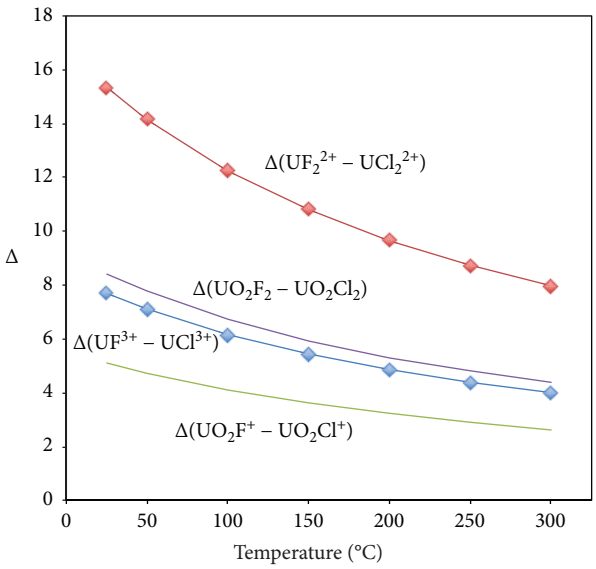

Figure 15: Difference in the logarithm of formation constants for U(IV/VI) fluoride and chloride complexes.

temperature. However, in the case of Zr(IV), Migdisov et al. [98] showed that 8- or 6-coordinated fluoro-aqua complexes predominate at low temperature and tetrahedral hydroxyl-fluoro complexes predominate at high temperature. Such complexes could further increase U(IV) mobility at elevated temperature.

In conclusion, the dissolution and precipitation of U are controlled by T-pH-fO_2, as well as the ligand type (F, Cl, and hydroxide are investigated in this study). The dissolution of uraninite can be described by the following equation:

$$\mathrm{U(IV)O_2(uraninite)} + 0.5\mathrm{O_2} + 2\mathrm{H^+} + x[\mathrm{F, Cl, OH}]^- = \mathrm{U(VI)O_2[F, Cl, OH]}_x^{2-x} + \mathrm{H_2O}. \quad (5)$$

The precipitation of uraninite via reduction of uranyl complexes can proceed with bisulfide (see (4)) or magnetite (Fe^{2+}) as reductants.

Accordingly, increased fO_2 and $[H]^+$ will enhance uraninite dissolution, while a decrease will result in uraninite precipitation (Figure 8(b), U precipitates towards higher pH). Richard et al. [32] postulated that acidic brines with pH between 2.5 and 4.5 are required to maintain high U concentrations in basinal fluids. In addition, the ligand type is also important for U dissolution. By forming strong complexes with $[UO_2]^{2+}$, hard ligands such as F^-, CO_3^{2+}, and SO_4^{2-} may be essential in helping uraninite dissolution. Also note that because of the strong association of F at low temperature, F is likely to be significant as a ligand only at $T < 200^\circ$C.

6. Final Word: the Geochemistry of IOCG Deposits

IOCG deposits are an increasingly important source of economic Fe, Cu, Au, and U since the discovery of the giant Olympic Dam Cu-U-Au deposit in South Australia in 1975 [99]. What constitutes an IOCG deposit has been initially formulated based on the Olympic Dam discovery; that is, IOCG had no formal genetic meaning, and the formal

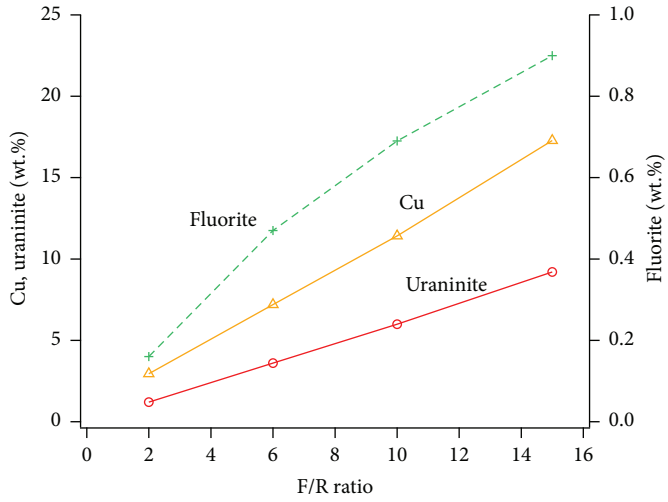

Figure 16: Predicted maximum U, Cu, and F contents with F/R ratio.

definition of IOCG remains a point of controversy to this day. Generally, the attempt of Groves et al. [99] is considered the most authoritative. Our calculations show that as a class, the common geochemical features of IOCG deposits as described by Groves et al. [99] can be related to the two-phase process we modelled, whereby a magnetite-hematite-rich orebody (formed via a number of processes under different tectonic settings) is enriched in Cu ± U,F through a second stage of hydrothermal circulation. Groves et al. [99] outline the following features as being necessary for an IOCG sensu stricto deposit such as Olympic Dam: (i) Cu and Au as economic metals, (ii) hydrothermal features and structural controls (e.g., breccias), (iii) abundant iron oxides (hematite, magnetite), (iv) LREE enrichment and low S sulfides like chalcopyrite and bornite, and (v) lack of abundant syn-sulfide quartz veins. Groves et al. [99] also note that the formation of OD-style IOCGs involved mixing of crustal and meteoric fluids with higher temperature magmatic/metamorphic fluids. In our model, the magmatic stage is not modelled but can correspond to the formation of the magnetite-rich protoore. Furthermore, a temporal (not spatial) relationship with magmatism is a key feature of IOCG deposits according to Groves et al. [99]. This feature is outside the scope of our geochemical model, although it can relate to the heat source driving hydrothermal fluids or to a geodynamic setting conductive to large fluid flow.

Our modelling also indicates that the coenrichment of F and U in IOCG ores most likely reflects the source of the ore-forming fluids and does not reflect an essential role of F in controlling the metal endowment of these deposits.

Conflicts of Interest

The authors declare that they have no conflicts of interest.

Acknowledgments

The authors thank the Australian Synchrotron for the beamtime (XFM beamline) and acknowledge the use of facilities within the Monash Centre for Electron Microscopy. Funding was provided by the Australian Research Council (ARC) grant DP140102765. The authors are grateful to Kathy Ehrig for her comments that helped improve the paper and Edeltraud Macmillan for providing access to the data in Figure 1.

Supplementary Materials

Table S1 lists the uranium minerals and aqueous U species used in the modelling, the equation of state used to extrapolate the thermodynamic properties to high pressure and temperature, and data sources. Table S2 is a digital copy of the thermodynamic data used in the modelling in HCh text export format. For minerals, units are as follows: G(298) [J/mol], S(298) [J·mol^{-1}·K^{-1}], and V(298) [J/bar]. For the modified HKF model of aqueous species, units are as follows: G(298) [cal/mol], H(298) [cal/mol], and S(298) [cal·mol^{-1}·K^{-1}]. *(Supplementary materials)*

References

[1] C. G. Cunningham, J. D. Rasmussen, T. A. Steven et al., "Hydrothermal uranium deposits containing molybdenum and fluorite in the Marysvale volcanic field, west-central Utah," *Mineralium Deposita*, vol. 33, no. 5, pp. 477–494, 1998.

[2] M. V. McGloin, A. G. Tomkins, G. P. Webb et al., "Release of uranium from highly radiogenic zircon through metamictization: the source of orogenic uranium ores," *Geology*, vol. 44, no. 1, pp. 15–18, 2016.

[3] J. McPhie, V. Kamenetsky, S. Allen, K. Ehrig, A. Agangi, and A. Bath, "The fluorine link between a supergiant ore deposit and a silicic large igneous province," *Geology*, vol. 39, no. 11, pp. 1003–1006, 2011.

[4] C. Zhang, Y. Cai, H. Xu, Q. Dong, J. Liu, and R. Hao, "Mechanism of mineralization in the Changjiang uranium ore field, South China: evidence from fluid inclusions, hydrothermal alteration, and H–O isotopes," *Ore Geology Reviews*, vol. 86, pp. 225–253, 2017.

[5] M. Cuney and K. Kyser, *Hydrothermal Uranium Deposits Related to Igneous Rocks, Recent and Not-So-Recent Developments in Uranium Deposits and Implications for Exploration*, Published Jointly by the Mineralogical Association of Canada (MAC) and the Society for Geology Applied to Mineral Deposits (SGA), 2009.

[6] M. W. Hitzman and R. K. Valenta, "Uranium in iron oxide-copper-gold (IOCG) systems," *Economic Geology*, vol. 100, no. 8, pp. 1657–1661, 2006.

[7] R. Z. Hu, X. W. Bi, M. F. Zhou et al., "Uranium metallogenesis in South China and its relationship to crustal extension during the Cretaceous to Tertiary," *Economic Geology*, vol. 103, no. 3, pp. 583–598, 2008.

[8] F. H. B. Tallarico, B. R. Figueiredo, D. I. Groves et al., "Geology and SHRIMP U-Pb geochronology of the Igarape Bahia deposit, Carajas copper-gold belt, Brazil: an Archean (2.57 Ga) example of iron-oxide Cu-Au-(U-REE) mineralization," *Economic Geology*, vol. 100, no. 1, pp. 7–28, 2005.

[9] G. Mark, N. H. S. Oliver, P. J. Willams, R. Valenta, and R. Crookes, "The evolution of the Ernest Henry Fe-oxide-(Cu-Au) hydrothermal system," in *Hydrothermal Iron Oxide Copper-Gold & Related Deposits*, pp. 123–136, A Global Perspective, Adelaide, PGC Publishing, 2000.

[10] G. Mark, N. H. S. Oliver, and P. J. Williams, "Mineralogical and chemical evolution of the Ernest Henry Fe oxide–Cu–Au ore system, Cloncurry district, northwest Queensland, Australia," *Mineralium Deposita*, vol. 40, no. 8, pp. 769–801, 2006.

[11] G. H. C. de Melo, L. V. S. Monteiro, R. P. Xavier et al., "Temporal evolution of the giant Salobo IOCG deposit, Carajás Province (Brazil): constraints from paragenesis of hydrothermal alteration and U-Pb geochronology," *Mineralium Deposita*, vol. 52, no. 5, pp. 709–732, 2017.

[12] W.-T. Chen and M. F. Zhou, "Ages and compositions of primary and secondary allanite from the Lala Fe–Cu deposit, SW China: implications for multiple episodes of hydrothermal events," *Contributions to Mineralogy and Petrology*, vol. 168, no. 2, p. 1043, 2014.

[13] W. T. Chen and M. F. Zhou, "Mineralogical and geochemical constraints on mobilization and mineralization of rare Earth elements in the Lala Fe-Cu-(Mo, Ree) deposit, SW China," *American Journal of Science*, vol. 315, no. 7, pp. 671–711, 2015.

[14] M. W. Hitzman, N. Oreskes, and M. T. Einaudi, "Geological characteristics and tectonic setting of Proterozoic iron oxide (Cu-U-Au-REE) deposits," *Precambrian Research*, vol. 58, no. 1-4, pp. 241–287, 1992.

[15] E. Macmillan, N. J. Cook, K. Ehrig, C. L. Ciobanu, and A. Pring, "Uraninite from the Olympic Dam IOCG-U-Ag deposit: linking textural and compositional variation to temporal evolution," *American Mineralogist*, vol. 101, no. 6, pp. 1295–1320, 2016.

[16] N. Oreskes and M. T. Einaudi, "Origin of hydrothermal fluids at Olympic dam; preliminary results from fluid inclusions and stable isotopes," *Economic Geology*, vol. 87, no. 1, pp. 64–90, 1992.

[17] P. J. Williams, M. Barton, D. Johnson et al., "Iron oxide copper-gold deposits: geology, space-time distribution, and possible modes of origin," *Economic Geology*, vol. 100th Anniversary, pp. 371–405, 2005.

[18] W. T. Chen, M.-F. Zhou, and J.-F. Gao, "Constraints of Sr isotopic compositions of apatite and carbonates on the origin of Fe and Cu mineralizing fluids in the Lala Fe-Cu-(Mo, LREE) deposit, SW China," *Ore Geology Reviews*, vol. 61, pp. 96–106, 2014.

[19] M. Cuney, *Recent and Not-So-Recent Developments in Uranium Deposits and Implications for Exploration*, Mineralogical Association of Canada (MAC) and the Society for Geology Applied to Mineral Deposits (SGA), 2009.

[20] J.-C. Luo, R.-Z. Hu, M. Fayek, X.-W. Bi, S.-H. Shi, and Y. W. Chen, "Newly discovered uranium mineralization at ~2.0 Ma in the Menggongjie granite-hosted uranium deposit, South China," *Journal of Asian Earth Sciences*, vol. 137, pp. 241–249, 2017.

[21] J. T. Nash, *Volcanogenic Uranium Deposits-Geology, Geochemical Processes, and Criteria for Resource Assessment*, U.S. Department of the Interior U.S. Geological Survey, 2010.

[22] A. Chabiron, M. Cuney, and B. Poty, "Possible uranium sources for the largest uranium district associated with volcanism: the Streltsovka caldera (Transbaikalia, Russia)," *Mineralium Deposita*, vol. 38, no. 2, pp. 127–140, 2003.

[23] M. Cuney, "Preliminary results on the petrology and fluid inclusions of the Rossing uraniferous alaskites," *Transactions of the Geological Society of South Africa*, vol. 83, pp. 39–45, 1980.

[24] H. Bohse, J. Rose-Hansen, H. Sørensen, A. Steenfelt, L. Løvborg, and H. Kunzendorf, "On the behaviour of uranium during crystallization of magmas with special emphasis on alkaline magmas, formation of uranium ore deposits," in *International Atomic Energy Agency (IAEA)*, pp. 49–60, Athens, Greece, May 1974.

[25] H. Keppler and P. J. Wyllie, "Partitioning of Cu, Sn, Mo, W, U, and Th between melt and aqueous fluid in the systems haplogranite-H_2O-HCl and haplogranite-H_2O-HF," *Contributions to Mineralogy and Petrology*, vol. 109, no. 2, pp. 139–150, 1991.

[26] C. Peiffert, C. Nguyen-Trung, and M. Cuney, "Uranium in granitic magmas: part 2. Experimental determination of uranium solubility and fluid-melt partition coefficients in the uranium oxide-haplogranite-H_2O-NaX (X = Cl, F) system at 770°C, 2 kbar," *Geochimica et Cosmochimica Acta*, vol. 60, no. 9, pp. 1515–1529, 1996.

[27] M. Cuney, "The extreme diversity of uranium deposits," *Mineralium Deposita*, vol. 44, no. 1, pp. 3–9, 2009.

[28] A. Richard, T. Pettke, M. Cathelineau et al., *Brine-Rock Interaction in the Athabasca Basement (McArthur River U deposit, Canada): Consequences for Fluid Chemistry and Uranium Uptake*, Terra Nova, 2010.

[29] E. Bali, A. Audetat, and H. Keppler, "The mobility of U and Th in subduction zone fluids: an indicator of oxygen fugacity and fluid salinity," *Contributions to Mineralogy and Petrology*, vol. 161, no. 4, pp. 597–613, 2011.

[30] E. Bastrakov, S. Jaireth, and T. Mernagh, "Solubility of uranium in hydrothermal fluids at 25° to 300°C," *Geoscience Australia*, vol. 29, p. 91, 2010.

[31] S. A. Cumberland, G. Douglas, K. Grice, and J. W. Moreau, "Uranium mobility in organic matter-rich sediments: a review of geological and geochemical processes," *Earth-Science Reviews*, vol. 159, pp. 160–185, 2016.

[32] A. Richard, C. Rozsypal, J. Mercadier et al., "Giant uranium deposits formed from exceptionally uranium-rich acidic brines," *Nature Geoscience*, vol. 5, no. 2, pp. 142–146, 2012.

[33] R. G. Pearson, "Hard and soft acids and bases," *Journal of the American Chemical Society*, vol. 85, no. 22, pp. 3533–3539, 1963.

[34] D. A. Banks, B. W. D. Yardley, A. R. Campbell, and K. E. Jarvis, "REE composition of an aqueous magmatic fluid: a fluid inclusion study from the Capitan Pluton, New Mexico, U.S.A.," *Chemical Geology*, vol. 113, no. 3-4, pp. 259–272, 1994.

[35] B. W. D. Yardley, "100th Anniversary special paper: metal concentrations in crustal fluids and their relationship to ore formation," *Economic Geology*, vol. 100, no. 4, pp. 613–632, 2005.

[36] K. Ehrig, J. McPhie, and V. Kamenetsky, *Geology and Mineralogical Zonation of the Olympic Dam Iron Oxide Cu-U-Au-Ag Deposit, South Australia*, Society of Economic Geologists, Inc., 2012.

[37] R. M. Hazen, R. C. Ewing, and D. A. Sverjensky, "Evolution of uranium and thorium minerals," *American Mineralogist*, vol. 94, no. 10, pp. 1293–1311, 2009.

[38] E. Macmillan, N. J. Cook, K. Ehrig, and A. Pring, "Chemical and textural interpretation of late-stage coffinite and brannerite from the Olympic Dam IOCG-Ag-U deposit," *Mineralogical Magazine*, vol. 81, no. 06, pp. 1323–1366, 2017.

[39] M. Kirchenbaur, R. Maas, K. Ehrig et al., "Uranium and Sm isotope studies of the supergiant Olympic Dam Cu–Au–U–Ag deposit, South Australia," *Geochimica et Cosmochimica Acta*, vol. 180, pp. 15–32, 2016.

[40] K. Li, B. Etschmann, N. Rae et al., "Ore petrography using megapixel X-ray imaging: rapid insights into element distribution and mobilization in complex Pt and U-Ge-Cu ores," *Economic Geology*, vol. 111, no. 2, pp. 487–501, 2016.

[41] B. H. P. Billiton, *BHP Annual Report*, 2017, https://www.bhp.com/-/media/documents/investors/annual-reports/2017/bhpannualreport2017.pdf.

[42] M. J. Gregory, A. R. Wilde, and P. A. Jones, "Uranium deposits of the Mount Isa region and their relationship to deformation, metamorphism, and copper deposition," *Economic Geology*, vol. 100, no. 3, pp. 537–546, 2005.

[43] P. A. Polito, T. K. Kyser, and C. Stanley, "The Proterozoic, albitite-hosted, Valhalla uranium deposit, Queensland, Australia: a description of the alteration assemblage associated with uranium mineralisation in diamond drill hole V39," *Mineralium Deposita*, vol. 44, no. 1, pp. 11–40, 2009.

[44] N. H. S. Oliver, J. S. Cleverley, G. Mark et al., "Modeling the role of sodic alteration in the genesis of iron oxide-copper-gold deposits, Eastern Mount Isa Block, Australia," *Economic Geology*, vol. 99, no. 6, pp. 1145–1176, 2004.

[45] E. N. Bastrakov, R. G. Skirrow, and G. J. Davidson, "Fluid evolution and origins of iron oxide cu-au prospects in the Olympic Dam District, Gawler Craton, South Australia," *Economic Geology*, vol. 102, no. 8, pp. 1415–1440, 2007.

[46] Y. Shvarov and E. Bastrakov, *HCh: a Software Package for Geochemical Equilibrium Modelling. User's Guide*, 1999.

[47] Y. V. Shvarov, "HCh: New potentialities for the thermodynamic simulation of geochemical systems offered by windows," *Geochemistry International*, vol. 46, no. 8, pp. 834–839, 2008.

[48] R. Zhong, J. Brugger, Y. Chen, and W. Li, "Contrasting regimes of Cu, Zn and Pb transport in ore-forming hydrothermal fluids," *Chemical Geology*, vol. 395, pp. 154–164, 2015.

[49] R. Zhong, J. Brugger, A. G. Tomkins, Y. Chen, and W. Li, "Fate of gold and base metals during metamorphic devolatilization of a pelite," *Geochimica et Cosmochimica Acta*, vol. 171, pp. 338–352, 2015.

[50] C. M. Bethke, *Geochemical and Biogeochemical Reaction Modeling*, Cambridge University Press, New York, second edition edition, 2008.

[51] R. Guillaumont, T. Fanghanel, V. Neck et al., *Update on the Chemical Thermodynamics of Uranium, Neptunium, Plutonium, Americium and Technetium*, 2003.

[52] A. A. Migdisov, H. Boukhalfa, A. Timofeev, W. Runde, R. Roback, and A. E. Williams-Jones, "A spectroscopic study of uranyl speciation in chloride-bearing solutions at temperatures up to 250°C," *Geochimica et Cosmochimica Acta*, vol. 222, pp. 130–145, 2018.

[53] Y. Gu, C. H. Gammons, and M. S. Bloom, "A one-term extrapolation method for estimating equilibrium constants of aqueous reactions at elevated temperatures," *Geochimica et Cosmochimica Acta*, vol. 58, no. 17, pp. 3545–3560, 1994.

[54] J. Brugger, W. Liu, B. Etschmann, Y. Mei, D. M. Sherman, and D. Testemale, "A review of the coordination chemistry of hydrothermal systems, or do coordination changes make ore deposits?," *Chemical Geology*, vol. 447, pp. 219–253, 2016.

[55] R. J. Frick, A. B. Pribil, T. S. Hofer, B. R. Randolf, A. Bhattacharjee, and B. M. Rode, "Structure and dynamics of the U^{4+} ion in aqueous solution: an ab initio quantum mechanical charge field molecular dynamics study," *Inorganic Chemistry*, vol. 48, no. 9, pp. 3993–4002, 2009.

[56] C. Hennig, K. Schmeide, V. Brendler, H. Moll, S. Tsushima, and A. C. Scheinost, "EXAFS investigation of U (VI), U (IV), and Th (IV) sulfato complexes in aqueous solution," *Inorganic Chemistry*, vol. 46, no. 15, pp. 5882–5892, 2007.

[57] A. Ikeda-Ohno, C. Hennig, S. Tsushima, A. C. Scheinost, G. Bernhard, and T. Yaita, "Speciation and structural study of U(IV) and -(VI) in perchloric and nitric acid solutions," *Inorganic Chemistry*, vol. 48, no. 15, pp. 7201–7210, 2009.

[58] H. Moll, M. A. Denecke, F. Jalilehvand, M. Sandstrom, and I. Grenthe, "Structure of the aqua ions and fluoride complexes of uranium (IV) and thorium (IV) in aqueous solution an EXAFS study," *Inorganic Chemistry*, vol. 38, no. 8, pp. 1795–1799, 1999.

[59] E. L. Shock, D. C. Sassani, M. Willis, and D. A. Sverjensky, "Inorganic species in geologic fluids: correlations among standard molal thermodynamic properties of aqueous ions and hydroxide complexes," *Geochimica et Cosmochimica Acta*, vol. 61, no. 5, pp. 907–950, 1997.

[60] I. Grenthe, J. Varfeldt, H. M. Seip et al., "A potentiometric study of fluoride complexes of uranium (IV) and uranium (VI) using the U(VI)/U(IV) redox couple," *Acta Chemica Scandinavica*, vol. 23, pp. 988–998, 1969.

[61] B. Noren, "A solvent extraction and potentiometric study of fluoride complexes of thorium (IV) and uranium (IV)," *Acta Chemica Scandinavica*, vol. 23, pp. 931–942, 1969.

[62] H. Kakihana and S. I. Ishiguro, "Potentiometric and spectrophotometric studies of fluoride complexes of uranium (IV)," *Bulletin of the Chemical Society of Japan*, vol. 47, no. 7, pp. 1665–1668, 1974.

[63] G. R. Choppin and P. J. Unrein, "Thermodynamic study of actinide fluoride complexation," *4th International Transplutonium Element Symposium, held in Baden-Baden*, 1976, pp. 97–107, North-Holland Publ., Amsterdam, Holland, September 1975.

[64] R. M. Sawant, N. K. Chaudhuri, and S. K. Patil, "Potentiometric studies on aqueous fluoride complexes of actinides: stability-constants of Th(IV)-, U(IV)-, Np(IV)- and Pu(IV)-

fluorides," *Journal of Radioanalytical and Nuclear Chemistry-Articles*, vol. 143, no. 2, pp. 295–306, 1990.

[65] I. Grenthe, J. Fuger, R. Konings et al., *Chemical Thermodynamics of Uranium*, p. 714, 1992.

[66] V. L. Barsukov and M. V. Borisov, "Models of uranium dissolution in natural waters of various compositions," *Geochemistry International*, vol. 41, pp. 38–63, 2003.

[67] A. W. Savage Jr and J. C. Browne, "The solubility of uranium (iv) fluoride in aqueous fluoride solutions," *Journal of the American Chemical Society*, vol. 82, no. 18, pp. 4817–4821, 1960.

[68] C. Hennig, J. Tutschku, A. Rossberg, G. Bernhard, and A. C. Scheinost, "Comparative EXAFS investigation of uranium (VI) and -(IV) aquo chloro complexes in solution using a newly developed spectroelectrochemical cell," *Inorganic Chemistry*, vol. 44, no. 19, pp. 6655–6661, 2005.

[69] E. L. Shock, D. C. Sassani, and H. Betz, "Uranium in geologic fluids: estimates of standard partial molal properties, oxidation potentials, and hydrolysis constants at high temperatures and pressures," *Geochimica et Cosmochimica Acta*, vol. 61, no. 20, pp. 4245–4266, 1997.

[70] Y. Shvarov, "A suite of programs, OptimA, OptimB, OptimC, and OptimS compatible with the Unitherm database, for deriving the thermodynamic properties of aqueous species from solubility, potentiometry and spectroscopy measurements," *Applied Geochemistry*, vol. 55, pp. 17–27, 2015.

[71] J. K. Hovey, C. Nguyen-trung, and P. R. Tremaine, "Thermodynamics of aqueous uranyl ion: apparent and partial molar heat capacities and volumes of aqueous uranyl perchlorate from 10 to 55°C," *Geochimica et Cosmochimica Acta*, vol. 53, no. 7, pp. 1503–1509, 1989.

[72] G. R. Choppin and M. Du, "*f*-Element complexation in brine solutions," *Radiochimica Acta*, vol. 58-59, no. 1, pp. 101–104, 1992.

[73] L. Soderholm, S. Skanthakumar, and R. E. Wilson, "Structural correspondence between uranyl chloride complexes in solution and their stability constants," *Journal of Physical Chemistry A*, vol. 115, no. 19, pp. 4959–4967, 2011.

[74] M. Dargent, J. Dubessy, L. Truche, E. F. Bazarkina, C. Nguyen-Trung, and P. Robert, "Experimental study of uranyl(VI) chloride complex formation in acidic LiCl aqueous solutions under hydrothermal conditions (T = 21 C–350°C, Psat) using Raman spectroscopy," *European Journal of Mineralogy*, vol. 25, no. 5, pp. 765–775, 2013.

[75] J. Brugger, "BeerOz, a set of Matlab routines for the quantitative interpretation of spectrophotometric measurements of metal speciation in solution," *Computers & Geosciences*, vol. 33, no. 2, pp. 248–261, 2007.

[76] D. Ferri, F. Salvatore, E. Vasca et al., "Complex-formation in the U (VI)-OH^--F^- system," *Acta Chemica Scandinavica*, vol. 47, pp. 855–861, 1993.

[77] M. Altmaier, E. Yalçıntaş, X. Gaona et al., "Solubility of U (VI) in chloride solutions. I. The stable oxides/hydroxides in NaCl systems, solubility products, hydrolysis constants and SIT coefficients," *The Journal of Chemical Thermodynamics*, vol. 114, pp. 2–13, 2017.

[78] S. Berto, F. Crea, P. G. Daniele, A. Gianguzza, A. Pettignano, and S. Sammartano, "Advances in the investigation of dioxouranium (VI) complexes of interest for natural fluids," *Coordination Chemistry Reviews*, vol. 256, no. 1-2, pp. 63–81, 2012.

[79] P. Zanonato, P. di Bernardo, A. Bismondo, G. Liu, X. Chen, and L. Rao, "Hydrolysis of uranium (VI) at variable temperatures (10–85°C)," *Journal of the American Chemical Society*, vol. 126, no. 17, pp. 5515–5522, 2004.

[80] A. V. Plyasunov and I. Grenthe, "The temperature dependence of stability constants for the formation of polynuclear cationic complexes," *Geochimica et Cosmochimica Acta*, vol. 58, no. 17, pp. 3561–3582, 1994.

[81] J. Brugger, B. Tooth, B. Etschmann et al., "Structure and thermal stability of bi (III) oxy-clusters in aqueous solutions," *Journal of Solution Chemistry*, vol. 43, no. 2, pp. 314–325, 2014.

[82] N. M. Nikolaeva, *Chemical Equilibria in Aqueous Solutions at High Temperatures*, Izd-vo Nauka Sibirskoe Otd., Novosibirsk (in Russian), 1982.

[83] S. Szenknect, A. Mesbah, T. Cordara et al., "First experimental determination of the solubility constant of coffinite," *Geochimica et Cosmochimica Acta*, vol. 181, pp. 36–53, 2016.

[84] R. Robie and B. Hemingway, "Thermodynamic properties of minerals and related substances at 298.15 K and 1 bar (10^5 Pascals) pressure and higher temperatures," *U.S. Geological Survey Bulletin*, vol. 2131, pp. 461–461, 1995.

[85] J. K. Fink, "Thermophysical properties of uranium dioxide," *Journal of Nuclear Materials*, vol. 279, no. 1, pp. 1–18, 2000.

[86] J. Brugger, N. Long, D. C. McPhail, and I. Plimer, "An active amagmatic hydrothermal system: the Paralana hot springs, Northern Flinders Ranges, South Australia," *Chemical Geology*, vol. 222, no. 1-2, pp. 35–64, 2005.

[87] B. Etschmann, J. Brugger, M. A. Pearce et al., "Grain boundaries as microreactors during reactive fluid flow: experimental dolomitization of a calcite marble," *Contributions to Mineralogy and Petrology*, vol. 168, no. 2, 2014.

[88] J. R. Haas, E. L. Shock, and D. C. Sassani, "Rare earth elements in hydrothermal systems: estimates of standard partial molal thermodynamic properties of aqueous complexes of the rare earth elements at high pressures and temperatures," *Geochimica et Cosmochimica Acta*, vol. 59, no. 21, pp. 4329–4350, 1995.

[89] A. Migdisov, A. E. Williams-Jones, J. Brugger, and F. A. Caporuscio, "Hydrothermal transport, deposition, and fractionation of the REE: experimental data and thermodynamic calculations," *Chemical Geology*, vol. 439, pp. 13–42, 2016.

[90] A. E. Williams-Jones, I. M. Samson, and G. R. Olivo, "The genesis of hydrothermal fluorite-REE deposits in the Gallinas Mountains, New Mexico," *Economic Geology*, vol. 95, no. 2, pp. 327–341, 2000.

[91] D. W. Haynes, K. C. Cross, R. T. Bills, and M. H. Reed, "Olympic dam ore genesis: a fluid-mixing model," *Economic Geology*, vol. 90, no. 2, pp. 281–307, 1995.

[92] S. Meffre, R. R. Large, J. A. Steadman et al., "Multi-stage enrichment processes for large gold-bearing ore deposits," *Ore Geology Reviews*, vol. 76, pp. 268–279, 2016.

[93] P. J. Pollard, *Evidence of Magmatic Fluid and Metal Source for Fe-Oxide Cu-Au Mineralizatoin*, PGC Publishing, Linden Park, 2000.

[94] K. Li, A. Pring, B. Etschmann et al., "Uranium scavenging during mineral replacement reactions," *American Mineralogist*, vol. 100, no. 8-9, pp. 1728–1735, 2015.

[95] A. Altree-Williams, A. Pring, Y. Ngothai, and J. Brugger, "Textural and compositional complexities resulting from coupled dissolution-reprecipitation reactions in geomaterials," *Earth-Science Reviews*, vol. 150, pp. 628–651, 2015.

[96] N. Oreskes and M. T. Einaudi, "Origin of rare earth element-enriched hematite breccias at the Olympic Dam Cu-U-Au-Ag deposit, Roxby Downs, South Australia," *Economic Geology*, vol. 85, no. 1, pp. 1–28, 1990.

[97] G. J. Davidson, H. Paterson, S. Meffre, and R. F. Berry, "Characteristics and origin of the Oak Dam East breccia-hosted, iron oxide Cu-U-(Au) deposit: Olympic Dam Region, Gawler Craton, South Australia," *Economic Geology*, vol. 102, no. 8, pp. 1471–1498, 2007.

[98] A. A. Migdisov, A. E. Williams-Jones, V. van Hinsberg, and S. Salvi, "An experimental study of the solubility of baddeleyite (ZrO_2) in fluoride-bearing solutions at elevated temperature," *Geochimica et Cosmochimica Acta*, vol. 75, no. 23, pp. 7426–7434, 2011.

[99] D. I. Groves, F. P. Bierlein, L. D. Meinert, and M. W. Hitzman, "Iron oxide copper-gold (IOCG) deposits through earth history: implications for origin, lithospheric setting, and distinction from other epigenetic iron oxide deposits," *Economic Geology*, vol. 105, no. 3, pp. 641–654, 2010.

Chapter 4

Trace cerium catalyses formation of giant ore deposits

Yanlu Xing[1], Joël Brugger[1*], Barbara Etschmann[1], Andy Tomkins[1] and Xiya Fang[2]

1. School of Earth, Atmosphere and Environment, Monash University, Clayton, Melbourne, Victoria, Australia
2. Monash Center of Electron Microscopy, Monash University, Clayton, Melbourne, Victoria, Australia

Trace cerium catalyzes formation of giant ore deposits

Yanlu Xing[1*], Joël Brugger[1*], Barbara Etschmann[1], Andy Tomkins[1], Andrew J. Frierdich[1], and Xiya Fang[2]

3. School of Earth, Atmosphere and Environment, Monash University, Clayton, Melbourne, Victoria, Australia
4. Monash Center of Electron Microscopy, Monash University, Clayton, Melbourne, Victoria, Australia

Corresponding author: yanluxxing@gmail.com; joel.brugger@monash.edu

Key words: Magnetite; hematite; mineral replacement; coupled dissolution-reprecipitation reactions; rare earth elements; giant ore deposits.

Abstract

The formation of giant ore deposits reflects the optimal conjunction of otherwise common physical and chemical processes. Positive feedbacks that link mass transfer and ore deposition can be the key difference between an average size deposit and a giant. The supergiant Olympic Dam (South Australia) Iron Oxide Copper-Gold-(uranium, silver) (IOCG) deposit and the giant Bayan Obo (Inner Mongolia, China) REE-Fe deposit are associated with large amounts of magnetite (Fe_3O_4) and hematite (Fe_2O_3). The formation of high-grade ores at Olympic Dam has been linked to overprinting of low-grade magnetite assemblages by hematitization. Similarly, at Bayan Obo, magnetite is commonly found replaced by hematite in the main-stage ores. Here, we show experimentally that the presence of a minor element, cerium (Ce), increases the porosity of hematite formed via fluid-induced replacement of magnetite. The catalytic effect of Ce increases the efficiency of the coupling between magnetite replacement reaction, fluid flow, and element mass transfer, thus enhancing ore formation and ultimately contributing to the size and grade of the ore deposits. At a fundamental level, our work demonstrates that trace elements can be actively involved in the redox cycles of fluid-mediated mineral replacement reactions. In that way, trace elements can have a first order effect on the kinetics, texture, and composition of the products of mineral-fluid reactions.

The Olympic Dam deposit contains the world's largest uranium resource, fifth largest copper, and third largest gold resource [1], and may be the largest, most valuable, supergiant deposit globally [2]. The most notable feature of IOCGs is that voluminous hematite and/or magnetite are associated with enrichments in Cu, Au, ± U, ± Ag. These ores are also enriched in light rare earth elements (LREE); Olympic Dam averages 5,000 ppm ΣREE in hematite-rich ores [3], although these are not currently recovered [4, 5].

IOCG deposits include two major sub-classes: magnetite-rich deposits, such as Kiruna-type magnetite-apatite deposits, and hematite-rich deposits, such as Olympic Dam [4]. Compared to the magnetite-rich endmembers, the hematite-rich deposits usually have elevated Cu-Au-U-REE concentrations and the ores are hosted in breccia [6]. The hydrothermal origin of Cu-Au-U-Ag-(REE) mineralization in IOCG deposits is widely accepted, although the key processes regarding the formation of high-grade ores are still under debate. A two-stage process is favored at Olympic Dam: early-magnetite stage ores formed at high temperatures (>400ºC),

and later flow of lower temperature (<300 ºC), presumably oxidizing fluids resulted in formation of the characteristic hematite-rich Cu-Au-Ag-U ores [7, 8].

One of the key factors controlling metal endowments in IOCG deposits is breccia permeability [7, 9]. Previous studies pointed out that ore grade, brecciation intensity and hematite:magnetite ratio are positively correlated in deposits from the Olympic Dam province [7]. Mineralized samples usually show increased porosity in hematite compared to magnetite [10], suggesting that hematitization introduces porosity.

The replacement of magnetite by hematite is one of the most important reactions associated with the formation of high-grade Cu-Au(±U) ores at Olympic Dam and in the other large deposits of the province (e.g., Oak Dam and Prominent Hill) [7, 8, 11], because of the predominance of iron oxides in these ores. This reaction is often considered to reflect influx of oxidizing fluids. However, pure oxidation of magnetite to form hematite (Reaction [1])) results in an increase in volume (1.66%) [10], which one would expect to decrease breccia porosity and permeability, limit fluid flow, and thus suppress precipitation of ore minerals.

Cerium(Ce) is usually the most enriched REE in iron-oxide ores [1, 3, 4]. Its main form in hydrothermal fluids is Ce(III) [3], but a coupling between the Ce(III/IV) and Fe(II/III) redox cycles is well established at low temperature [12], so we conceived that Ce(III/IV) may affect the magnetite to hematite transformation under hydrothermal conditions. Hence, we performed hydrothermal experiments for the magnetite to hematite transformation in both Ce-bearing and Ce-free (La-, and Nd-bearing) solutions.

Cerium influence on ore texture

Fluid redox is an essential factor controlling the magnetite to hematite transformation [13, 14]. Two different pathways have been recognized for the replacement of magnetite by hematite, a reaction that proceeds via the coupled dissolution-reprecipitation mechanism (ref. [15]):

Oxidative pathway: $2\ Fe_3O_4(mt) + ½\ O_2(aq) = 3\ Fe_2O_3(hm)$; $\Delta V = 1.66\%$ [1]

Non-redox pathway: $Fe_3O_4(mt) + 2\ H^+ = Fe_2O_3(hm) + Fe^{2+}(aq) + H_2O$; $\Delta V = -32.22\%$ [2]

Samples from our oxidative runs (proceeding predominantly via Reaction [1]) show little reaction regardless of the presence of Ce (Table S1, Fig. S1a). The reacted magnetite grains in these experiment products have smooth surfaces, and the pores are usually isolated and small (<1-10 μm) (Fig. S1b). Sample porosity is a necessary feature of coupled dissolution-reprecipitation reactions, as it allows chemical exchange between the reaction front and the bulk fluid. The slow rate of the pure oxidation reaction (Table S1) and smooth grain surfaces

of these experiments (Fig. S1) indicate that simple oxidation via Reaction [1] may block fluid pathways due to the volume increase which reduces the porosity.

Synchrotron X-ray fluorescence mapping combined with μ-XANES imaging shows that Ce(IV) is predominant in the newly formed hematite phase of the oxidative experiments, whereas only minor amounts of Ce(III) are present (Fig. S2). Hence, we conclude that under highly oxidizing conditions, Ce(III) is nearly fully oxidized to Ce(IV), at least partly within the solution itself via reaction with O_2(aq)/H_2O_2(aq).

In contrast, extensive replacement of magnetite by hematite was observed when the reaction was conducted in oxidant-free solutions (i.e., Reaction [2]; Fig. 1a,b; Table S1). Furthermore, under these conditions the textures of the products formed from Ce-doped solutions were different to those reacted in Ce-free solutions (Fig. 1). In Ce-doped solutions, magnetite was replaced by hematite rims, with 5-10 μm wide gaps usually developed at the hematite-magnetite phase boundary (Fig. 1a). Secondary Electron (SE) imaging shows that the magnetite grains have rough surfaces, through formation of 1 to >5 μm hematite crystals (Fig. 2a). For experiments using La- or Nd-doped solutions, hematite in the products usually formed thin lamellae, commonly in close contact with magnetite grains (Fig. 1c); SE images show that hematite crystals are closely stacked on the magnetite surfaces and generally have a homogenous morphology with a narrow size distribution (~5 μm; Fig. 2b).

In order to get more information of the transformation process, we performed Electron Backscattered Diffraction (EBSD) analysis to get orientation and crystal statistics (e.g., single grain shape and size distribution) of hematite and magnetite grains. EBSD data were analysed using TSL OIM software (details in Methods section) and we reconstructed recrystalized hematite grains in the newly formed hematite phase in both sets of samples (Figs. 1b,1d and Fig. 4). The results show that in Ce-doped solutions, hematite grain can generally grow larger than those in La- or Nd-doped solutions. This difference in the size of recrystalized hematite grains indicate that different transformation reaction happened for magnetite to hematite when difference REEs are doped (i.e., Ce, La and Nd).

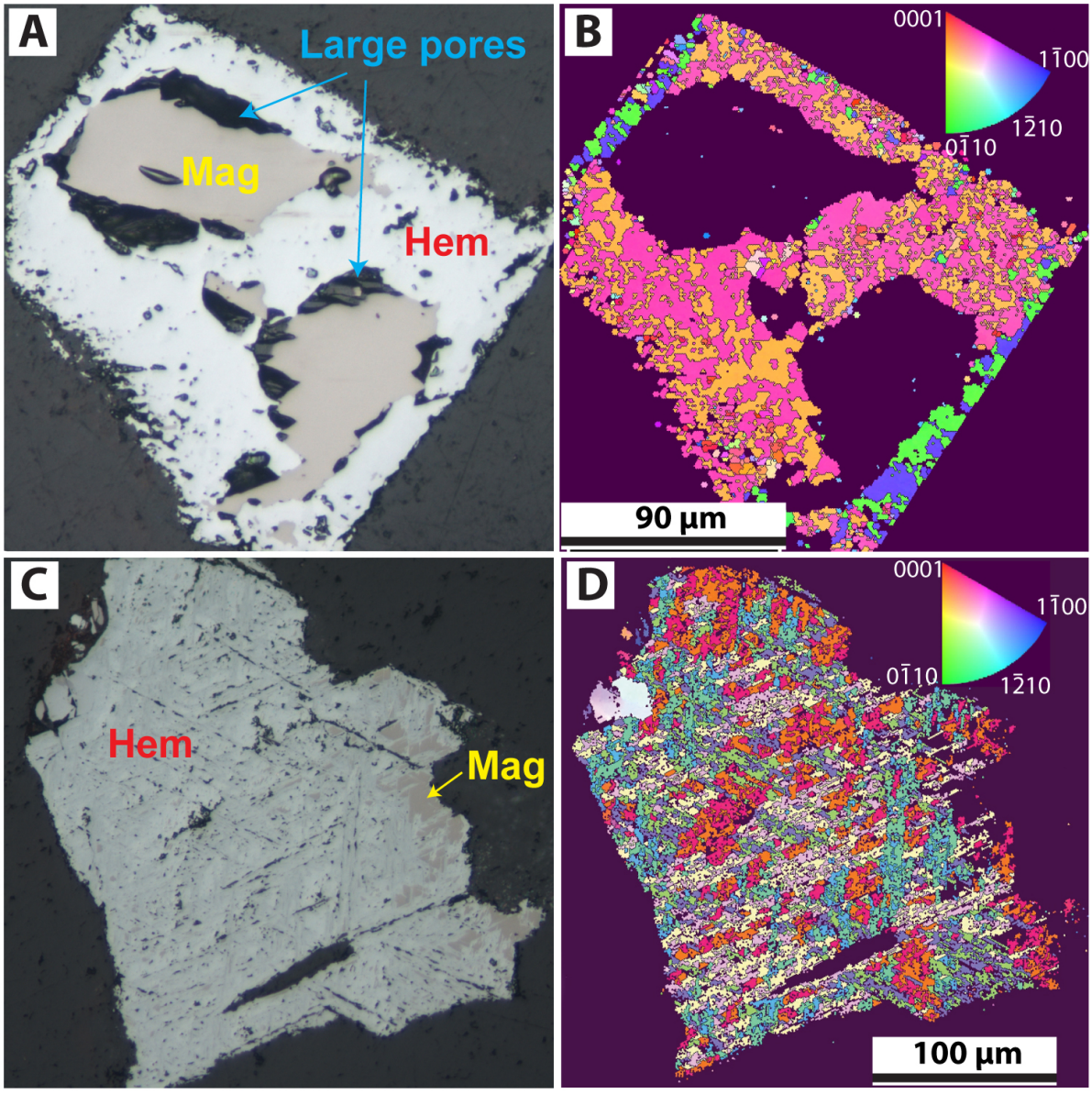

Fig. 1 | Optical reflected light micrographs and EBSD orientation maps showing magnetite replaced by hematite. (a-b) Magnetite reacted in an oxidant-free Ce-bearing solution; (a) hematite replaces magnetite along the rim; gaps develop at the hematite-magnetite phase boundary; large (5-30 µm) pores occur within hematite; (b) EBSD inversed pole figure (IPF) with orientation and reconstructed grain boundary for hematite in the grain illustrated in (a). (c-d) Magnetite reacted in an oxidant-free Nd-bearing solution; (c) hematite replaces magnetite from one side of the parent magnetite grain. Hematite forms lamellae that are in close contact with magnetite, with no visible pores at the boundary. Small (<1-10 µm) pores are present within the hematite domains; (d) EBSD IPF figure for (c), with orientation and reconstructed grain boundary for hematite.

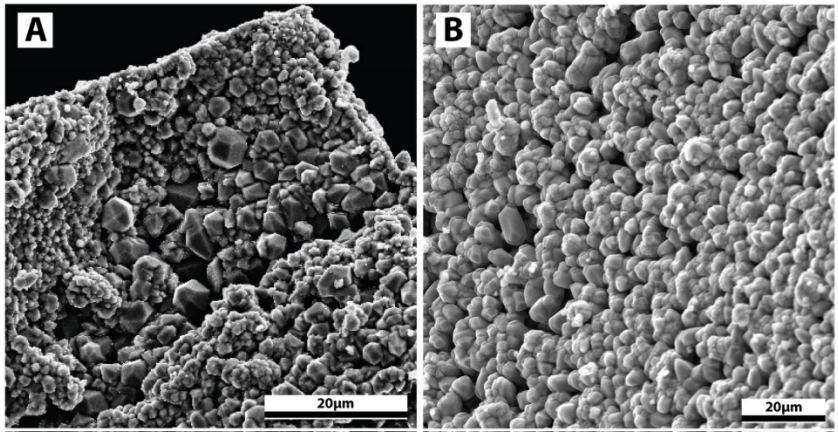

Fig. 2 | SE image of the surface of magnetite grains replaced by hematite, for reactions in oxidant-free conditions and in presence of either (A) Ce(III) and (B) Nd(III) in solution.

Reaction mechanism

Magnetite replacement produced textures typical of interface-coupled dissolution-reprecipitation (ICDR) reaction mechanism [13]. The difference in porosity (size and distribution) and crystal habit of the hematite produced in Ce-bearing versus Ce-free runs indicates that different dissolution-reprecipitation processes operated (e.g., ref. [16]).

The dissolution of magnetite in the oxidant-free experiments can be described by:

Fe_3O_4 (mt) + 8 H^+ = Fe^{2+}(aq) + 2 Fe^{3+}(aq) + 4 H_2O(l), log$K_{200°C}$ = -3.84 [3]

which results in an Fe^{2+}/Fe^{3+} ratio of 0.5 in solution at the reaction front. When Ce^{3+} is present in the solution, the following reaction may occur:

Fe^{3+} + Ce^{3+} + 2 H_2O(l) = CeO_2(cerianite) + Fe^{2+} + 4 H^+, log$K_{200°C}$ = 0.93. [4]

For Reaction [4], log$K$ is 0.93 at 200 ºC. Assuming that the fluid has 200 ppm Ce^{3+} and pH ~4, the fluid will have an equilibrium Fe^{2+}/Fe^{3+} value of 10^{13} at 200 ºC. Therefore, the presence of Ce^{3+} may dramatically increase the Fe^{2+}/Fe^{3+} ratio in the local solution, as well as the solution acidity, promoting local magnetite dissolution.

Hematite precipitation can happen via the following reactions:

$2Fe^{3+}$(aq) + 3 H_2O(l) = Fe_2O_3(hm) + 6 H^+, log$K_{200°C}$ = 8.53 [5]

$2Fe^{2+}$(aq) + $3H_2O$(l) = Fe_2O_3(hm) + 4 H^+ + H_2(g), log$K_{200°C}$ = -12.30 [6]

Reactions [5] and [6] show that hematite solubility increases with increasing pH and under reducing conditions (high Fe(II)/Fe(III) ratio in solution) [17]. These conditions are realized at

the reaction front: both Reactions [5] and [6] increase pH, and an increase in Fe^{2+}/Fe^{3+} results from local Ce^{3+} oxidation (Reaction [4]). Hence the increase in Fe solubility at the reaction front in the presence of Ce^{3+} decreases the hematite nucleation rate.

The presence of Ce(IV) in the hematite product in our experiments was confirmed by XANES imaging (Fig. S2); these micro-spectroscopic results, however, show that only small amounts of Ce(IV) are preserved in the hematite product, with Ce(III)/Ce(IV) ratios >>1. Cerium(IV) is poorly soluble in hydrothermal fluids, precipitating as cerianite-(Ce) (CeO_2). However, cerianite-(Ce) is not reported as a hydrothermal phase in IOCG ores; we suggest that this nano-mineral decomposes to form Ce^{3+} via the following reaction:

$$CeO_2(s) + 3\ H^+ + 0.5\ H_2(g) = 2\ H_2O(l) + Ce^{3+},\ \log K_{200^oC} = 9.49 \qquad [7]$$

This reaction is facilitated by the pH decrease at hematite precipitation sites via Reactions [5] and [6] (Fig. 3), and the locally reducing conditions at the hematite – magnetite interface (e.g., $fH_2(g) = 10^{-3}$ at 200 ºC, P_{sat} for the hematite-magnetite buffer).

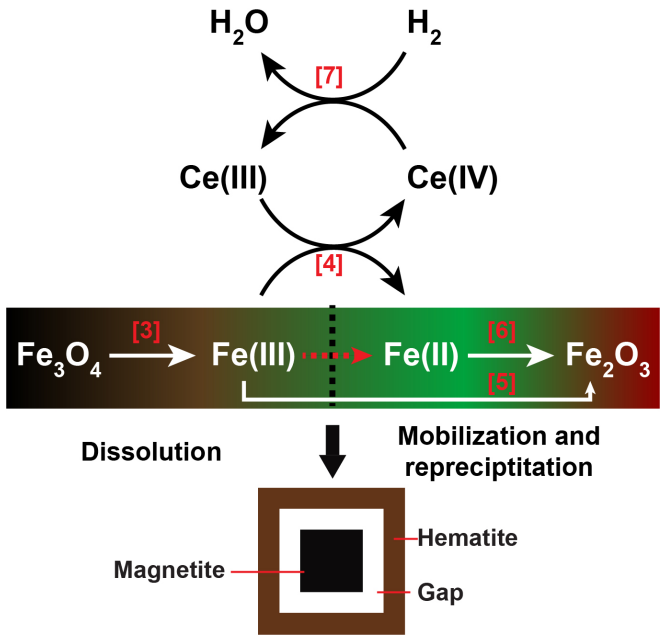

Fig. 3 | Schematic diagram showing Fe(III)-Fe(II) and Ce(III)-Ce(IV) reaction cycles during ICDR processes of magnetite to hematite transformation.

Nature of reaction-induced porosity

Reaction-induced porosity is a necessary feature for mineral replacement reactions proceeding via coupled dissolution-reprecipitation mechanism [18]. This porosity, which is often transient, i.e., not preserved as the system undergoes further fluid-rock interaction or annealing, has recently been argued to be important in ore-forming, metamorphic and metasomatic

environments [19]. The amount of porosity is controlled by relative mineral solubilities, which in turn is controlled by fluid parameters such as pH, Eh, and solution composition [20].

Rather than fine pores distributed throughout the hematite (e.g., Fig. 1c), the oxidant-free Ce-bearing experiments produced coarser porosity located predominantly at the magnetite-hematite phase boundary (Fig. 1a). These are key changes that enhance fluid access to the reaction front, thereby facilitating fluid-mineral interaction. Cerium does this by increasing the Fe^{2+}/Fe^{3+} ratio in the reaction front fluid via Reaction [4], which allows formation of larger hematite crystals with concomitantly larger spaces between crystals by suppressing hematite nucleation. This is confirmed by EBSD data that hematite grew larger in Ce-doped solutions than in Nd-doped solutions (Fig. 4). By comparison, the absence of Ce results in fast hematite nucleation and finer hematite crystals, and more homogeneously distributed smaller pores (Figs. 2 and 4). The closer proximity of magnetite and hematite in this case (Fig. 1c) makes fluid access to the mineral reaction front less efficient.

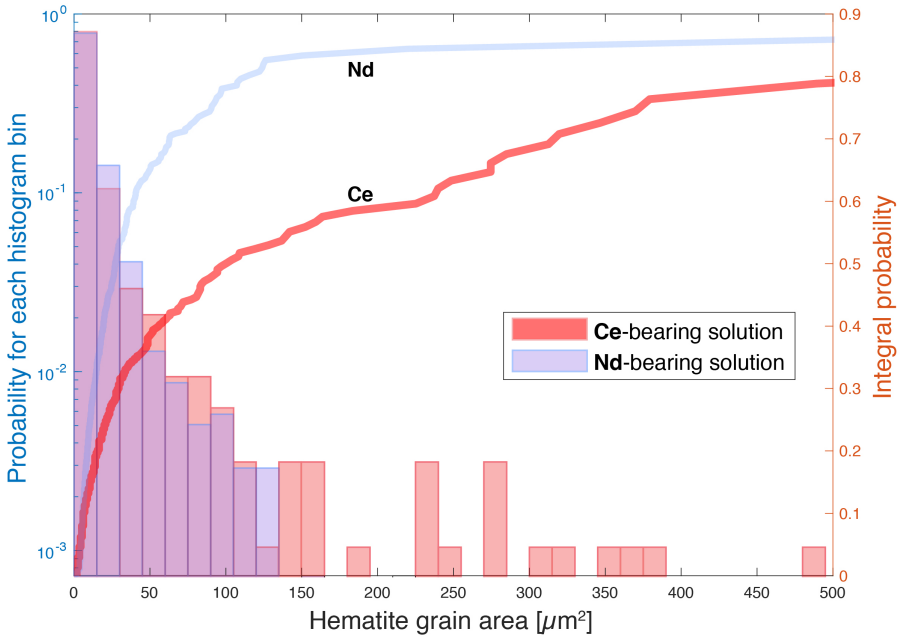

Fig. 4 | Grain size distribution of hematite formed in Ce-bearing and in Nd-bearing solutions from non-oxidative runs. The lines show the integral probability of the hematite grains.

The making of giant ore deposits

Specific positive feedbacks that increase the efficiency of a given mineralization process, but require a set of highly specific conditions to become active, may be important in explaining the size, distribution, and rarity of giant ore deposits. Permeability is a key factor controlling metal endowment in hydrothermal ore deposits. In the case of Olympic Dam, regional faults are the primary control of the formation of breccia complex [7, 9]. The primary brecciation processes introduced the major fluid conduits in the system. However, hydrothermal alteration can moderate the brecciation process by increasing or decreasing porosity. This helps the fluid to penetrate into wall rocks along fluid pathway and form pervasive alteration. Previous studies have linked the F-rich nature of many IOCG deposits to enhanced permeability of IOCG ore bodies because HF(aq) is a highly corrosive acid [21]. However, recent experimental and theoretical data show the amount of F in fluids is strongly limited by mineral solubility, which further limits the aggressive character of these fluids [17, 22].

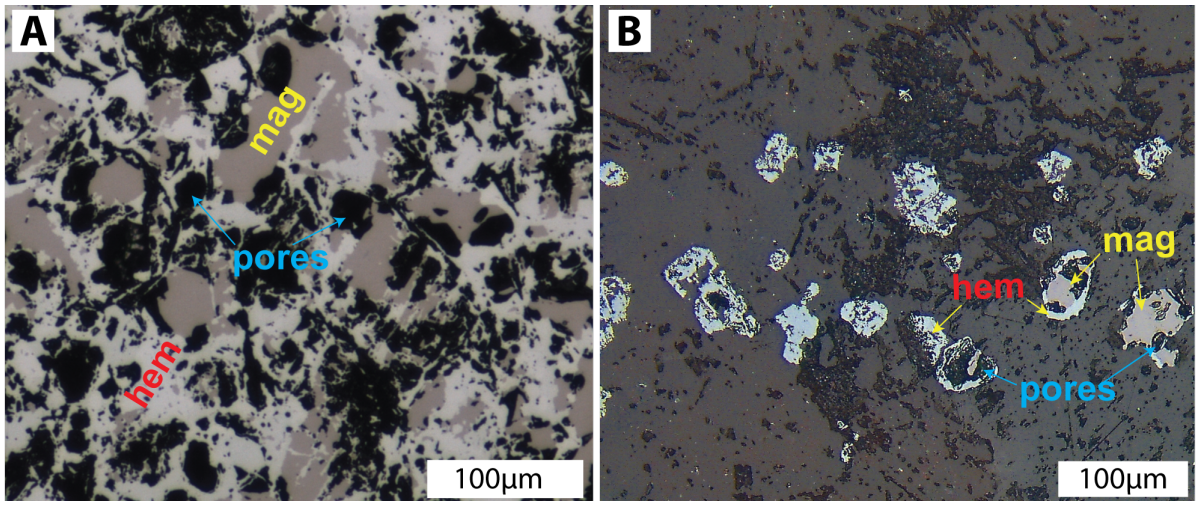

Fig. 5 | Ores from the Olympic Dam IOCG province. (A) Massive iron oxide ores from Torrens Dam (drill core TD 2), with hematite replacing magnetite. Hematite is porous with large pores. Pores are usually developed at the hematite-magnetite phase boundary and filled with quartz. (B) Hematitized rock from Emmie Bluff (drill core SAE 7). Hematite replacing magnetite along grain rims, with significant porosity developed at magnetite-hematite boundaries. Hematite is porous and usually display a hole (filled by quartz) around the core, with magnetite relicts in the core.

The replacement textures seen in our Ce-bearing experiments (Fig. 1a) are similar to those observed in ore textures from several deposits of the Olympic Dam Cu-Au province (e.g.,

Torrens Dam and Emmie bluff), with the same increased porosity in hematite, and the discontinuity usually existing at the hematite-magnetite boundary (Fig. 5; ref [10]). For these deposits, it is thought that oxidized fluids are responsible for the hematitization of the magnetite-rich assemblage (i.e., Reaction [1]) and formation of high-grade Cu-Au mineralization [11]. However, the redox state of the ore fluid, source of oxidant, and the reaction mechanisms for magnetite replacement are poorly constrained. Because magnetite replacement by hematite can happen through a redox or a non-redox pathway (Reactions [1] and [2]), it is misleading to simply use the mineral assemblages to infer the fluid redox. We have shown that the oxidation reaction of magnetite to form hematite (Reaction [1]) inhibits generation of high-grade hematite-associated ores in IOCG deposits, because the volume increase of the ore results in permeability loss, thereby limiting fluid-mineral interaction, fluid-mixing, and precipitation of new minerals (ore) [9]. Instead, Ce-catalyzed non-oxidative hematitization of magnetite significantly enhances the syn-mineralization porosity (Fig. 3), and thus makes formation of giant ore deposits more likely.

We suggest that similar trace element-induced catalyzation of mineral replacement may play a key role in ore genesis in other deposit types and hydrothermal ore-forming systems where such redox-sensitive trace element exists. For example, in the world's largest REE deposit, Bayan Obo, Ce-rich REE mineralization is accompanied by significant amounts of iron oxides (i.e., magnetite and hematite). The formation of Bayan Obo has been explained by multi-stage hydrothermal events, where cyclic fluid circulation drove dissolution-reprecipitation reactions and REE remobilization [23]. As at Olympic Dam and in the experiments, magnetite is typically replaced by porous hematite in the main stage ores [24], implying that the same Ce-catalyzation occurred. The fluids involved do not need to be oxidizing, and evolve from Ce-rich sources such as felsic magmas or carbonatites.

Unpredictable consequences – for now

This is the first time that a trace element has been demonstrated to act as a catalyst for an ICDR reaction (Fig. 3). Such effects are difficult to predict empirically, because they arise from a complex interplay between mineral solubility, nucleation, growth, and mass transfer at nano- to micro-scales. Although it is challenging to predict empirically which elements may play a similar role in porosity enhancement in a large range of hydrothermal systems, such effects are likely to affect a number of important geological reactions, including hydrous metamorphism,

metasomatism, and sodic/potassic alteration. However, their recognition requires a large experimental effort.

Acknowledgments

This study is supported by funding from the Australian Research Council (ARC) to Joël Brugger (DP140102765) and the McKinstry Fund from the Society of Economic Geologist (SEG) to Yanlu Xing (SRG_17-31). We thank Dr. Kan Li for his help with sample collection. We also acknowledge beamtime at the Australian Synchrotron, part of ANSTO (proposal AS181/XFM/12890). We are grateful to reviewers for suggestions that help to improve the manuscript.

References

1. Ehrig K, McPhie J, Kamenetsky V. Geology and mineralogical zonation of the Olympic Dam iron oxide Cu-U-Au-Ag deposit, South Australia. *Economic Geology* 2012, **Special Publication**(16)**:** 237-267.

2. Groves DI, Goldfarb RJ, Santosh M. The conjunction of factors that lead to formation of giant gold provinces and deposits in non-arc settings. *Geoscience Frontiers* 2016, **7**(3)**:** 303-314.

3. Oreskes N, Einaudi M. Origin of Rare Earth Element-Enriched Hematite Breccias at the Olympic Dam Cu-U-Au-Ag Deposit, Roxby Downs, South Australia. *Economic Geology* 1990, **85:** 1-28.

4. Hitzman M, Oreskes N, Einaudi M. Geological characteristics and tectonic setting of Proterozoic iron oxide (Cu-U-Au-REE) deposits. *Precambrian Research* 1992, **58:** 241-287.

5. Williams PJ, Barton M, Johnson D, Fontbote L, Haller A, Mark G*, et al.* Iron Oxide Copper-Gold Deposits: Geology, Space-Time Distribution , and Possible Modes of Origin. *Economic Geology* 2005, **100th Anniversary Volume:** 371-405.

6. Haynes D, Cross K, Bills R, Reed MH. Olympic Dam Ore Genesis: A Fluid-Mixing Model. *Economic Geology* 1995, **90:** 281-307.

7. Gow PA, Wall VJ, Oliver NHS, Valenta RK. Proterozoic iron oxide (Cu-U-Au-REE) deposits: Further evidence of hydrothermal origins. *Geology* 1994, **22**(7)**:** 633-636.

8. Bastrakov EN, Skirrow RG, Davidson GJ. Fluid Evolution and Origins of Iron Oxide Cu-Au Prospects in the Olympic Dam District, Gawler Craton, South Australia. *Economic Geology* 2007, **102:** 1415-1440.

9. Davidson GJ, Paterson H, Meffre S, Berry RF. Characteristics and Origin of the Oak Dam East Breccia-Hosted, Iron Oxide Cu-U-(Au) Deposit: Olympic Dam Region, Gawler Craton, South Australia. *Economic Geology* 2007, **102:** 1471-1498.

10. Gow PA. Geological evolution of the Stuart Shelf and Proterozoic iron oxide-associated mineralization: Insights from regional geophysical data. PhD thesis, Monash University, 1996.

11. Schlegel TU, Wagner T, Walle M, Heinrich CA. Hematite Breccia-Hosted Iron Oxide Copper-Gold Deposits Require Magmatic Fluid Components Exposed to Atmospheric Oxidation: Evidence from Prominent Hill, Gawler Craton, South Australia. *Economic Geology* 2018, **113**(3)**:** 597-644.

12. Bau M, Koschinsky A. Oxidative scavenging of cerium on hydrous Fe oxide: Evidence from the distribution of rare earth elements and yttrium between Fe oxides and Mn oxides in hydrogenetic ferromanganese crusts. *Geochemical Journal* 2009, **43**(1)**:** 37-47.

13. Zhao J, Brugger J, Pring A. Mechanism and kinetics of hydrothermal replacement of magnetite by hematite. *Geoscience Frontiers* 2019, **10**(1)**:** 29-41.

14. Otake T, Wesolowski DJ, Anovitz LM, Allard LF, Ohmoto H. Mechanisms of iron oxide transformations in hydrothermal systems. *Geochimica et Cosmochimica Acta* 2010, **74**(21)**:** 6141-6156.

15. Mücke A, Cabral AR. Redox and nonredox reactions of magnetite and hematite in rocks. *Chemie der Erde - Geochemistry* 2005, **65**(3)**:** 271-278.

16. Xia F, Brugger J, Chen G, Ngothai Y, O'Neill B, Putnis A*, et al.* Mechanism and kinetics of pseudomorphic mineral replacement reactions: A case study of the replacement of pentlandite by violarite. *Geochimica et Cosmochimica Acta* 2009, **73**(7)**:** 1945-1969.

17. Xing YL, Etschmann B, Liu WH, Mei Y, Shvarov Y, Testemale D*, et al.* The role of fluorine in hydrothermal mobilization and transportation of Fe, U and REE and the formation of IOCG deposits. *Chemical Geology* 2019, **504:** 158-176.

18. Putnis A. Why Mineral Interfaces Matter. *Science* 2014, **343**(6178)**:** 1441-1442.

19. Jonas L, John T, King HE, Geisler T, Putnis A. The role of grain boundaries and transient porosity in rocks as fluid pathways for reaction front propagation. *Earth and Planetary Science Letters* 2014, **386:** 64-74.

20. Altree-Williams A, Pring A, Ngothai Y, Brugger J. Textural and compositional complexities resulting from coupled dissolution–reprecipitation reactions in geomaterials. *Earth-Science Reviews* 2015, **150:** 628-651.

21. McPhie J, Kamenetsky V, Allen S, Ehrig K, Agangi A, Bath A. The fluorine link between a supergiant ore deposit and a silicic large igneous province. *Geology* 2011, **39**(11)**:** 1003-1006.

22. Xing Y, Mei Y, Etschmann B, Liu W, Brugger J. Uranium Transport in F-Cl-Bearing Fluids and Hydrothermal Upgrading of U-Cu Ores in IOCG Deposits. *Geofluids* 2018.

23. Smith MP, Campbell LS, Kynicky J. A review of the genesis of the world class Bayan Obo Fe-REE-Nb deposits, Inner Mongolia, China: Multistage processes and outstanding questions. *Ore Geology Reviews* 2015, **64:** 459-476.

24. Huang XW, Zhou MF, Qiu YZ, Qi L. In-situ LA-ICP-MS trace elemental analyses of magnetite: The Bayan Obo Fe-REE-Nb deposit, North China. *Ore Geology Reviews* 2015, **65:** 884-899.

Methods

Hydrothermal experiments

Natural magnetite from Itabira District, Minas Gerais, Brazil (SA Museum sample G32618) was used as the starting material. The material was crushed and grains ranging in size from 150-250 μm were selected for the experiment. The initial magnetite was analyzed using powder X-ray diffraction (XRD) and the results show >99% Fe_3O_4. The solution was prepared with an acetic acid - sodium acetate buffer, to get a calculated pH of 4 at 25 ºC. The salinity of the buffer was controlled by addition of 0.5M NaCl. For each run, the solution was doped with

200-300 ppm La(III), Ce(III) and Nd(III), respectively. Samples were reacted at 200 ºC for 8-14 days. Control experiments were conducted for two sets of solutions to quantify the effects from solution redox: (1) non-oxidative solutions by bubbling with N_2 gas, for which hematite and magnetite buffer the fO_2(g); (2) oxidative solutions by addition of 0.5 g 30% H_2O_2 solution. Details of our experiments are summarized in Table S1 in the supplementary material.

Textural and morphological characterization

Polarized optical microscopy was conducted using an Olympus BX51 microscope. Secondary Electron (SE) imaging and Electron Backscattered Diffraction (EBSD) were conducted with a FEI Quanta 3D Field Emission Scanning Electron Microscope (FESEM) at the Monash Centre of Electron Microscope (MCEM) at Monash University, Australia. Samples for SE imaging and EBSD were embedded into epoxy resin, polished and then coated with thin carbon film (~2-4 nm). The accelerating voltage for SE was maintained at 15 kV. EBSD patterns were collected at 15 kV, 11 nA with TSL OIM EBSD system. EBSD data was analyzed using TSL-OIM 8 software and Matlab MTEX toolbox. Crystallographic data for hematite and magnetite were taken from American Mineralogist Crystal Structure Database (AMCSD).

Powder X-ray Diffraction (XRD)

Powder X-ray diffraction patterns were collected on a Bruker D8 Advance Cobalt Machine (Co-Kα1 radiation, λ = 1.78892 Å) at the Monash X-ray Platform at Monash University, Australia, using 40 kV and 25 mA, and a 0.6 mm slit. Phase identification was conducted using Bruker EVA software. Phase fractions (i.e., hematite and magnetite) were determined via Rietveld refinement [25] using Bruker TOPAS package. Crystal structure data of magnetite and hematite were taken from ICDD PDF-4+ database.

Synchrotron XFM

Elemental distribution of Ce, La and Nd were mapped at the X-ray fluorescence spectroscopy (XFM) beam line [26] at the Australian Synchrotron, Melbourne, Australia. The incident beam energy was set at 18.5 keV using a Si(111) monochromator with an energy resolution of $\Delta E/E$ of ~2.8×10^{-4}. The beam was focused to a ~2x2 μm^2 spot size using Kirkpatrick-Baez mirrors. Fluorescence data were collected using the Maia model D384 detector array, which has an energy resolution of 240 eV and can detect elements down to atomic number 15 (phosphorous) [27, 28]. Samples were mapped using scanning speeds ranging from 2–5 mm/s, corresponding to dwell times of 0.3 to 1.75 ms/pixel. Standard foils (Pt, Mn, Fe) were used to constrain the detector geometry and efficiency; and to translate ion chamber counts to flux.

The data were analyzed with the GeoPIXE software package [29, 30], which utilizes the Dynamic Analysis method [31, 32, 33] to subtract background, unfold overlapping fluorescence peaks and then project elemental images from full fluorescence spectra (as opposed to just region-of-interest data).

The oxidation state of Ce was mapped using the XANES imaging technique, as described in Etschmann, Ryan [34,] Etschmann, Donner [35]. XANES stacks were measured by collecting SXRF maps at 109 irregularly spaced monochromator energies that spanned the Ce-L_3 edge, with 0.5 eV steps across the edge. A separate Dynamic Analysis matrix was used for each beam energy when processing the stack, in order to track the changing energy of the scatter peaks. The intensities of the Ce Lα peak at each pixel in the SXRF map, at each monochromators energy, were extracted and used to construct XANES spectra at each pixel and integrated over regions in the map selected based on Ce Lα intensity ratios at different energies or on sample composition.

References

25. Rietveld HM. A profile refinement method for nuclear and magnetic sturctures. *Journal of Applied Crystallography* 1969, **2:** 65-71.

26. Paterson D, de Jonge MD, Howard DL, Lewis W, McKinlay J, Starritt A*, et al.* The X-ray Fluorescence Microscopy Beamline at the Australian Synchrotron. 2011. pp. 219-222.

27. Kirkham R, Dunn PA, Kuczewski AJ, Siddons DP, Dodanwela R, Moorhead GF*, et al.* The Maia Spectroscopy Detector System: Engineering for Integrated Pulse Capture, Low-Latency Scanning and Real-Time Processing. 2010. pp. 240-243.

28. Ryan CG, Siddons DP, Kirkham R, Li ZY, de Jonge MD, Paterson DJ*, et al.* Maia X-ray fluorescence imaging: Capturing detail in complex natural samples. *Journal of Physics: Conference Series* 2014, **499**.

29. Ryan CG, Cousens DR, Sie SH, Griffin WL, Suter GF. Quantitative PIXE microanalysis of geological material using the CSIRO proton microprobe. *Nuclear Instruments and Methods in Physics Research* 1990, **B47:** 55-71.

30. Ryan CG, Kirkham R, Hough RM, Moorhead G, Siddons DP, de Jonge MD*, et al.* Elemental X-ray imaging using the Maia detector array: The benefits and challenges of large solid-angle. *Nuclear Instruments and Methods in Physics Research Section A: Accelerators, Spectrometers, Detectors and Associated Equipment* 2010, **619**(1-3)**:** 37-43.

31. Ryan CG, Jamieson DN. Dynamic analysis: on-line quantitative PIXE microanalysis and its use in overlap-resolved elemental mapping. *Nuclear Instruments and Methods in Physics Research B77* 1993**:** 203-214.

32. Ryan CG. Quantitative Trace Element Imaging Using PIXE and the Nuclear Microprobe. *International journal of imaging systems and technology* 2000, **11:** 219-230.

33. Ryan CG, Siddons DP, Kirkham R, Dunn PA, Kuczewski A, Moorhead G*, et al.* The New Maia Detector System: Methods For High Definition Trace Element Imaging Of Natural Material. 2010. pp. 9-17.

34. Etschmann BE, Ryan CG, Brugger J, Kirkham R, Hough RM, Moorhead G*, et al.* Reduced As components in highly oxidized environments: Evidence from full spectral XANES imaging using the Maia massively parallel detector. *American Mineralogist* 2010, **95**(5-6)**:** 884-887.

35. Etschmann BE, Donner E, Brugger J, Howard DL, de Jonge MD, Paterson D*, et al.* Speciation mapping of environmental samples using XANES imaging. *Environmental Chemistry* 2014, **11**(3)**:** 341-350.

Supplementary Materials

Appendix 4

Chapter 5

Arsenic evolution as a tool for understanding formation of pyritic gold ores

Yanlu Xing[1], Joël Brugger[1,*], Andrew Tomkins[1], Yuri Shvarov[2]

1. School of Earth, Atmosphere and Environment, Monash University, Clayton, VIC 3800, Australia

2. Lomonosov Moscow State University, Moscow, Russia

GEOLOGY | THE GEOLOGICAL SOCIETY OF AMERICA®

https://doi.org/10.1130/G45708.1

Manuscript received 15 October 2018
Revised manuscript received 27 January 2019
Manuscript accepted 29 January 2019

Published online 26 February 2019

Arsenic evolution as a tool for understanding formation of pyritic gold ores

Yanlu Xing[1], Joël Brugger[1]*, Andrew Tomkins[1], and Yuri Shvarov[2]
[1]School of Earth, Atmosphere and Environment, Monash University, Clayton, Victoria 3800, Australia
[2]Faculty of Geology, Lomonosov Moscow State University, 119991, Moscow, Russia

ABSTRACT

Arsenic (As) and gold (Au) are closely associated in many gold deposits, both being hosted in Fe-sulfide minerals (pyrite, marcasite, and arsenopyrite), partly because As geochemistry controls Au accumulation. Yet, the partitioning behavior of As between pyrite, arsenopyrite, and hydrothermal fluids remains poorly understood. Here, we introduce solid-solution models for As in pyrite and As in arsenopyrite into a thermochemical model of fluid-rock interaction, and use it to evaluate the effects of temperature, redox state, and fluid-flow dynamics on As—and Au by association—partitioning. We find that As concentrations in pyrite decrease with increasing temperature, despite the widening of the solid-solution composition range. This is related to the preferential partitioning of As into fluids at higher temperatures. Simulations of infiltration of rock-buffered H_2O-CO_2-As fluids into low-As pyrite (As:S = 0.01) ores reveal a continuous enrichment of As in pyrite with increasing fluid:rock ratio. The modeling suggests that upgrading of early-formed low-grade ores by multistage hydrothermal events can generate large gold deposits. In this scenario, an anomalously Au-rich fluid is not needed, but instead, prolonged fluid-rock interaction enriches pyrite in As, which promotes gold sequestration.

INTRODUCTION

The association between Au and As in Fe(-As) sulfides (pyrite [FeS_2], marcasite [FeS_2], and arsenopyrite [FeAsS]) is a well-recognized characteristic of most Au deposits. Hence, the correlation between Au and As makes As in pyrite a good proxy for Au mineralization. This As-Au coupling also may reflect a partial control of Au accumulation by As geochemistry in hydrothermal gold systems (Deditius et al., 2014). Yet, the behavior of As in fluid-rock systems remains poorly understood, due to limited understanding of the solid solution of As in iron-sulfide minerals (Reich and Becker, 2006).

Thermodynamic reactive transport modeling is an important tool for understanding complex fluid-rock interactions, element mass transfer, and the potential of fluids to carry economic amounts of metals (Seward and Barnes, 1997). To date, our capacity to model As mobility under hydrothermal conditions has been severely limited by the absence of a thermodynamic model for As-in-pyrite and As-in-arsenopyrite solid solutions. Consequently, most available models overestimate As mobility in hydrothermal fluids, because As remains in solution until an As-dominant mineral such as arsenopyrite or löllingite precipitates (Zhong et al., 2015).

Here, we build a model of As solid solution in pyrite-marcasite and in arsenopyrite, and use it to calculate the partitioning of As between pyrite-marcasite, arsenopyrite, and fluids under conditions typical for Au deposition (Phillips and Evans, 2004). We find that the model provides important insights into the role of fluid-rock interaction in Au mineralization. We show that the empirically well-established retrograde As solubility in pyrite with increasing temperature, T (Deditius et al., 2014), is a result of prograde As solubility in fluids. We further show that recurring fluid flow can enrich As in pyrite and arsenopyrite through extensive fluid-mineral interactions, which results in gold incorporation, generating high-grade gold resources.

THERMODYNAMIC MODELING OF THE FeS_2-$FeAs_2$ BINARY

The FeS_2-$FeAs_2$ binary (Fig. 1) is modelled using three phases: pyrite-marcasite solid solution [$Fe(S,As)_2$], arsenopyrite solid solution ($FeAs_{1-x}S_{1+x}$), and löllingite ($FeAs_2$). Löllingite is assumed to be stoichiometric, in view of the limited S solubility in this mineral (Fleet and Mumin, 1997; Reich and Becker, 2006).

Arsenopyrite is modeled as a solid solution between the fictional end members $FeS_{1.2}As_{0.8}$ and $FeS_{0.8}As_{1.2}$. Pyrite-marcasite is described as a solid solution between marcasite (FeS_2) and a fictional (fic) löllingite (Lö, $FeAs_2$), which is defined such that $\Delta_f G^{fic}_{Lo} = \Delta_f G_{Lo} + 10$ kJ/mol (where $\Delta_f G$ is the Gibbs free energy of formation from the elements to the subscripted species) so that löllingite is the stable mineral on the As-rich side of the diagram. This pyrite-marcasite model assumes that As^{1-} is substituting for sulfur in the disulfide anion, S_2^{2-}, which is the predominant substitution mechanism in pyrite-marcasite (Qian et al., 2013). Due to the nature of As-S interactions, non-ideal contributions need to be incorporated for realistic modeling of the FeS_2-$FeAs_2$ binary (Reich and Becker, 2006). Because of experimental difficulties (non-homogenous As distributions and nanoscale inclusions of As-rich phases), we use the theoretical energies of mixing derived from first principles by Reich and Becker (2006) to calibrate the excess free-energy models for pyrite-marcasite and arsenopyrite (Redlich-Kister formalism; Redlich and Kister, 1948). Reich and Becker (2006)'s calculations indicate that pyrite-marcasite can hold a maximum of ~6 wt% As in solid solution (Fig. 1); natural pyrite contains up to 19 wt% As, but many such As-rich pyrites have been shown to contain nanometer-size inclusions of As-rich phases (Deditius et al., 2014; Reich and Becker, 2006).

Thermodynamic calculations were conducted using the HCh software (http://www1.geol.msu.ru/deps/geochems/soft/index_e.html), which employs a Gibbs free-energy minimization algorithm (Shvarov, 1999, 2008). Figure 1 illustrates the good agreement between the HCh model and the theoretical phase

*E-mail: joel.brugger@monash.edu

CITATION: Xing, Y., Brugger, J., Tomkins, A., and Shvarov, Y., 2019, Arsenic evolution as a tool for understanding formation of pyritic gold ores: Geology, v. 47, p. 335–338, https://doi.org/10.1130/G45708.1

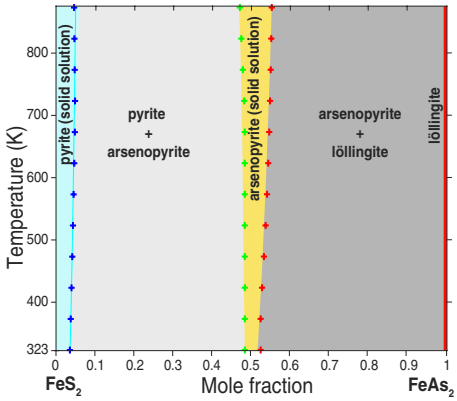

Figure 1. FeS_2-$FeAs_2$ phase diagram. Crosses represent theoretical diagram derived by Reich and Becker (2006) on basis of first-principle quantum mechanical computations, and colored fields are phase diagram predicted from thermodynamic data derived in this study.

diagram. Details of the calculation procedure and thermodynamic properties are provided in GSA Data Repository[1].

ARSENIC SOLUBILITY IN PYRITE-MARCASITE AND ARSENOPYRITE

Fluid-rock equilibria are calculated in the Fe-As-S-Na-Cl-K-Al-Si-H-O system (25–600 °C, fixed pressure of 200 MPa) for two conditions: an oxidized system buffered by pyrite + hematite, and a reduced system buffered by pyrite + pyrrhotite + magnetite. Fluid pH is buffered by K-feldspar + muscovite + quartz. Under these rock-buffered conditions, aqueous As concentrations increase with increasing temperature—from parts per billion to thousands of parts per million in the case of hematite-bearing assemblages (Fig. 2A). In arsenopyrite-absent assemblages, for a given As content of the simulated system, pyrite composition is largely temperature independent up to ~200 °C for the oxidized system, and 400 °C for the reduced system (Figs. 2C and 2D). Then As concentrations in pyrite decrease rapidly with increasing temperature, despite the fact that in the water-free system As solubility in pyrite increases slightly with temperature (Fig. 1).

The model predictions tally with the empirical observations that As contents of pyrite decrease as a function of increasing ore-formation temperature, from ~200 to ~500 °C (Deditius et al., 2014). To understand the cause of the retrograde As contents of hydrothermal pyrite, it is useful to express the equilibrium between pyrite and fluid in terms of the Nernst partition coefficient, $D_{py/f} = X_{As(py)} / X_{As(f)}$, where $X_{As(py)}$ and $X_{As(f)}$ are the mass fractions of As in pyrite and fluid, respectively. The hydrothermal fluids responsible for the world's major gold production (e.g., "orogenic gold"; Carlin-type gold; Witwatersrand goldfields) share common features: T >200 °C, CO_2-rich (0.05–0.25 mol%), S-bearing, and low salinity (Phillips and Evans, 2004; Mikucki 1998). In these fluids, As exists predominantly in the form of $[As^{3+}(OH)_3]_{(aq)}$ (James-Smith et al. 2010; Kokh et al. 2017), and As solubility controlled by pyrite is described by

$$As(OH)_{3(aq)} + ½FeS_{2(py)} + 2.5H_{2(g)} = ½FeAs_{2(py)} + HS^- + H^+ + 3H_2O\,, \quad (1)$$

where (aq) and (g) refer to aqueous and gaseous species, respectively.

Writing the equilibrium constant ($\log K_{P,T}$, at fixed pressure [P] and temperature [T]) and rearranging produces:

$$\log D_{py/f} = \log K_{P,T} + pH + 2.5\log f_{H_{2(g)}} - \log a_{HS^-} + \log \underbrace{\frac{\gamma_{FeAs_{2(py)}}}{\gamma_{As(OH)_{3(aq)}} \cdot \gamma_{FeS_{2(py)}}}}_{\text{Effect of composition of fluid and pyrite}}, \quad (2)$$

where γ is activity coefficient; a is activity; and f is fugacity. Equation 2 indicates a strong dependence of the partitioning upon local fluid conditions, including pH, redox [$f_{H_{2(g)}}$], and sulfur concentration, expressed as activity of the bisulfide ion, a_{HS^-}. The low As contents of pyrite at high temperature are due to low $\log D_{py/f}$ (Figs. 2C and 2D), which results mainly from the prograde S solubility (Fig. DR2 in the Data Repository) and prograde As solubility in fluids (encapsulated by $\log K_{P,T}$ in Equation 2). The strong redox dependence of As incorporation into pyrite is due to the fact that As^{3+} is the main oxidation state of As in aqueous fluids, whereas As^{1-} is predominant in pyrite: the As fraction is higher in pyrite that formed under reduced conditions compared to oxidized conditions (Figs. 2C and 2D). The calculated As partitioning coefficients between pyrite and solution for oxidized conditions (Fig. DR3) correspond well with the experimental and natural data reported by Kusebauch et al. (2018).

The As content of arsenopyrite (FeAsS) has been proposed as a geothermometer in gold systems, based on phase diagrams in the water-free Fe-As-S system (Kretschmar and Scott, 1976; Sharp et al., 1985). Figure 2 shows that in As-undersaturated systems (i.e., native As absent, corresponding to the vast majority of Au deposits), arsenopyrite coexisting with pyrite has decreasing As content with increasing temperature, although the composition change is small and not suitable for a geothermometer (Figs. 2C and 2D). In As-rich systems where arsenopyrite and löllingite coexist, the concentration of As in arsenopyrite increases with increasing temperature and can be used as a geothermometer. Where arsenopyrite and pyrrhotite coexist, the main control on arsenopyrite composition is the bulk system composition.

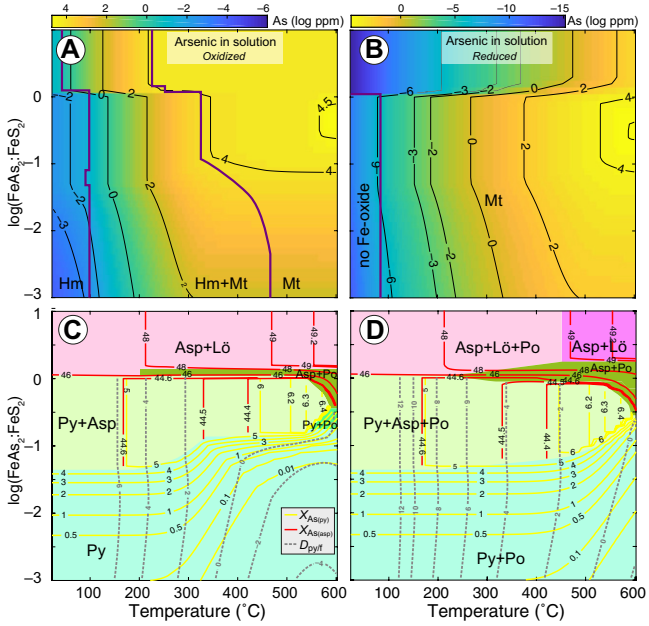

Figure 2. Results of modeling in HCh software (http://www1.geol.msu.ru/deps/geochems/soft/index_e.html) of As in pyrite and arsenopyrite in oxidized (left) and reduced (right) fluids as function of temperature (°C, x-axis) and As fraction in the rocks. Simulations apply to rock-buffered systems, where pH is buffered by K-feldspar + muscovite + quartz, fugacities $f_{O_2(g)}$ and $f_{S_2(g)}$ (g—gaseous species) are controlled by Fe-mineral assemblage, and As solubility is controlled by Fe-As sulfides. A,B: Solubility of As (in log parts per million) in fluids; thick solid lines represent phase boundaries for Fe-oxide minerals. C,D: Rock mineralogy (colored fields); yellow isolines represent As fraction in pyrite at equilibrium ($X_{As(py)}$, in weight percent), red isolines represent As mass fraction in arsenopyrite ($X_{As(asp)}$, in weight percent), and grey dotted isolines are calculated partitioning coefficient of As between pyrite and fluid ($D_{py/f}$). Asp—arsenopyrite; Hm—hematite; Lö—löllingite; Mt—magnetite; Po—pyrrhotite; Py—pyrite.

[1]GSA Data Repository item 2019114, description of the fundamental assumptions for the thermodynamic model of Fe-As-S minerals; details of the fitting procedure and Redlich-Kister formalism used, and the mixing parameters derived in this study; supporting information for the thermodynamic model of fluid-rock interaction, including sulfur concentrations and partitioning coefficients of arsenic between pyrite and solution for simulations in Figure 2; and starting compositions for the model in Figure 3, is available online at http://www.geosociety.org/datarepository/2019/, or on request from editing@geosociety.org.

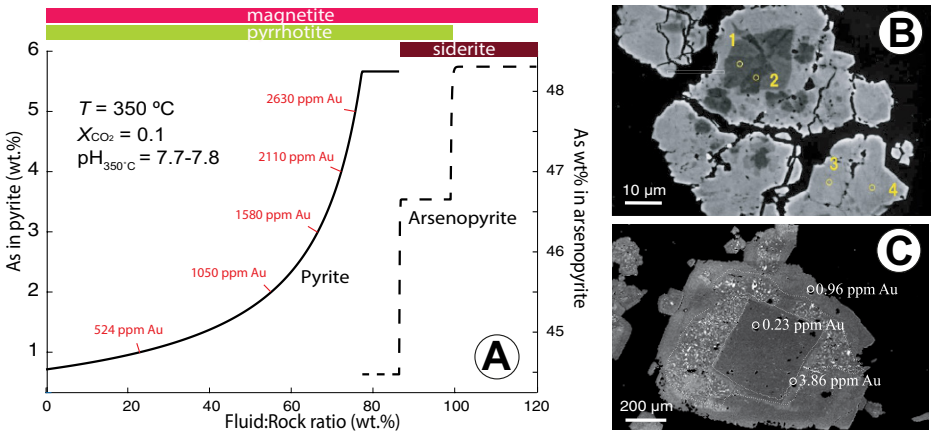

Figure 3. A: Upgrading of As in pyrite and arsenopyrite. Initial fluids have 100 ppm As and 10 mol% CO_2. Fluids were equilibrated with sulfur-bearing basalt before reacting with pyrite ores (initial pyrite As:S ratio of 0.01). Solid line represents As concentrations in pyrite, and dashed line, As concentrations in arsenopyrite. Maximum amount of Au for corresponding As concentrations in pyrite are plotted based on empirical solubility limit of Reich et al. (2005). B,C: Backscatter electron (BSE) images of complex growth and recrystallization textures in arsenian pyrite from Au deposits. In these images, lighter shades indicate higher As contents. B: As-rich rims and replacement of As-poor pyrite by As-rich pyrite (Hishikari ore deposit, Japan; image from Morishita et al., 2018; yellow circles and numbers are locations of analyses). C: Recrystallization of arsenian pyrite into porous zone of pyrite (white) with increased As-Au content (Sunrise Dam gold deposit, Western Australia; Au concentrations are shown for three points; image and analyses from Sung et al., 2009).

ARSENIC ENRICHMENT BY MULTI-STAGE HYDROTHERMAL FLUIDS

Several studies have highlighted the importance of multistage hydrothermal events and/or cyclic fluid flows to the formation and refinement of gold deposits (Sibson et al., 1975; Brugger et al., 2000; Bateman and Hagemann, 2004; Sung et al. 2009; Cockerton and Tomkins, 2012; Meffre et al., 2016). This repeated infiltration provides the extremely high fluid:rock ratios apparently required to form high-grade ore zones (Meffre et al., 2016; Mikucki, 1998; Thébaud et al., 2008). Indeed, the concentrations of As and Au in ore-forming fluids are usually relatively low (1–100 ppb Au, 0.10–100 ppm As; Mikucki, 1998; James-Smith et al., 2010; Goldfarb and Groves, 2015). This contrasts with the fact that As-rich zones in arsenian pyrite can contain up to ~2400 ppm Au and 20 wt% As (Reich et al., 2005), which is hard to reconcile with a single mineralization step for each zone.

A key aspect of any multistage As enrichment model is the efficiency of As scavenging from the fluid by reaction with the ores deposited in earlier stages. Hence, we model the infiltration of H_2O-CO_2-As fluids into pyritic rocks using the step-flow-reactor technique with HCh (Shvarov, 1999), in a manner similar to that of the model of Phillips and Evans (2004). The ore fluid is first equilibrated with basalt, which results in an As concentration of ~20 ppm in the fluid. Next, each batch of the fluid is reacted with As-poor pyritic rocks (As:S = 0.01, which is ~0.6 wt% As) at 350 °C, 200 MPa. Details of the modeling and fluid and rock composition are in the Data Repository.

The modeled pyrite and arsenopyrite compositions are plotted as a function of fluid:rock ratio in Figure 3A. Arsenic concentrations in pyrite gradually increase with increasing fluid:rock ratio and reach a maximum value of 5.7 wt% at a fluid:rock ratio of 80. Arsenopyrite forms when the fluid:rock ratio is >80, with As concentrations increasing steeply and reaching a maximum of 48.3 wt% at fluid:rock = 100.

DISCUSSION

The positive correlation between As and Au contents in arsenian pyrite has been well established in many gold systems, including Carlin-type (Cline, 2001; Reich et al., 2005), orogenic (Large et al., 2009; Morey et al., 2008), volcanogenic massive sulfide (Wagner et al., 2007), porphyry Cu-Au (Reich et al., 2013), and epithermal deposits (Deditius et al., 2014). Hence, As in pyrite is a good proxy for Au in many deposits. Equilibrium thermodynamic modelling of Au coprecipitation with Fe sulfides is not practical because the scavenging mechanisms remain controversial and mostly involve local conditions: for example, arsenic may enhance Au chemisorption on the surface of Fe sulfides, or local dissolution of Fe-As-S minerals may cause ultra-local reducing conditions, leading to precipitation of Au^{1+} aqueous complexes at the mineral surface (Pokrovski et al., 2014). Furthermore, Au concentrations in arsenian pyrite range across multiple orders of magnitude up to a solubility limit (Reich et al. 2005); this implies that most arsenian pyrites form from Au-undersaturated fluids. Indeed, in many gold deposits, native gold is a paragenetically late phase, resulting from recrystallisation of Fe-As sulfides (Fougerouse et al., 2016).

Complex As-Au zoning in pyrites characterized by both oscillatory zoning and secondary dissolution, reprecipitation, and recrystallisation textures is common in, and indeed characteristic of, Au deposits (Large et al., 2009). These variations are usually interpreted in terms of changing fluid sources or temperatures. For example, the As:Au ratio of As-Au–rich hydrothermal rims in pyrite is widely used to indicate fluid source, and further used to distinguish different stages of ore fluids (Thomas et al., 2011; Morishita et al., 2018). Pyrites from the Bendigo gold deposit (Australia) share similar As:Au ratios, suggesting that As-Au may be leached and transported together from the diagenetic and recrystallized metamorphic pyrite in the sediments (Thomas et al., 2011). However, thermodynamic constraints on the partitioning of As between hydrothermal fluid and pyrite indicates that the formation of these As-Au–rich rims via direct precipitation from the parent hydrothermal fluid requires fluids that are extremely enriched in As, which are unlikely to be found in nature. In particular, such fluid cannot be produced by leaching or by pyrite-to-pyrrhotite conversion of diagenetic and recrystallized metamorphic pyrite, which is significantly lower in As and Au (Thomas et al., 2011).

Mikucki (1998) estimated that high fluid:rock ratios (>100–1000) are required to form lode-gold deposits, assuming that Au is precipitated from fluids with Au concentration of 1–100 ppb at T <400 °C. Our modeling shows that fluids with relatively low As concentrations at T <300 °C are able to produce As-rich pyrite via protracted fluid flows. The upgrading model in Figure 3 indicates that As (and Au) enrichment in arsenian pyrite likely results from a refinement process; low-As fluids can effectively enrich As in pyrite through ongoing hydrothermal alteration. This mechanism may also explain the elevated As-Au content in pyrite associated with quartz veins at Bendigo, compared to diagenetic pyrite and metamorphic hydrothermal pyrite (Thomas et al., 2011), due to the higher local fluid:rock ratio required to form quartz veins and reefs. This progressive enrichment of As in pyrite is accompanied by a decrease in pyrite volume (Fig. DR4), which we suggest would serve to generate porosity in individual pyrite crystals and enhance Au sequestration (see Fig. 3).

In conclusion, our results show that the As concentration in pyrite is controlled by temperature, fluid composition, and redox, in addition to the As concentration in the parent fluid. Fluids with low As concentrations are able to form high-As arsenian pyrite and arsenopyrite through extensive hydrothermal alteration, thus forming the As(-Au) enrichment in ores. Externally derived As(-Au)–rich fluids are not necessarily required for forming high-grade pyritic gold ores. Instead, our thermodynamic model shows that dilute fluids can drive remobilization

and reprecipitation of As, forming As enrichment in localized high-grade domains, which would further facilitate Au accumulation. This is consistent with the evidence for high fluid:rock ratio and complex growth and/or dissolution and/or recrystallization textures of pyrite in gold ore zones. The solid-solution model for As in pyrite and arsenopyrite presented here makes it possible to precisely predict As solubility in pyrite and arsenopyrite under temperature- and redox-controlled conditions, which is an important tool for understanding and quantifying Au mobilization and enrichment in hydrothermal gold systems.

ACKNOWLEDGMENTS

Artur Deditius, Ross Large, Chris Clark, and an anonymous reviewer helped improve the manuscript, and their contribution is gratefully acknowledged. We thank the Australian Research Council (grant DP140102765 to Joël Brugger) and the Russian Foundation for Basic Research (grant 17-05-00244 to Yuri Shvarov) for supporting this research.

REFERENCES CITED

Bateman, R., and Hagemann, S., 2004, Gold mineralisation throughout about 45 Ma of Archaean orogenesis: Protracted flux of gold in the Golden Mile, Yilgarn craton, Western Australia: Mineralium Deposita, v. 39, p. 536–559, https://doi.org/10.1007/s00126-004-0431-2.

Brugger, J., Lahaye, Y., Costa, S., Lambert, D., and Bateman, R., 2000, Inhomogeneous distribution of REE in scheelite and dynamics of Archaean hydrothermal systems (Mt. Charlotte and Drysdale gold deposits, Western Australia): Contributions to Mineralogy and Petrology, v. 139, p. 251–264, https://doi.org/10.1007/s004100000135.

Cline, J.S., 2001, Timing of gold and arsenic sulfide mineral deposition at the Getchell Carlin-type gold deposit, north-central Nevada: Economic Geology and the Bulletin of the Society of Economic Geologists, v. 96, p. 75–89, https://doi.org/10.2113/gsecongeo.96.1.75.

Cockerton, A.B.D., and Tomkins, A.G., 2012, Insights into the liquid bismuth collector model through analysis of the Bi-Au Stormont skarn prospect, northwest Tasmania: Economic Geology and the Bulletin of the Society of Economic Geologists, v. 107, p. 667–682, https://doi.org/10.2113/econgeo.107.4.667.

Deditius, A.P., Reich, M., Kesler, S.E., Utsunomiya, S., Chryssoulis, S.L., Walshe, J., and Ewing, R.C., 2014, The coupled geochemistry of Au and As in pyrite from hydrothermal ore deposits: Geochimica et Cosmochimica Acta, v. 140, p. 644–670, https://doi.org/10.1016/j.gca.2014.05.045.

Fleet, M.E., and Mumin, A.H., 1997, Gold-bearing arsenian pyrite and marcasite and arsenopyrite from Carlin Trend gold deposits and laboratory synthesis: The American Mineralogist, v. 82, p. 182–193, https://doi.org/10.2138/am-1997-1-220.

Fougerouse, D., Micklethwaite, S., Tomkins, A.G., Mei, Y., Kilburn, M., Guagliardo, P., Fisher, L.A., Halfpenny, A., Gee, M., Paterson, D., and Howard, D.L., 2016, Gold remobilisation and formation of high grade ore shoots driven by dissolution-reprecipitation replacement and Ni substitution into auriferous arsenopyrite: Geochimica et Cosmochimica Acta, v. 178, p. 143–159, https://doi.org/10.1016/j.gca.2016.01.040.

Goldfarb, R.J., and Groves, D.I., 2015, Orogenic gold: Common or evolving fluid and metal sources through time: Lithos, v. 233, p. 2–26, https://doi.org/10.1016/j.lithos.2015.07.011.

James-Smith, J., Cauzid, J., Testemale, D., Liu, W.H., Hazemann, J.-L., Proux, O., Etschmann, B., Philippot, P., Banks, D., Williams, P., and Brugger, J., 2010, Arsenic speciation in fluid inclusions using micro-beam X-ray absorption spectroscopy: The American Mineralogist, v. 95, p. 921–932, https://doi.org/10.2138/am.2010.3411.

Kokh, M.A., Akinfiev, N.N., Pokrovski, G.S., Salvi, S., and Guillaume, D., 2017, The role of carbon dioxide in the transport and fractionation of metals by geological fluids: Geochimica et Cosmochimica Acta, v. 197, p. 433–466, https://doi.org/10.1016/j.gca.2016.11.007.

Kretschmar, U., and Scott, S.D., 1976, Phase relations involving arsenopyrite in the system Fe-As-S and their application: Canadian Mineralogist, v. 14, p. 364–386.

Kusebauch, C., Oelze, M., and Gleeson, S.A., 2018, Partitioning of arsenic between hydrothermal fluid and pyrite during experimental siderite replacement: Chemical Geology, v. 500, p. 136–147, https://doi.org/10.1016/j.chemgeo.2018.09.027.

Large, R.R., Danyushevsky, L., Hollit, C., Maslennikov, V., Meffre, S., Gilbert, S., Bull, S., Scott, R., Emsbo, P., Thomas, H., Singh, B., and Foster, J., 2009, Gold and trace element zonation in pyrite using a laser imaging technique: Implications for the timing of gold in orogenic and Carlin-style sediment-hosted deposits: Economic Geology and the Bulletin of the Society of Economic Geologists, v. 104, p. 635–668, https://doi.org/10.2113/gsecongeo.104.5.635.

Meffre, S., Large, R.R., Steadman, J.A., Gregory, D.D., Stepanov, A.S., Kamenetsky, V.S., Ehrig, K., and Scott, R.J., 2016, Multi-stage enrichment processes for large gold-bearing ore deposits: Ore Geology Reviews, v. 76, p. 268–279, https://doi.org/10.1016/j.oregeorev.2015.09.002.

Mikucki, E.J., 1998, Hydrothermal transport and depositional processes in Archean lode-gold systems: A review: Ore Geology Reviews, v. 13, p. 307–321, https://doi.org/10.1016/S0169-1368(97)00025-5.

Morey, A.A., Tomkins, A.G., Bierlein, F.P., Weinberg, R.F., and Davidson, G.J., 2008, Bimodal distribution of gold in pyrite and arsenopyrite: Examples from the Archean Boorara and Bardoc shear systems, Yilgarn craton, Western Australia: Economic Geology and the Bulletin of the Society of Economic Geologists, v. 103, p. 599–614, https://doi.org/10.2113/gsecongeo.103.3.599.

Morishita, Y., Shimada, N., and Shimada, K., 2018, Invisible gold in arsenian pyrite from the high-grade Hishikari gold deposit, Japan: Significance of variation and distribution of Au/As ratios in pyrite: Ore Geology Reviews, v. 95, p. 79–93, https://doi.org/10.1016/j.oregeorev.2018.02.029.

Phillips, G.N., and Evans, K.A., 2004, Role of CO_2 in the formation of gold deposits: Nature, v. 429, p. 860–863, https://doi.org/10.1038/nature02644.

Pokrovski, G.S., Akinfiev, N.N., Borisova, A.Y., Zotov, A.V., and Kouzmanov, K., 2014, Gold speciation and transport in geological fluids: Insights from experiments and physical-chemical modelling, *in* Garofalo, P.S., and Ridley, J.R., eds., Gold-Transporting Hydrothermal Fluids in the Earth's Crust: Geological Society of London Special Publication 402, p. 9–70, https://doi.org/10.1144/SP402.4.

Qian, G., Brugger, J., Testemale, D., Skinner, W., and Pring, A., 2013, Formation of As(II)-pyrite during experimental replacement of magnetite under hydrothermal conditions: Geochimica et Cosmochimica Acta, v. 100, p. 1–10, https://doi.org/10.1016/j.gca.2012.09.034.

Redlich, O., and Kister, A.T., 1948, Algebraic representation of thermodynamic properties and the classification of solutions: Industrial and Engineering Chemistry, v. 40, p. 345–348, https://doi.org/10.1021/ie50458a036.

Reich, M., Kesler, S.E., Utsunomiya, S., Palenik, C.S., Chryssoulis, S.L., and Ewing, R.C., 2005, Solubility of gold in arsenian pyrite: Geochimica et Cosmochimica Acta, v. 69, p. 2781–2796, https://doi.org/10.1016/j.gca.2005.01.011.

Reich, M., and Becker, U., 2006, First-principles calculations of the thermodynamic mixing properties of arsenic incorporation into pyrite and marcasite: Chemical Geology, v. 225, p. 278–290, https://doi.org/10.1016/j.chemgeo.2005.08.021.

Reich, M., Deditius, A., Chryssoulis, S., Li, J.W., Ma, C.Q., Parada, M.A., Barra, F., and Mittermayr, F., 2013, Pyrite as a record of hydrothermal fluid evolution in a porphyry copper system: A SIMS/EMPA trace element study: Geochimica et Cosmochimica Acta, v. 104, p. 42–62, https://doi.org/10.1016/j.gca.2012.11.006.

Seward, T.M., and Barnes, H.L., 1997, Metal transport by hydrothermal ore fluids, *in* Barnes, H.L., ed., Geochemistry of Hydrothermal Ore Deposits (third edition): New York, John Wiley & Sons, p. 435-486.

Sharp, Z.D., Essene, E.J., and Kelly, W.C., 1985, A re-examination of the arsenopyrite geothermometer: Pressure considerations and applications to natural assemblages: The Canadian Mineralogist, v. 23, p. 517–534.

Shvarov, Yu.V., 1999, Algorithmization of the numeric equilibrium modeling of dynamic geochemical processes: Geochemistry International, v. 37, p. 571–576.

Shvarov, Yu.V., 2008, HCh: New potentialities for the thermodynamic simulation of geochemical systems offered by windows: Geochemistry International, v. 46, p. 834–839, https://doi.org/10.1134/S0016702908080089.

Sibson, R.H., Moore, J.M., and Rankin, A.H., 1975, Seismic pumping—A hydrothermal fluid transport mechanism: Journal of the Geological Society, v. 131, p. 653–659, https://doi.org/10.1144/gsjgs.131.6.0653.

Sung, Y.-H., Brugger, J., Ciobanu, C.L., Pring, A., Skinner, W., and Nugus, M., 2009, Invisible gold in arsenian pyrite and arsenopyrite from a multistage Archaean gold deposit: Sunrise Dam, Eastern Goldfields Province, Western Australia: Mineralium Deposita, v. 44, p. 765–791, https://doi.org/10.1007/s00126-009-0244-4.

Thébaud, N., Philippot, P., Rey, P., Brugger, J., Van Kranendonk, M., and Grassineau, N., 2008, Protracted fluid-rock interaction in the Mesoarchaean and implication for gold mineralization: Example from the Warrawoona syncline (Pilbara, Western Australia): Earth and Planetary Science Letters, v. 272, p. 639–655, https://doi.org/10.1016/j.epsl.2008.05.030.

Thomas, H.V., Large, R.E., Bull, S.W., Maslennikov, V., Berry, R.F., Fraser, R., Froud, S., and Moye, R., 2011, Pyrite and pyrrhotite textures and composition in sediments, laminated quartz veins, and reefs at Bendigo Gold Mine, Australia: Insights for ore genesis: Economic Geology and the Bulletin of the Society of Economic Geologists, v. 106, p. 1–31, https://doi.org/10.2113/econgeo.106.1.1.

Wagner, T., Klemd, R., Wenzel, T., and Mattsson, B., 2007, Gold upgrading in metamorphosed massive sulfide ore deposits: Direct evidence from laser-ablation–inductively coupled plasma–mass spectrometry analysis of invisible gold: Geology, v. 35, p. 775–778, https://doi.org/10.1130/G23739A.1.

Zhong, R., Brugger, J., Tomkins, A.G., Chen, Y., and Li, W., 2015, Fate of gold and base metals during metamorphic devolatilization of a pelite: Geochimica et Cosmochimica Acta, v. 171, p. 338–352, https://doi.org/10.1016/j.gca.2015.09.013.

Printed in USA

Chapter 6

Conclusions

Yanlu Xing

School of Earth, Atmosphere and Environment, Monash University, Clayton, VIC, 3800

Fluid-rock interactions are key to controlling metal mobility from source to sink in hydrothermal ore systems. This thesis investigated several aspects that affect fluid-rock interaction, including metal hydrothermal mobilization, metal partitioning during fluid-mineral equilibria, and mechanisms of fluid-mediated mineral replacement reactions. Furthermore, we discussed the influence of these factors on the formation of large hydrothermal ore deposits. In this chapter, the results of the thesis are briefly summarized and based on this, an overview is given on how these new results contribute to understanding the formation of giant ore deposits.

6.1 Role of F in formation of IOCG deposits

Fluoride is widely thought to be able to form strong aqueous complexes with Fe, U and REE. However, its role in transporting metals is questioned since the recent discovery of low solubility of REE fluorides (Migdisov et al., 2016). IOCG deposits are one of the most notable hydrothermal systems that usually show elevated F concentrations in the ore and host rocks (Hitzman et al., 1992; McPhie et al., 2011).

In chapter 2, results from in-situ XAS experiments show that Fe(II/III)-F complexation is less important than previously thought and F tends to cause Fe precipitation at T>200ºC, in agreement with the predicted reversed solubility of FeF_2(s). Modelling of fluid-granite equilibria shows that fluoride complexing is insignificant for Fe and U transport, whereas it plays an important role on REE transport. Calculations show that fluid-granite interaction is able to form fluids with up to ~70 ppm F at 450 ºC. This F concentration is relatively low compared to some magmatic fluids, in which case extensive hydrothermal activities are required to form the large F endowment observed in some IOCG deposits (e.g., Olympic Dam). Including F in the model can help to increase solubility of silicates, as it not only affects Si-F complexing, but also bulk fluid pH which results in increased concentrations of $H_3SiO_4^-$ and $NaHSiO_3$(aq). Overall, although the transporting role of F is less important than previously thought, presence of F is able to affect pH, redox and the mineralogy. These will therefore increase the metal carrying ability of the fluids and also the permeability of the breccia and wall rock, which are essential for the formation of giant ore deposits.

6.2 Uranium transport and formation of U-F association

The association between U and F is common in hydrothermal uranium deposits including IOCG deposits, orogenic U deposits, and volcanogenic and vein-type deposits hosted in felsic rocks (Cuney and Kyser, 2009; Hu et al., 2008; McGloin et al., 2016). This co-enrichment of U and F has long been attributed to the transporting role of F for U(IV/VI) in fluids. In Chapter

3, we thoroughly reviewed the available thermodynamic properties for U(IV/VI)-F complexes, and compared the stability of U(IV/VI) fluoride complexes with chloride and hydroxide complexes under hydrothermal conditions. We show that fluoride is overestimated for U hydrothermal transport, especially at elevated temperatures (T>250 ºC). Formation of the U-F co-enrichment in the Olympic Dam ores reflect that U and F may come from a same source (e.g., Roxby Down granite) and are enriched via the same hydrothermal processes, rather than reflecting an essential role of F in U transportation or controlling the metal endowment of these deposits.

6.3 The catalysing role of Ce on magnetite to hematite transformation reaction

In IOCG deposits, the replacement of magnetite by hematite is widely observed and is thought to be important during the second stage hematite-alteration, which is closely associated with high-grade ore genesis. Chapter 4 investigates the product textures for magnetite to hematite transformation under both oxidative and non-oxidative conditions in the presence of La, Ce and Nd. The results show that the reaction is actually much less efficient in oxidative fluids compared to non-oxidative fluids. Moreover, it is the first time showing that trace amount of Ce(III) can catalyse magnetite to hematite transformation by enhancing the syn-mineralization porosity. In fact, Ce(III) may actually be the key factor for generating the observed ore textures (e.g., Emmie Bluff, Torrents Dam), which can facilitate fluid penetration in hematite ores and thus greatly boost the fluid-rock interaction. Therefore, it shows that trace amounts of Ce may play a key role in the formation of a giant ore deposit such as Olympic Dam.

6.4 Arsenic behaviour in hydrothermal gold systems

In Chapter 5, we present the first thermodynamic model for solid solutions of arsenian pyrite and arsenopyrite. This model makes it possible to accurately evaluate the partitioning behaviour of As during the formation of pyritic gold ores, and to use As concentration in pyrite and arsenopyrite as a geothermometer. Furthermore, reactive transport modelling show that the high As concentration in pyrite can be achieved via circulation of fluids with low As content, which requires high fluid:rock ratio. This result is consistent with field observations that high-grade gold ores usually have pyrite with complex growth and/or dissolution/reprecipitation textures, indicating complex growth/alteration history. Therefore, because of the coupled geochemistry of As and Au, the new solid solution model presented here makes As a good tool to look at the ore forming history in hydrothermal gold systems.

6.5 Concluding remarks

The formation of large and those giant ore deposits is usually a combination of many geological processes (Richards, 2013). Understanding specific factors that have a major contribution to the formation of those giant ore deposits help us build accurate genesis models, which are important for guiding exploration targeting. Regardless of types of deposits, some factors have common effects that are crucial for the formation of the deposits. For example, the transporting role of F for metals such as Fe, U and REE under the P-T-x range studied here is not only applicable to IOCGs, but also any other systems where such combination exists under similar conditions.

It is also should be noted that the explanation of some phenomena recognized in hydrothermal systems may result from different fluid-rock interactions, which requires caution and good understanding of the reaction mechanisms and the ore textures that observed in nature. As we show in this thesis that permeability is an essential factor that controls the formation of most hydrothermal ore forming systems. Mineral-scale porosity change has significant influence of the overall permeability of the whole system but explanation of the porosity change in different minerals or rocks could be very different. This can be seen from the F induced porosity change in silicate minerals/rocks compared to magnetite to hematite transformation induced porosity change. In the case F, it helps dissolve silicate minerals but it has no significant influence on the porosity of iron-oxide ores (i.e., magnetite and hematite), for which some other trace element may actually be the key, such as Ce, to affecting the reaction and generating porosity. Therefore, when considering the effects of certain fluid-rock interactions on ore formation, or influence from some specific elements, the overall geological background is important to consider (such as composition and property of wall-rock) when building up the genesis model for ore deposits.

Fluid-rock interaction is one of the essential processes that happens throughout the ore forming history. Understanding the formation of hydrothermal ore deposits, especially those economically large and giant deposits, requires good knowledge on mechanisms and influence of fluid-rock interaction. In summary, this thesis investigates fluid-rock interaction and its influence on ore formation through three perspectives: (1) metal mobilization in fluids containing specific ligands (i.e., F and Cl); (2) mineral replacement reaction mechanisms; (3) remobilization and enrichment mechanisms of metals through multi-stage hydrothermal activities and cyclic fluid flows. However, there are still several aspects that require further investigation:

(1) The transporting role of F for U requires further experimental study on U-F complexation at hydrothermal conditions (e.g., T>200ºC). This is because the current thermodynamic properties of several U(IV/VI)-F species are extrapolated based on room temperature or low temperature experimental data. In this case, there are uncertainties for these properties when using them to do calculations and modelling at higher temperatures.

(2) The coupled geochemistry enables As to be a good proxy for Au. However, it is still not clear about why As can help Au absorption in pyrite and the mechanisms for As and Au sequestration. Understanding of these requires more experimental studies.

(3) The catalysing role of Ce on magnetite to hematite transformation reactions for the first time shows that trace elements can play an essential role in changing reaction mechanism for mineral replacement and defining the ore textures, which further affects the hydrothermal circulation in the ore forming systems and contributes to the formation of a giant ore deposit. This provides a thoroughly new perspective to investigate the mechanisms of mineral replacement reactions in the presence of specific trace elements, apart from the common 'important' factors such as temperature, salinity, pH, fO_2, etc.

Investigation of these problems requires more experimental and theoretical efforts but their understanding will contribute to more accurate genesis models of hydrothermal ore formation, which are still at the centre of the study of mineral ore deposits and essential for future exploration.

6.6 References

Cuney, M., and Kyser, K., 2009, Hydrothermal Uranium Deposits Related to Igneous Rocks, Recent and not-so-recent developments in uranium deposits and implications for exploration, Published jointly by the Mineralogical Association of Canada (MAC) and the Society for Geology Applied to Mineral Deposits (SGA).

Hitzman, M., Oreskes, N., and Einaudi, M., 1992, Geological characteristics and tectonic setting of Proterozoic iron oxide (Cu-U-Au-REE) deposits: Precambrian Research, v. 58, p. 241-287.

Hu, R. Z., Bi, X. W., Zhou, M. F., Peng, J. T., Su, W. C., Liu, S., and Qi, H. W., 2008, Uranium metallogenesis in South China and its relationship to crustal extension during the Cretaceous to Tertiary: Economic Geology, v. 103, no. 3, p. 583-598.

McGloin, M. V., Tomkins, A. G., Webb, G. P., Spiers, K., MacRae, C. M., Paterson, D., and Ryan, C. G., 2016, Release of uranium from highly radiogenic zircon through metamictization: The source of orogenic uranium ores: Geology, v. 44, no. 1, p. 15-18.

McPhie, J., Kamenetsky, V., Allen, S., Ehrig, K., Agangi, A., and Bath, A., 2011, The fluorine link between a supergiant ore deposit and a silicic large igneous province: Geology, v. 39, no. 11, p. 1003-1006.

Migdisov, A., Williams-Jones, A. E., Brugger, J., and Caporuscio, F. A., 2016, Hydrothermal transport, deposition, and fractionation of the REE: Experimental data and thermodynamic calculations: Chemical Geology, v. 439, p. 13-42.

Richards, J. P., 2013, Giant ore deposits formed by optimal alignments and combinations of geological processes: Nature Geoscience, v. 6, no. 11, p. 911-916.

Appendices

Chapter 2

Supplementary materials include: Appendix 1. Details on thermodynamic modelling;

Appendix 2. XANES spectra.

These can be found on online at

***https://doi.org/10.1016/j.chemgeo.2018.11.008*.**

Refer to

Xing, Y. L., Etschmann, B., Liu, W. H., Mei, Y., Shvarov, Y., Testemale, D., Tomkins, A., and Brugger, J., 2019, The role of fluorine in hydrothermal mobilization and transportation of Fe, U and REE and the formation of IOCG deposits: Chemical Geology, v. 504, p. 158-176.

Chapter 3

Appendix 3. This can be found online at

https://doi.org/10.1155/2018/6835346

Refer to

Xing, Y., Mei, Y., Etschmann, B., Liu, W., and Brugger, J., 2018, Uranium Transport in F-Cl-Bearing Fluids and Hydrothermal Upgrading of U-Cu Ores in IOCG Deposits: Geofluids.

Chapter 4

Appendix 4.

Appendix 4

Trace cerium catalyzes formation of giant ore deposits

Yanlu Xing[1], Joël Brugger[1*], Barbara Etschmann[1], Andy Tomkins, and Xiya Fang[2],

1. School of Earth, Atmosphere and Environment, Monash University, Clayton, Melbourne, Victoria, Australia
2. Monash Centre for Electron Microscopy, Monash University, Clayton, Melbourne, Victoria, Australia

Corresponding author: yanluxxing@gmail.com; joel.brugger@monash.edu

Table S1 Summary of reaction conditions in batch Teflon reactors

Run	T (°C)	pH	S/F (g/L)	Oxidant	NaCl/ M	Filling gas	Time /days	REE (ppm)	REE	Products
MH38	200	4	Acetate acid buffer		0.5	N_2	8	250.6	La	hem 23.4, mag 76.6
MH39	200	4	Acetate acid buffer		0.5	N_2	8	203.1	Ce	hem 54.1, mag 45.9
MH40	200	4	Acetate acid buffer		0.5	N_2	8	168.5	Nd	hem 22.7, mag 77.3
MH41	200	4	Acetate acid buffer	0.2g H_2O_2	0.5	N_2	8	202.0	La	hem 15.8, mag 84.2
MH42	200	4	Acetate acid buffer	0.2g H_2O_2	0.5	N_2	8	237.0	Ce	hem 11.5, mag 88.5
MH43	200	4	Acetate acid buffer	0.2g H_2O_2	0.5	N_2	8	180.0	Nd	hem 12.1, mag 87.9
MH44	200	4	Acetate acid buffer		0.5	N_2	14	255.8	Ce	hem 60.5, mag 39.6
MH45	200	4	Acetate acid buffer		0.5	N_2	14	321.7	La	hem 22.8, mag 77.3
MH46	200	4	Acetate acid buffer	0.2g H_2O_2	0.5	Air	14	267.1	Ce	hem 12.7, mag 87.3

Textures for samples reacted in oxidative solutions

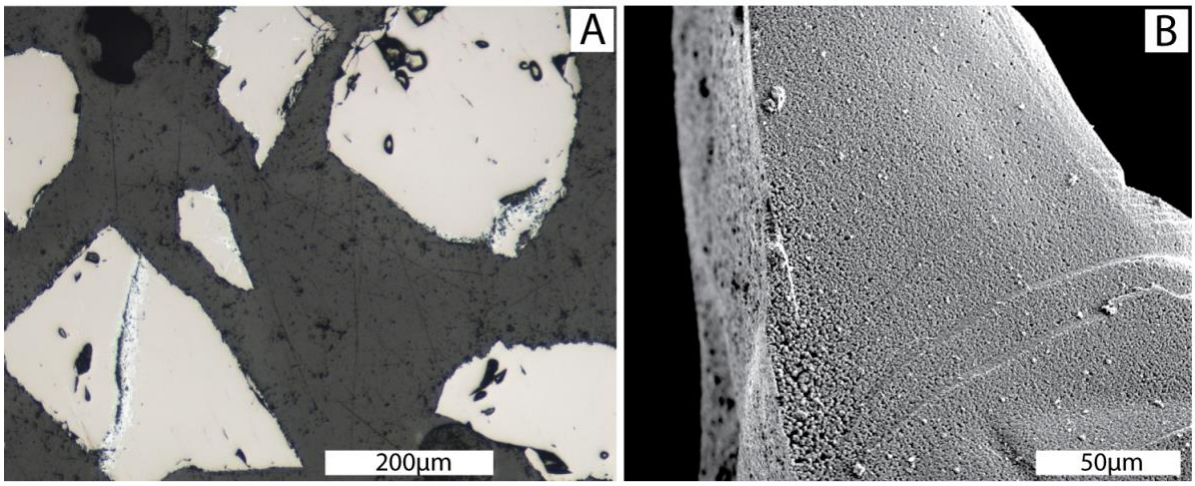

Figure S1. Optical microscopy and SE image of samples reacted in oxidative solution. (A) Little replacement of magnetite replacement along the rim or cracks. (B) Surface of the grain is smooth, with little porosity developed.

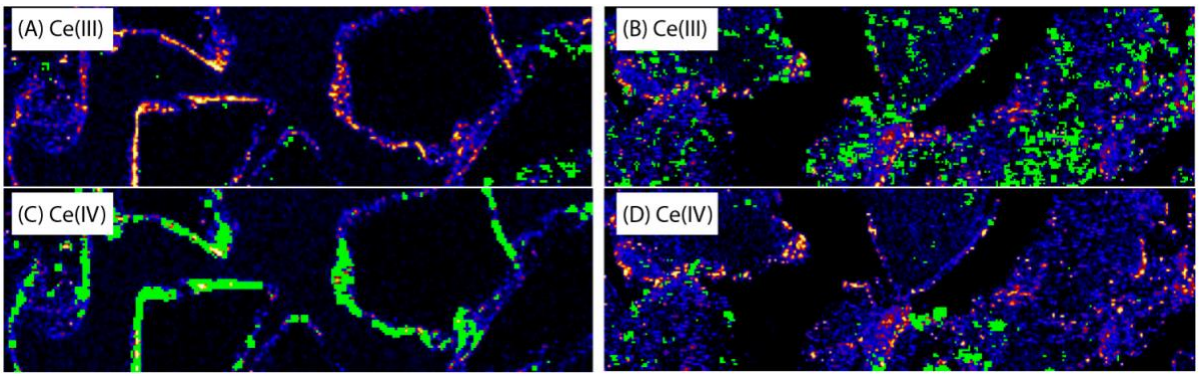

Figure S2. XFM mapping for Ce(III) and Ce(IV) of samples from oxidative (A, C) and non-oxidative(B, D) solutions. (A) Ce(III) and (C) Ce(IV) distribution for sample run under oxidative condition. (B) Ce(III) and (D) Ce(IV) distribution for sample run under non-oxidative condition.

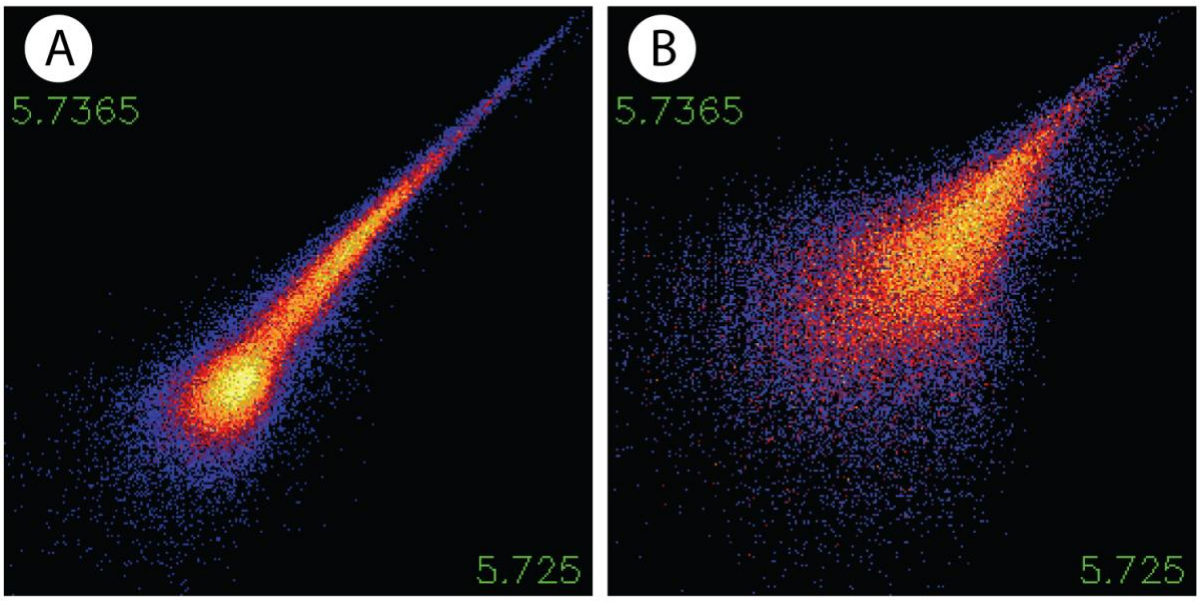

Figure S3. XANES energy distribution of Ce for samples from oxidative and non-oxidative solutions. (A) Sample reacted in oxidative solution. The mapping shows a slim, single tail with less low energy points, indicating that the energy for Ce is concentrated and Ce^{4+} is the predominant species. (B) Sample reacted in non-oxidative solution. Mapping shows two tails and more low energy points, indicating that Ce distribution is more separated, compared to samples reacted in oxidative solutions; Ce^{3+} and Ce^{4+} are both important while Ce^{3+} is the predominant.

Chapter 5

Appendix 5. This can be found online at

http://www.geosociety.org/datarepository/2019

Refer to

Xing, Y., Brugger, J., Tomkins, A., and Shvarov, Y., 2019, Arsenic evolution as a tool for understanding formation of pyritic gold ores: Geology, v. 47, no. 4, p. 335-338.